Title

Nanophotonic designs for light-driven propulsion and space exploration

Permalink

https://escholarship.org/uc/item/1d88x3gf

Author

Tung, Ho-Ting

Publication Date

2023

Peer reviewed|Thesis/dissertation

UNIVERSITY OF CALIFORNIA

Los Angeles

Nanophotonic designs for light-driven propulsion and space exploration

A dissertation submitted in partial satisfaction of the

requirements for the degree Doctor of Philosophy

in Aerospace Engineering

by

Ho-Ting Tung

2023

ABSTRACT OF THE DISSERTATION

Nanophotonic designs for light-driven propulsion and space exploration

by

Ho-Ting Tung

Doctor of Philosophy in Aerospace Engineering

University of California, Los Angeles, 2023

Professor Artur R. Davoyan, Chair

Space exploration is of paramount importance to advancing fundamental science, such as understanding the formation of universe and origins of life, as well as for the global economy, including communications and navigation. Despite the many milestones that we've witnessed in the last 60 years of space exploration, today's space exploration is hindered by the limitations of existing spacecraft propulsion technologies. Specifically, limited acceleration and velocity gain constrain the range of possible orbital maneuvers and challenge visionary deep space missions.

In this thesis, we examine the use of radiation pressure for fast in-space propulsion. We show that minute forces of radiation pressure may be utilized to accelerating spacecraft to speeds that surpass those attainable by conventional chemical rockets and electric engines. Agile and fast-transit Earth orbital maneuvering and fast-flyby solar system exploration missions are discussed. Two distinct approaches to light-driven space exploration are examined. Lightsailing that makes use of laser beams is shown to be advantageous for Earth orbital transfers and for missions to outer planets with small <10 g payloads. Solar

sails provide an alternative for outer planet and interstellar space exploration. By sending ultralight solar sails close to the sun, solar-sail spacecraft can be accelerated to very high velocities. Both approaches face a number of technical and materials challenges, some of which are studied in this thesis.

One of the key objectives of this dissertation is to design and fabricate suitable materials for such high speed light-driven propulsion approaches. We use a combination of analytical, computational, and experimental methods. Starting with space mission concept of operations analysis and examining related parameter tradeoffs, we provide guidelines that drive computational and experimental research of this thesis. Both analytical and computational methods are used to photonic materials that meet stringent mission requirements. A novel fabrication process is developed to prototype sail materials designed theoretically. Fabricated samples are measured and characterized, and their performance is examined. Lastly, possible space environmental effects associated with solar sailing in the close proximity to the sun are discussed and analyzed. This work aims at laying a foundation for the design of materials based on nanophotonic engineering for future light-driven in-space propulsion.

The dissertation of Ho-Ting Tung is approved.

Timothy S. Fisher

Richard E. Wirz

Raymond M. Spearrin

Artur R. Davoyan, Committee Chair

University of California, Los Angeles

2023

TABLE OF CONTENTS

LIST OF FIGURES

Figure 2.4 Concept of laser propelled wafer scale femtosatellites. (Left) Schematic illustration of some of the applications of such femtosatellites: 1) seamless sensor networks for Earth and space observations and situational awareness, 2) fast orbital transfer for inspection and fuel delivery, 3) inspection of large and costly space assets. Beamed laser propulsion is key to enabling agile high Δv maneuvering and fast on-demand orbital transfers. (Right) Schematic illustration of a wafer satellite. The top side carries all of the

LIST OF TABLES

ACKNOWLEDGEMENTS

I would start with thanking my PhD advisor, Professor Artur Davoyan for his guidance, support, encouragement, expertise and mentorship. He is the sole reason that I am able to be here in the US and UCLA to experience studying aboard as a PhD student. Thanks to you I have been able to learn not only research and coursework, but also academic writing, assisting with undergraduate course teaching, and being a better presenter. I am grateful to be one of your first students in UCLA. We have grown together in this journey.

I would also like to thank my doctoral committee. Professor Timothy Fisher is the one of the first professors that I took classes from at UCLA. The project that I did in the class helped setting a good framework for my research later on. Professor Richard Wirz introduced me to plasma physics, and the discussion that we had on plasma physics eventually leads to a part of this dissertation about plasma interaction with materials. Professor Mitchell Spearrin have graciously kept up with my work throughout the years at UCLA, and has provided me with invaluable insights along the way.

Next I would like to thank my family and friends, whether in US or Taiwan, for standing by me during the most challenging moments. Pursuing a PhD is a significant undertaking, and I would be nowhere near where I am now without them. Their continuing support, both physical and emotional, has been invaluable throughout this journey. Every ounce of effort they invested is truly priceless. Special appreciation goes to Celestine, Joy, and Esther—your late-night and early-morning calls were always a source of comfort. No matter what time zones we are in we will always be best friends for life. To Jeremy, Josh, and Michael, thank you for being my pillars of support in California. And despite the

physical distance, Audi has consistently been there whenever I needed someone to talk to. I extend my heartfelt thanks to Rick, Andy, and Yen-Wen for providing a home away from home for Taiwanese international students. Additionally, I am grateful to Christine, Pacie, and Eddie for their guidance and assistance on various aspects of life in the United States.

Many thanks goes to my fellow lab cohorts Hanon Ling, Pavel Shafirin, Hanseong Jo, Tom Joly-Jehenne, and Evy Haynes. Especially Haonan, who for a while has been the only labmate, including during challenging times of COVID. We have consistently supported each other, and tanked almost everything together. Special thanks to Evy helping me on fabricating a lot of the CNT films used in this dissertation. The cleanroom staff are also crucial part to this dissertation. Yuwei Fan, Hoc Ngo, Lorna Tokunaga, Angelica Saenz-Trevizo, Joe Zendejas, Brian Matthews, and Noah Bodzin all aided me in different parts of this study. There are many other people that I need to thank and the list can go on. The PhD is truly a team effort, if anything.

VITA

2016	B.S. in Electrical Engineering, National Tsing Hua University
2018	M.S. in Photonic Technologies, National Tsing Hua University
2019-2023	Graduate Research Assistant, University of California, Los Angeles

Publications

Ho-Ting Tung, and Artur R. Davoyan. "Carbon nanotube assisted ultrathin films for next generation solar sailing," *in preparation* (2023).

Jagrit Digani, Ho-Ting Tung, Artur R. Davoyan, "Inverse design of all-dielectric solar sails," *in preparation* (2023).

Haonan Ling, Arnab Manna, Jialiang Shen, Ho-Ting Tung, David Sharp, Johannes Fröch, Siyuan Dai, Arka Majumdar, and Artur R. Davoyan, "Deeply Subwavelength Integrated Excitonic van der Waals Nanophotonics" *Optica* **10**, 1345-1352 (2023).

Ho-Ting Tung, and Artur R. Davoyan. "Low-power laser sailing for fast-transit space flight." *Nano Letters* **22**, 1108-1114 (2022).

Ho-Ting Tung, Yu-Kai Chen, Pei-Lun Jheng, and Yu-Chueh Hung, "Origin and manipulation of band gaps in three-dimensional dielectric helix structures." *Optics Express* **25**, 17627-17638 (2017).

CHAPTER 1

Introduction

1.1 Space exploration today
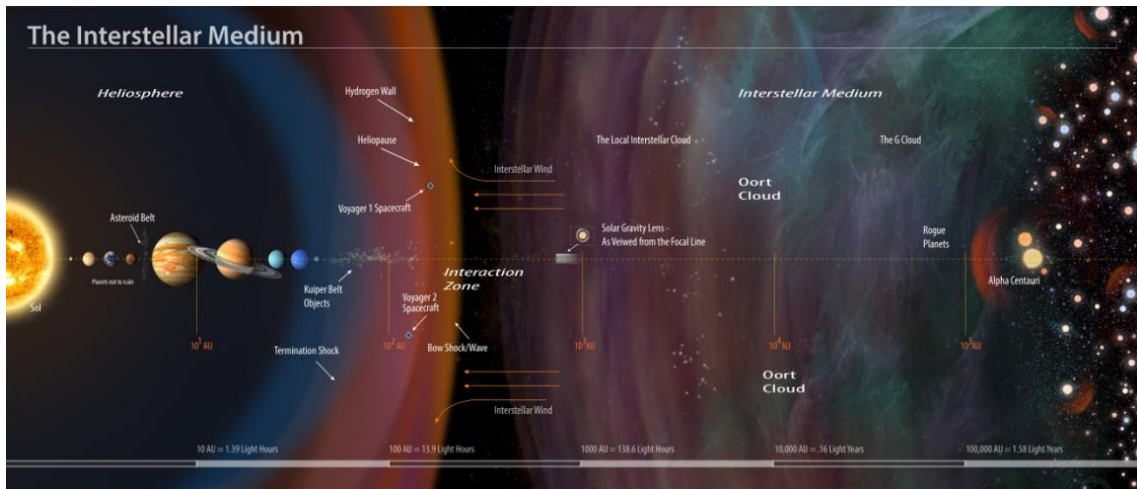
Figure 1.1 Artistic illustration of the solar system and interstellar space on a logarithmic scale. Advanced propulsion is key to enabling scalable exploration of outer solar system, Kuiper belt objects and interstellar medium. (Image by Pat Brennan, NASA's Exoplanet Exploration Program)

Since the launch of the first artificial satellite into Earth's orbit in 1957, space exploration has proven invaluable for uncovering new scientific discoveries. Of a particular interest are interplanetary and deep space missions, offering insights into the formation of the solar system, the evolution of the universe, and, potentially, the origins of life [1-3]. At the same time, vast distances of space challenge space exploration. Hence, in the past sixty years only five space probes have been sent beyond the orbit of Jupiter: Pioneer 11, Voyager 1 and 2, Cassini–Huygens, and New Horizons. Missions to outer planets take

years of flight time and decades of costly spacecraft development. For example, it took Juno – recent NASA's mission to Jupiter – >5 years of flight to reach the destination [1]. The long flight time translates onto development and mission support costs, which further constrains outer space exploration.

Nevertheless, exploration of outer solar system remains of high priority. For example, recently, the planetary science community in its recent Decadal Survey selected Uranus as the target of highest priority for NASA's next large-scale "flagship" mission [2]. Study of Uranus is important to better understanding of its composition and origin. Furthermore, planets like Uranus are among the most common types that have been discovered in recent exoplanet surveys. Collecting data from Uranus system would help inferring on composition and dynamics of many of recently discovered exoplanets. However, to date Uranus and Neptune have been visited only once more than 30 years ago; both by NASA's Voyager 2 probe in 1986 and 1989, respectively. One of the major obstacles is a long transit time (~15 years) and the need for performing energetic maneuvers. More efficient means of propulsion and space exploration could expedite discoveries and study of outer planets.

Beyond Uranus and Neptune lie vast reaches of interstellar space. Our sun is thought to be located near the edge of a local interstellar cloud [3]. The solar wind streams outward from sun's corona and expands throughout and beyond the solar system. The solar wind and the interstellar medium interact to create a complex structure – a global heliosphere. Global heliosphere extends to around 200-300 astronomical units (AU) in the upstream direction (towards the local interstellar flow) and thousands of AU tailward, where it shields the solar system from the plasma, energetic particles, small dust, and fields

of the interstellar medium. To directly probe the interstellar medium, it is necessary to go to at least 200 AU and well beyond the heliopause.

Exoplanet imaging requires going even further out. Ever since the first exoplanet was discovered in 1992, there is a strong desire to image and collect spectroscopic information of exo-worlds. Direct multipixel imaging is beyond the reach of current observatories. For this purpose, use of solar gravitational lens for high resolution imaging and spectroscopy was proposed. The lens could reconstruct the exoplanet image with ~25 km-scale surface resolution in ~6 months of integration time, enough to see surface features and signs of habitability [4]. However, such solar gravity lens imaging requires going to ~550 AU. Advanced propulsion systems that can reach 500 AU and beyond in 10-20 year are highly desirable.

Spacecraft propulsion limitations are manifested also at Earth orbit as well. Massive orbital constellations being deployed to provide global services, such as navigation, Earth observations and internet are driving the economic growth. At the same time, rapid proliferation of orbital use faces new challenges, including spacecraft on-orbit servicing of satellites on demand [5, 6] and collision avoidance [7], among others. Such services become increasingly important as the number of spacecraft and orbital debris grow to a critically significant levels [8]. However, at present there are no efficient ways to changing spacecraft orbit, such as performing large orbital plane or altitude changes. In particular, current chemical and plasma engines require either exorbitant amount of fuel or many months of flight time to perform desired orbital maneuvers [9-11]. Future discoveries call for a paradigm shift in propulsion and spacecraft design that is coupled with a new concept

of operations (CONOPS) approaches that will enable faster, cheaper, and massively scalable ubiquitous exploration of the solar system and beyond.

1.2 Spacecraft propulsion overview

Without any forces applied spacecraft follows a prescribed orbital path (a simple two-body problem is assumed here for sake of simplicity of discussion, while second order effects, such as multibody dynamics, are neglected). Orbital maneuvering, such as altitude and plane changes, and spacecraft insertion onto interplanetary and solar escape trajectories, is associated with changing spacecraft velocity (i.e., $\boldsymbol{v}_0(t) \rightarrow \boldsymbol{v}_1(t)$), which may be attained by an applied propulsive force, $\boldsymbol{F}(t)$. The ability of a spacecraft to perform orbital maneuvers is then described by a scalar velocity gain:

$$\Delta v = \int_0^t \frac{|\boldsymbol{F}(t)|}{m(t)} \, dt,$$

(1.1)

here $m(t)$ is a spacecraft mass. Higher velocity gain, Δv, allows broader range of possible orbits and trajectories, and orbits that deviate significantly from an original one. Complex Earth orbital transfers require $\Delta v > 3 \, km/s$. For example, going from low Earth orbit (LEO) at 300 km altitude to a geostationary orbit (GEO) requires $\Delta v = 3.88 \, km/s$, whereas inserting a spacecraft from a parking LEO orbit onto Earth escape trajectory for interplanetary flight needs $\Delta v = 11 \, km/s$. Performing a 90 degree change of orbital plane inclination necessitates $\Delta v \simeq 9 \, km/s$.

Current propulsion systems can be roughly categorized into chemical and electrical propulsion systems. Chemical rockets rely on combustion of fuel to generate thrust, while electric propulsion ionizes the fuel and accelerates the ionized fuel by electric power. For

conventional spacecraft with propulsion originating from fuel exhaustion, the spacecraft velocity gain can be found by Tsiolkovsky's rocket equation:

$$\Delta v = v_{\text{ex}} \ln \left(\frac{m_0}{m_f} \right),$$

(1.2)

where Δv is the velocity change of the spacecraft, v_{ex} is the fuel exhaust velocity that is defined by an engine, m_0 and m_f are the spacecraft mass in the beginning and in the end of the maneuver, respectively.

The limitations of current engines in performing high Δv maneuvers ($\Delta v \gg 3km/s$) is evident from this equation. Relatively small exhaust velocity of chemical rockets $v_{ex} \simeq 3km/s$ [12], according to equation (1-2) requires exorbitant amount of fuel to perform desired high Δv orbital maneuvers. For instance, achieving $\Delta v = 10 \ km/s$ would require 96% of spacecraft mass allocated to fuel – a significant constrain for space flight. Electrical engines, while efficient in delivering high v_{ex} (typically $v_{ex} \simeq 30km/s$ [13]) and thus high Δv with affordable fuel consumption, produce very low propulsive force, $|\boldsymbol{F}|$<<1N, and therefore result in lengthy – months long – orbital transfers [11]. For example, Deep Space 1 – the first spacecraft to use electric propulsion [14] – has achieved $\Delta v = 4.3 \ km/s$ post-launch, whereas Dawn – the first electrically propelled interplanetary mission to Vesta and Ceres – attained $\Delta v = 11 \ km/s$, which is the largest Δv ever achieved. Nevertheless, it took 90 mN Dawn thrusters ~5.5 years to perform the maneuver (noteworthy, that Dawn spacecraft utilized Mars gravity assist to reach the desired orbit). Fast transfer high Δv maneuvers are beyond the reach of either chemical or electrical rockets.

Future of space exploration and space sciences necessitate fundamentally different principles of propulsion and spacecraft design, which can significantly reduce flight and

lead times, and development costs. Many concepts have been proposed to allow for more efficient propulsion in space, such as nuclear propulsion [15], antimatter rockets [16], and even wrap drives. Figure 1.2 shows a chart of different propulsion systems as a function of thrust-to-weight ratio and specific impulse. Photon engines that make use radiation pressure are capable of delivering very high effective specific impulse, well above any other propulsion approach. Ability to harness high specific impulse can pave new ways for space exploration. At the same time, low thrust-to-weight ratio of radiation pressure necessitates novel spacecraft design principles to allow efficient in-space operations. This thesis explores radiation pressure propulsion to push the feasibility limits for future breakthrough fast-transit and deep-space missions with high Δv, as well as studies new regimes of operation in Earth orbital environment.
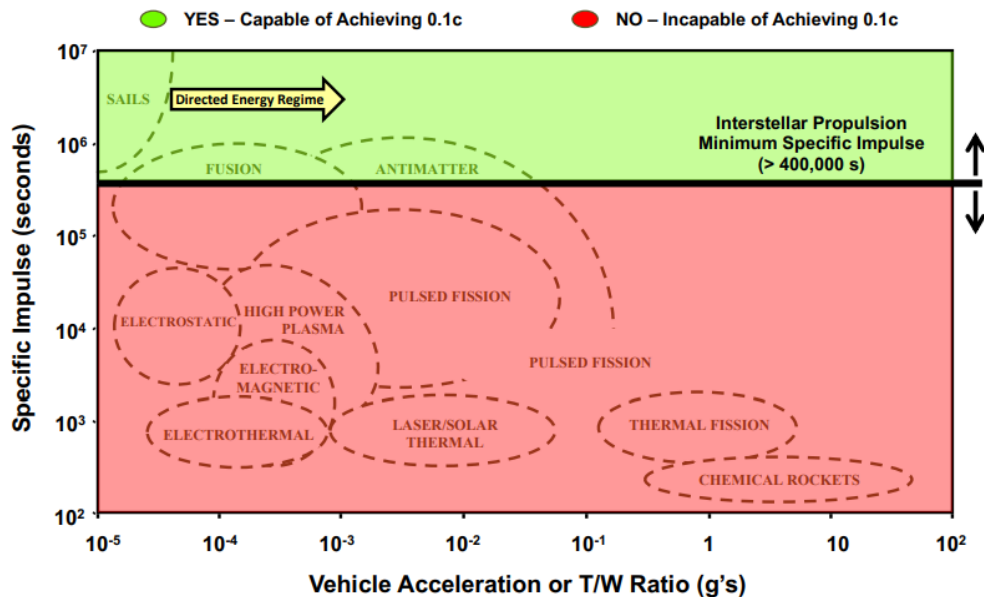
Figure 1.2 Landscape of known in-space propulsion technologies, after [17]. Radiation pressure propulsion ("sails" in the figure) differs fundamentally from other propulsion concepts, and is suitable for fast in-space travel by having high specific impulse.

1.3 Overview of light sailing in-space propulsion

Radiation pressure propulsion differs fundamentally from conventional chemical and electric means of propulsion in use today (see also fig. 1.2). Light sails reflect the incident radiation and generate thrust upon the momentum transfer in reflection. As a result, the need for heavy, expendable propellants employed by conventional onboard chemical and electric propulsion systems is eliminated. The Δv of radiation pressure propulsion increases linearly with the total power incident on the sail and with the illumination time. The potential to generate large Δv enables new vantage points for science observations that are inaccessible or impractical using conventional propulsion methods.
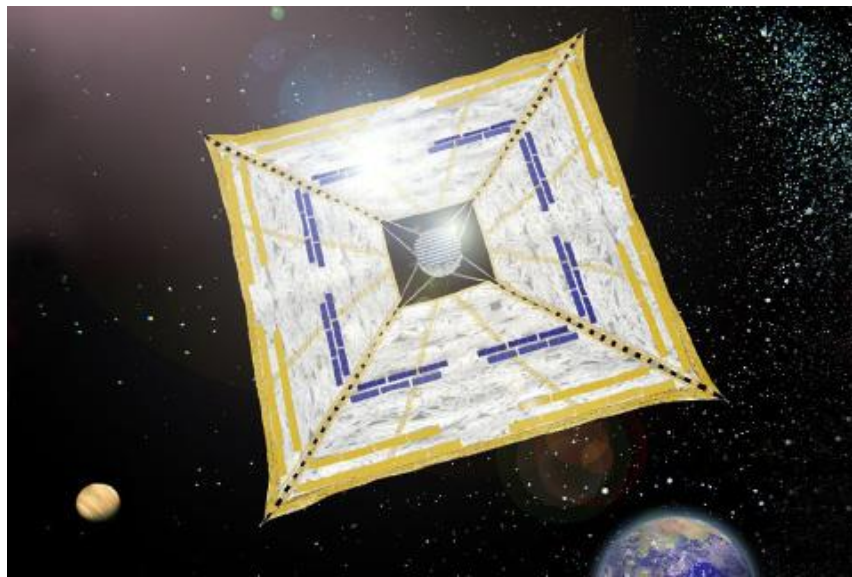
Figure 1.3 Artistic illustration of IKAROS solar sail. Image source: JAXA [18]

Mission concepts based on light sailing have been proposed since the 1980s. The first spacecraft to make use of solar radiation pressure was IKAROS built by JAXA and launched in 2010, Fig. 1.3. IKAROS solar sail made use of solar radiation pressure propulsion as its main way to maneuver in space on a mission to Venus. Soon after IKAROS, NASA successfully launched NanoSail-D in 2010, demonstrating solar sailing

satellite on low Earth orbit. In 2019, another successful low Earth orbit solar sailing satellite, LightSail-2, by The Planetary Society raised confidence in solar sails and paved the way for the first NASA solar sails interplanetary science mission – NEA-Scout (launched in 2022 as a part of Artemis I mission). Proliferation of small satellites and miniaturization of instruments further stimulate development of solar sails. Lighter solar sail spacecraft can be accelerated to even higher velocities enabling novel breakthrough missions. Future solar sail missions would benefit tremendously from getting close to the sun and from ultralight architectures. This is where novel lightweight materials and high durability materials are need. Chapters 3 of this thesis explore such systems.
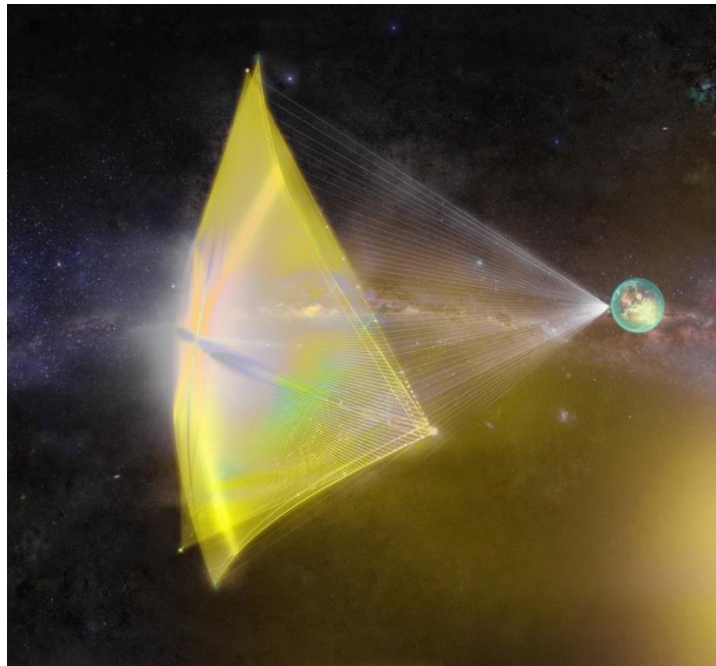
Figure 1.4 Conceptual illustration of Breakthrough Starshot LightSail propelled by a laser array. Image source: Breakthrough Initiatives [19].

Laser beaming can also be utilized for the radiation pressure propulsion. Ideas of using laser beaming as the radiation power source were proposed starting from 1960s, and recently being revisited in the context of interstellar travel. For example, the Breakthrough

Starshot initiative (Fig. 1.4) established in 2016 sets the goal of visiting the neighbor exoplanet Proxima Centauri b with an ultralight "StarChip" propelled by laser radiation pressure propulsion. The laser beaming power is orders of magnitudes larger than the solar radiation at Earth, which allows accelerating an ultralight ~1g spacecraft to ~20% of the speed of light. In this case a StarShot probe would reaching the exoplanet in approximately 20 years. However, ultrahigh beam power and need for ~1g spacecraft challenge materials and spacecraft designs. Chapter 2 of this thesis explores novel photonic designs to enable efficient use of beamed laser propulsion for near-future missions.

Future light sail missions would rely on advanced materials that could handle high power radiation flux. For example, laser sailing would rely on using high power >100 kW lasers for propulsion, whereas solar sailing benefits from maneuvering closer to the sun. In both cases high incident radiation power poses significant challenges on sail materials. In this thesis we explore the material requirements for such high power operation for both laser and solar sailing. Parameter analysis considering tradeoffs on Δv, thermal balance, and spacecraft mass are performed, and from these studies we identify the need to explore advanced thin film materials for radiation pressure propulsion.

1.4 Purpose of study

In the scope of this dissertation two distinctive mission architectures using radiation pressure for breakthrough space exploration and related technologies are discussed. The first approach utilizes laser beaming as the source of radiation pressure to propel ultralight-weight probes (Chapter 2). The second approach discussed in chapter 3 takes advantage of solar sailing for fast transit outer space exploration. For both approaches, we study material parameters, examine related material challenges, and study light-materials interaction and

photonic designs (Chapter 4 and 5). Candidate sail materials are designed, fabricated, and tested. We further discuss proper figures of merits and optimize designs accordingly. In Chapter 6 potential environmental effects on the solar sail materials are examined. The research encompasses both theoretical and experimental work. Finally, we outline a roadmap for future research related to lightsail materials and photonic designs.

CHAPTER 2

Laser Sailing for High Delta-V Missions

In this chapter we study theoretically laser-driven light sailing for Earth orbital maneuvering and for interplanetary missions. Specifically, we show that with relatively moderate laser beam requirements – 100 kW - 10 MW of power and 1-10 m array aperture – a lightweight (≤ 100 g) wafer-scale spacecraft may be propelled to velocities and regimes that are beyond the reach of conventional space propulsion technologies. In particular, we demonstrate that arbitrary Earth orbital maneuvers may be performed in a matter of minutes and show that >10x faster interplanetary flight as compared to today's space missions is possible. Such fast and on-demand maneuvering has a potential for novel space operations and infrastructure. Situational awareness and responsiveness, asset monitoring and refueling, seamless data acquisition, and in-space countermeasures are the few technologies that we believe may emerge.

We introduce figures of merit for such regime of laser sailing and analyze corresponding material and photonic designs challenges. We discuss several examples of nanostructured thin films that may meet desired operation criteria. Finally, we discuss promise of laser-driven lightsailing for Earth orbital use and for fast and scalable solar system exploration.

2.1 Laser sailing propulsion overview

Laser sailing [20-26] fundamentally differs from conventional chemical and electric means of propulsion. Laser sailing harnesses photon radiation pressure from an external

laser source. Without a need to carry energy source and propellant on board, even minute forces of radiation pressure may accelerate a light-weight spacecraft to near-relativistic velocities [20, 23, 25]. Figure 2.1 illustrates conceptually the principles of laser sailing. Here a laser beam is incident on thin light-weight sail (LightSail) that carries a payload. Upon laser beam reflection laser beam photons transfer momentum to push the sail. The radiation pressure force is then given as:

$$F_p \simeq \frac{2}{c} R cos(\theta) P \hat{n},$$

(2.1)

here, a flat specularly reflecting sail is assumed [23], P is the laser power, c is the speed of light, R is the reflectivity of the lightsail, θ is the angle of incidence, and $\hat{\boldsymbol{n}}$ is a normal to a lightsail (Fig. 2.1). As can be seen propulsive force depends only on laser beam power and does not depend on the probe mass (i.e., not constrained by the rocket equation). For sufficiently long illumination time and for sufficiently high incident laser power, laser driven probes can be accelerated to very high velocities.
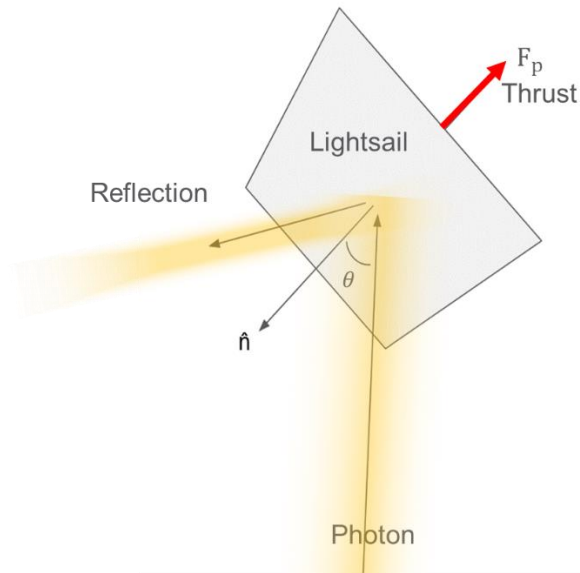
Figure 2.1 Schematic illustration of principles of laser-driven light sailing

Unique capability of laser sailing makes it of great of great promise for future deep space and interstellar missions [20-26]. By making use of laser radiation pressure with sufficiently high-power laser beams, lightweight probes can be accelerated to very high, near-relativistic, velocities [23]. By doing so nearby star systems can potentially be reached in a matter of decades, thus opening a new era for spacefaring civilization. A range of proposals for reaching near-relativistic speeds have been considered [15, 16, 23, 27].

Laser beam sailing was first proposed in the 1960's for interstellar travel [21]. It was suggested that using laser beams allows avoiding extremely high mass ratios when propelling to ultra-high velocities for future interstellar missions. The ideas of laser sailing received subsequent development in works by Robert Forward [26], Geoffrey Landis [24], Jordin Kare [28] and others. In his 1984 proposal [26] Robert Forward assumed a 1000 kg interstellar probe equipped with a 71,500 tons, 3.6 km diameter lightsail pushed by 65 GW laser (Fig. 2.2). To propel such relatively heavy space probe, laser beam needs to illuminate the probe for a considerable amount of time (3-year illumination time was assumed). As such, one of the mission requirements was to keep the laser collimated for a substantially long distance. As a result, laser beamer needed to have 1000 km diameter laser array aperture (in which case even at a distance of 4.3 light-years the laser beam spot is only ~100 km). During 3-years of illumination the probe would propel to 11% of speed of light and reach α-Centauri system in ~40 years. Furthermore, the proposed architecture can be extended to allow for probe deceleration and return to Earth for a roundtrip interstellar mission (Fig. 2.2 shows conceptual illustration of the laser beamer and related mission architecture). However, building a 3.5 km sail as well as 1000 km laser beamer that would operate for 3 years is impractical at this stage of technology development. Recent advances

13

in instrument and spacecraft miniaturization driven by consumer electronics markets, as well as rapid proliferation of laser technology, allows new opportunities for interstellar laser sailing with small mass probes [20, 23, 25, 29].
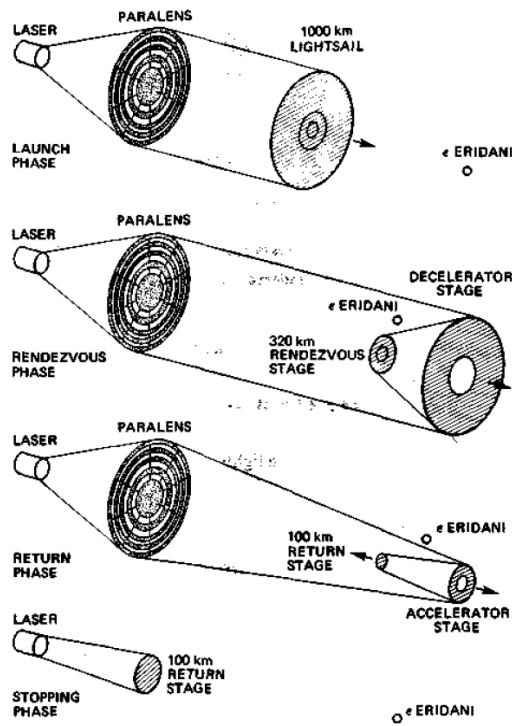
Figure 2.2 Robert Forward assumed a 1000 kg interstellar probe equipped with a 3.6 km diameter lightsail pushed by 65 GW laser. An illustration of laser propulsion for roundtrip interstellar travel after Ref. [26]

A notable example is the Starshot mission concept [20, 23, 25], proposed in 2015. Starshot mission assumes propelling a ~1g spacecraft to ~20% of the speed of light by ~100 GW kilometer square laser array [20, 25]. In this case the probe would reach exoplanet Proxima Centauri b – a potentially habitable planet 4.2 light years away in the closest star system [30] – in about 20 years. Notably, in Starshot the overall duration of laser illumination (i.e., acceleration phase) is <20 minutes. Figure 2.3 illustrates major

14

Starshot mission parameters. While a considerable research and development effort is required, Starshot mission parameters are feasible to achieve with today's technologies with a proper development roadmap [23]. Notably, one of the key innovations making Starshot a feasible mission is the use of an ultralight weight probes (~1 g mass with a ~10 m^2 laser sail). With such a small mass a relatively high radiation pressure force (~1000 N) needs to act only for a very short period of time to propel a 1g space probe to a near-relativistic velocity.
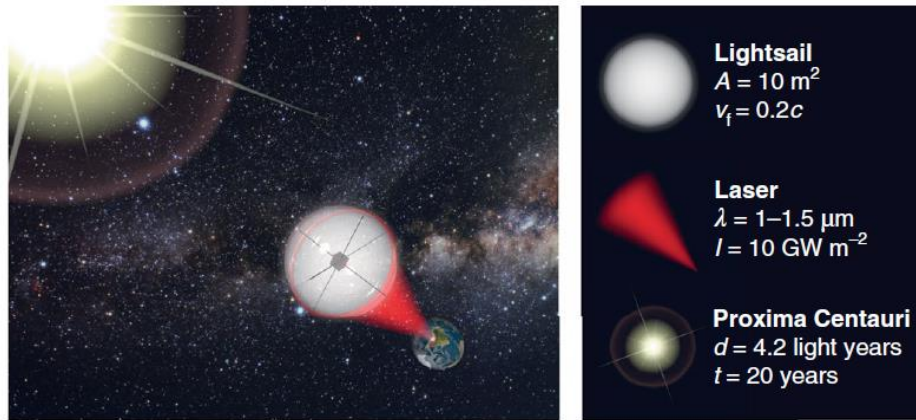
Figure 2.3 Schematic illustration of the Breakthrough Starshot mission concept. Key mission parameters are indicated. After Ref. [23]

Use of high power laser beam (100 GW) and a need for ultralight-weight sails designs ($\sim 10\ m^2$ with $< 1\ \mu m$ thickness) put significant constraints on materials and photonic designs. In [23] a holistic analysis of light sail materials and photonic designs was performed. It was suggested that high refractive index ultralow loss semiconductors such as Si and MoS_2 are needed to minimize laser beam power absorption. Furthermore, a dedicated nanophotonic engineering is needed to enable high reflectivity so that the laser radiation pressure can be exerted, as well as to allow radiative cooling of the system in

space [31, 32]. The search for proper materials and designs is an active research topic these days.

Despite a considerable effort in the context of the Starshot mission concept fueled by private foundations, a little attention has been drawn to understanding precursor missions with smaller laser beams. Such an analysis is performed in this work, where we examine possible missions with significantly lower power laser beams (~1 MW) with smaller apertures (~10 m^2) – a laser beamer that can be built already today. We will show that use of lower power beams significantly changes requirements set on materials and photonic designs, compared to common anticipation in the context of Starshot program. We further show that such "low power" laser sailing has advantages for Earth orbital operations and for interplanetary fly-by missions.

2.2 Small satellite missions overview

As mentioned in the previous section, ultralight weight probes (<100 g) is the main prerequisite for laser sailing missions in the foreseeable future. Below we provide a brief outlook on the proliferation of small satellite technology for space exploration.

Driven by instrument miniaturization and rapid growth of ride sharing opportunities to low Earth orbit (particularly fueled by recent success of reusable rocket technology), small satellites have gained considerable traction from government and private sectors in the last decade. Of a particular interest are CubeSats, which, originally originated as an educational program for students, now play an increasingly important role for science missions. Notable example of recent successful CubeSat missions are CAPSTONE [33] and MarCO [34] missions. The global CubeSat market is experiencing an explosive growth.

16

Hence, it was valued at $210.1 million in 2019, and is projected to reach $ 491.3 million by 2027 [35]. Such rapid growth of CubeSat technologies is a good indicator that future space missions will rely more on miniaturized systems.

Beyond CubeSats an active research is in the fields of Femtosatellites (<100g) and even ChipSats (<1g). Such ultra-lightweight probes are an emerging class of satellites, which owing to their low mass and ultralow cost are of a great promise for distributed space systems and swarm architectures [36-38]. Furthermore, a constellation of such ultra-small satellites has potential to improve resiliency of the overall space architecture. Ultralight probes also allow for trade-offs in individual sensor performance (such as lower imaging resolution) in return for a wider coverage [39].

However, small mass budget also presents its challenges. For example, lightweight probes constrained with mass, and therefore the amount of propellant, have little ability to maneuver in space. The lack of agility limits such smallsats to orbits that they are launched into, and therefore it is hard to perform multipurpose or complete complex tasks. The lack of propellant further implies shorter mission timelines, which unnecessarily drives the cost and has implications for orbital debris.

With laser sailing issues related to propulsion and orbital maneuvering can be circumvented. Laser propulsion relies on energy purely from a laser beaming station and does not require carrying propellant on board of the spacecraft. Figure 2.4 shows our vision for a laser driven architecture with ultra-lightweight probes and constellations. Laser sailing could potentially enable fast transit and high delta-V maneuvers at low Earth orbits.
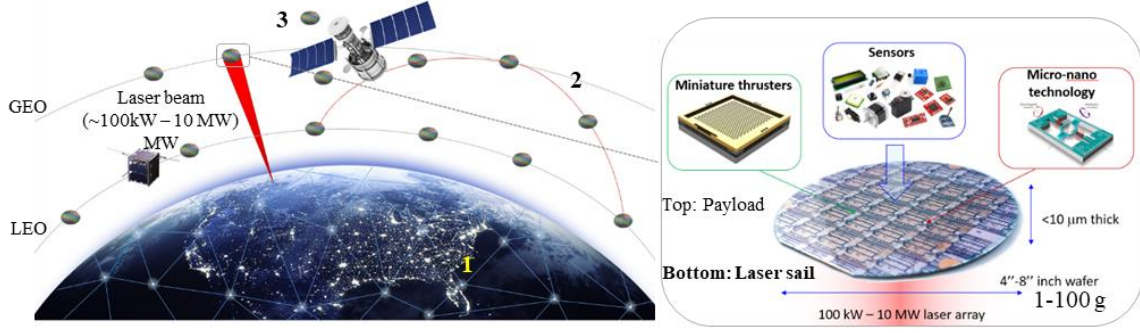
Figure 2.4 Concept of laser propelled wafer scale femtosatellites. (Left) Schematic illustration of some of the applications of such femtosatellites: 1) seamless sensor networks for Earth and space observations and situational awareness, 2) fast orbital transfer for inspection and fuel delivery, 3) inspection of large and costly space assets. Beamed laser propulsion is key to enabling agile high Δv maneuvering and fast on-demand orbital transfers. (Right) Schematic illustration of a wafer satellite. The top side carries all of the electronics, sensors and attitude controls, the bottom is a highly reflective laser sail surface.

To further illustrate the capabilities of laser prolusion we analyze the corresponding velocity gain:

$$\Delta v = \int_0^t \frac{\left|\boldsymbol{F}_p(t)\right|}{m} dt = \frac{2P}{mc} t,$$

(2.2)

where t is the total illumination time and $m = m_s + m_p$ is the overall mass of the laser propelled spacecraft, m_s is the mass of the lightsail, and m_p is the mass of the payload, i.e., all other spacecraft systems. In our analysis for the sake of comparison we shall assume normal incidence ($\theta = 0$), unity reflectivity ($R = 1$) and negligible absorbance at the laser wavelength (see also Eq. (2.1))

Clearly, a light-weight spacecraft under a high enough laser power can attain very high velocity gain, Δv, in a relatively short period of time. Figure 2.5(a) compares Δv possible with $P/m = 1MW/g$ (compare to $\sim 100\ GW/g$ considered in Starshot program [20]) with that possible with the state-of-the-art electric and chemical engines. In 600 s (~10 minutes) of illumination, the light-driven spacecraft gains Δv surpassing that of best chemical rockets [40, 41]. After 2000 s of illumination Δv exceeds that of Dawn attained in 5.5 years and after Mars gravity assist [42]. Figure 2.5(b) further examines capability of laser-driven lightsailing. Evidently, very high Δv needed to perform arbitrarily complex maneuvers may be reached in a relatively short time (minutes to hours) with even moderate laser power requirements$\simeq 100\ kW/g$.
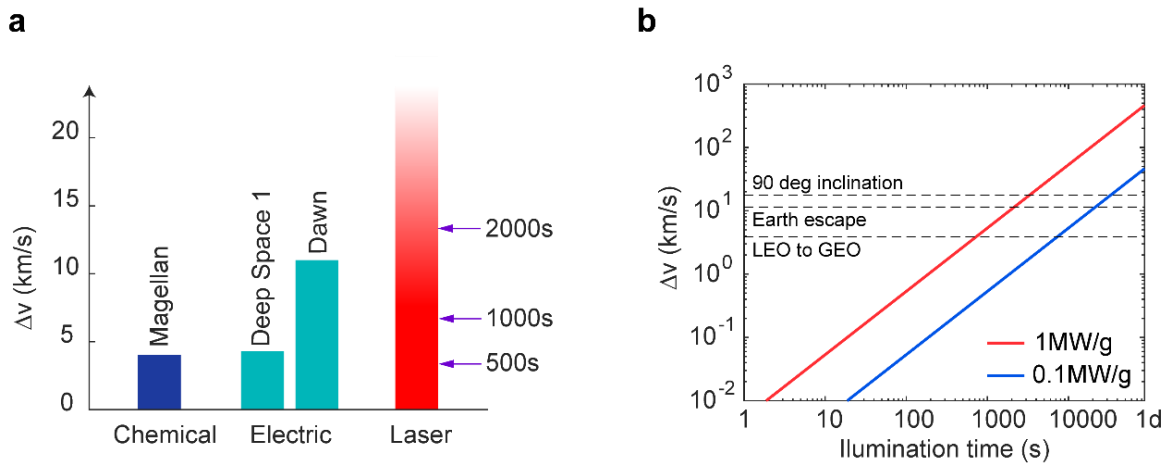
Figure 2.5 Comparison of laser sailing to chemical and electric propulsion. (a) In-space velocity gain attained by electrical and chemical engines, and laser sailing. (b) Velocity gain with illumination time for two different values of laser power per spacecraft weight. Dashed lines indicate velocity gain to perform respective orbital maneuvers.

2.3 Laser beamer considerations for in-space propulsion

In this section we discuss several high level requirements on the laser beamer for future laser driven propulsion architectures.

As mentioned earlier one of the key requirements for laser propulsion is the ability to focus laser beam on the spacecraft. Therefore, effects that may affect focusing and/or laser beam quality need to be accounted. Light diffraction is one of the major effects causing beam spreading and power density attenuation with propagation [43]. Being of a fundamental nature laser beam diffraction is observed in both atmosphere and free space.

Consider, for example, a phased array laser system emitting at a wavelength λ with a continuously filled aperture D (see schematic in Fig. 2.6 left). It is possible to show that the beam power can be almost entirely focused on a target with radius w up-to a maximum distance

$$Z_{max} = \frac{\pi}{2} \frac{Dw}{\lambda}.$$

(2.3)

That is, up-to a range Z_{max} power losses due to laser beam diffraction do not occur, provided that the phased array laser may be reconfigured to focus on a desired target within that range (for example by controlling the phase across the entire aperture). Fig. 2.6 left shows schematically this regime of operation. Beyond Z_{max} diffraction effects play an important role and should be considered. Notably, for the purposes of in-space and high altitude laser propulsion the laser beam is focused on a target at $z > 50\ km$. Therefore, within the sensible atmosphere (up-to ~7-10 km), where effects of turbulence, atmospheric absorbance, and thermal blooming are dominant, laser beam profile is nearly uniform forming a beam column with a radius $D/2$.

Beyond distance Z_{max} any phase profile adjustments at the phased array side will not be able to compensate for beam diffraction. Hence, for high altitude propulsion and manipulation of a target with an effective cross section of 10 cm, a ground based laser array of a diameter of 50 cm will suffice. For in-space propulsion, to propel a 10cm space target (i.e,. laser sail) a 10 m in diameter array would be needed; the array size may be reduced by making spacecraft with a larger sail radius (e.g., 1 m target may be propelled by a 1 m array at an altitude of 1000 km).
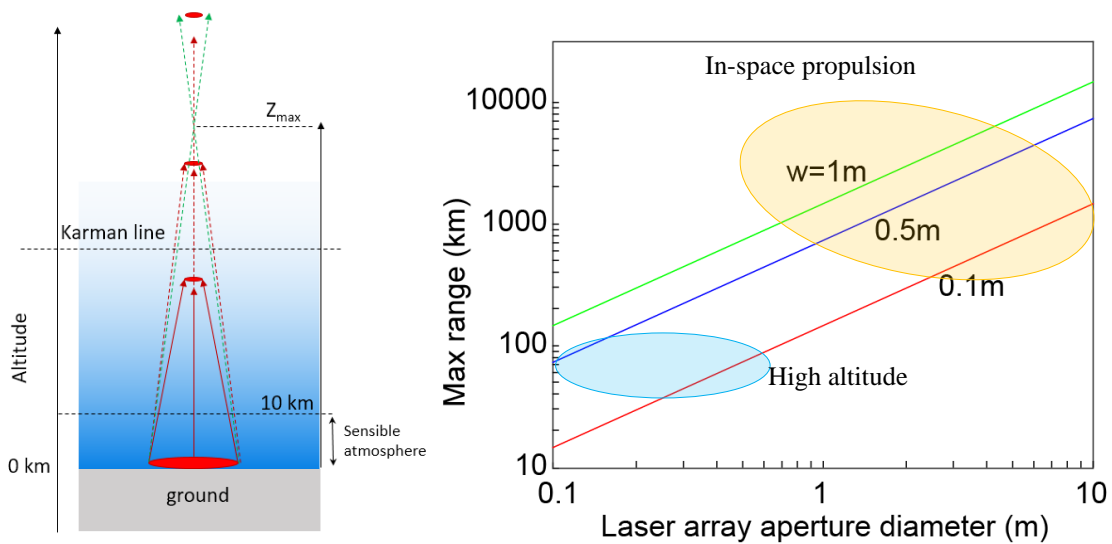
Figure 2.6 (Left) Schematic illustration of laser beam propagation and diffraction. For a given ground based laser array aperture the beam can be near entirely focused on a given target up-to a maximum range Z_{max}. Beyond that range due to laser beam diffraction the beam cannot be focused on the target anymore. (Right) maximum distance at which optimal focusing on a target of radius w can be achieved. Highlighted areas denote the regimes of interest for high altitude operation (50-100 km) and for in-space propulsion (1000km and more). Here $\lambda = 1.06\ \mu m$.

21

Atmospheric absorbance is another important factor that should be considered when analyzing high power ground-to-space beaming [43]. The power attenuation due to atmospheric absorbance for sites with a clear sky (i.e., low concentration of particulates, dust, water vapor) may be with a great approximation described by an extinction coefficient $K(z) = K_0 \exp\left(-\frac{z}{h_0}\right)$ that being proportional to pressure exponentially decays with altitude z, here K_0 is the extinction coefficient at the sea level and $h_0 \simeq 7km$ and denotes sensible atmosphere.

The absorbance of a laser beam propagation from ground to space is then found as:

$$A(h) = \exp\left[-K_0 h_0 e^{-\frac{z_0}{h_0}}\right],$$

(2.4)

here, $z = z_0$ is the elevation (i.e., height above the sea level) of the site where ground laser is based. The extinction coefficient $K(z)$ varies not only with altitude but also with site location. More polluted and humid areas imply higher absorption. In contrast, remote locations with generally dry atmosphere possess the lowest atmospheric extinction (e.g., deserts, dry mountain ranges, Antarctic region etc). Notably, sites with higher elevation z_0 also possess lower absorbance due to a reduced air density. In these regions absorption above the sensible atmosphere, i.e., for $z_0 \simeq h_0 \simeq 7km$, is very small. Astronomy community has developed an extensive map and survey of sites with near excellent atmospheric transmittance. In Fig. 2.7 we plot data collected for *Mauna Kea* [44] – one of the largest observatory sites in the world. Important to mention that the site is located at an average altitude of 4.2 km.
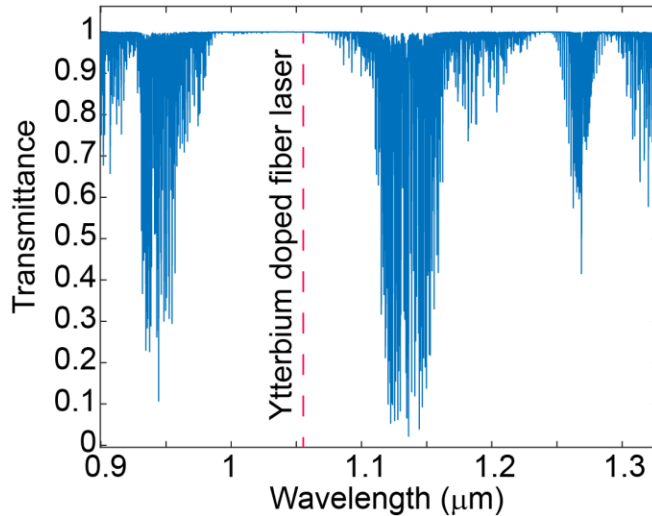
Figure 2.7 Atmospheric transmission spectrum through atmosphere above Mauna Kea.

Dashed line shows the frequency range of the Ytterbium doped fiber laser ($\sim 1.06\ \mu m$)

Clearly, a large transparency window exists at the near infrared frequency range. Hence, the transmission at 1.06 µm – wavelength of high power Yb doped fiber lasers commercially available – is >0.99995. That is, less than 0.005% of laser power is absorbed by atmosphere. We note that the transparency window is rather large and hence allows selection of lasers with different wavelengths. In the rest of the sections of this chapter, we choose the wavelength of the laser for laser sailing to be 1.06 µm. Importantly, at this wavelength a range of relatively low cost lasers are available, which is an important consideration for high power laser beamer architectures.

Of course, in a practical laser beamed system many other issues need to be accounted for, such as atmospheric turbulence, thermal blooming, coherent beam combining to yield high beam powers, pointing and stability, as well as many other related issues [45-48]. These topics are active areas of research in the context of directed energy for power delivery and for communications [43]. Their detailed outlook is beyond the scope of this thesis.

2.4 Orbital dynamics with laser sailing.

Let us now examine utility of laser sailing for Earth orbital maneuvering and for interplanetary flight. Figure 2.8 provides a conceptual illustration of the architecture we study in this section. In contrast to prior interstellar works [21, 23, 26] we focus on understanding laser sailing with moderate power levels (100 kW – 10 MW) and relatively small laser beamer apertures (1- 50 m).
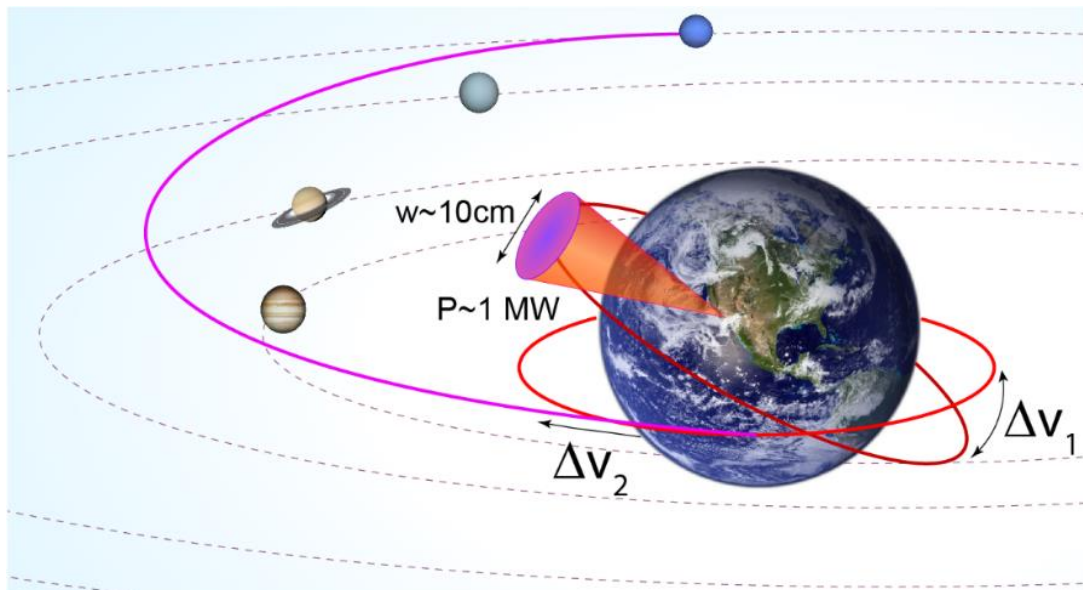
Figure 2.8 Schematic illustration of laser sailing for Earth orbital maneuvering and for fast transit interplanetary missions. Here a laser beam with ~1MW power propels a wafer-scale (~10 cm) lightsail. Powered by laser propulsion such a spacecraft can perform highly energetic orbital maneuvers that require very large velocity gain, Δv. Two examples (not to scale) of such maneuvers are schematically shown: inclination change at the low Earth orbit and fast transit to Neptune and beyond.

For the sake of concept demonstration, an idealistic scenario of normal incidence and perfect reflectivity (i.e., $\theta = 0$ and $R = 1$) is assumed. Furthermore, it is assumed that

during the illumination phase the force of radiation pressure is constant (i.e., $\boldsymbol{F}_p = const$).

In practice one should consider effects of oblique incidence, Earth rotation and orbital orientation with respect to a laser beam – effects that depend on a particular mission and its objectives. Study and analysis of these effects is a subject of future studies extending beyond this thesis. Despite its simplicity our analysis provides a guideline for the efficiency of laser propulsion as compared to other means of navigating in space.

2.4.i Fast transit Earth orbital transfers.

Here we study use of laser sailing for Earth orbital maneuvering [49]. In particular, we consider two characteristic orbital maneuvers: a transfer from a low Earth orbit to a geostationary orbit and a 90 degree orbital plane inclination change maneuver. Provided that the range of laser operation is limited at most by the geostationary orbit ($z_{GEO} \simeq$ 35,700 km altitude), we assume that all of the laser power may be focused on the lightsail. Such assumption is justified when laser aperture diameter, D, and lightsail radius, w, meet Rayleigh length criterion [20, 43]: $Dw > \frac{2}{\pi} z_{GEO} \lambda$, where λ is the laser wavelength (in our case $\lambda \simeq 1\ \mu m$ is assumed). For instance, a sail with $w = 1\ m$ would require a laser with an aperture $D \simeq 26\ m$ (compare with the 30m diameter primary mirror of the Thirty Meter Telescope under construction). However, we stress that most practical scenarios are limited to low and medium Earth orbits that require a much shorter operation range ($z \leq 1000\ km$), and therefore a significantly smaller laser array.

To examine trajectories and orbital maneuvers we use Runge-Kutta numerical methods to calculate spacecraft position and velocity. A brief excerpt of the algorithm for a two dimensional case (i.e., in an orbital plane) is provided below. The equation of motion

is dictated by Newton's second law in the presence of the force of gravity $(-\frac{GMm}{r^2}\hat{r})$ and

laser radiation pressure, $\boldsymbol{F_p}$:

$$m\frac{d^2r}{dt^2} = -\frac{GMm}{r^2}\hat{r} + \boldsymbol{F_p} = \boldsymbol{F}$$

(2.5)

By denoting $\frac{d\vec{r}}{dt} = \vec{u}$ and $\frac{d\vec{u}}{dt} = \frac{F}{m} = f(\vec{r})$ we apply the Runge-Kutta algorithm and obtain

the following set of iterative equations:

$$\begin{cases} \vec{k}_{r1} = \vec{u}_i \Delta t \\ \vec{k}_{u1} = f(\vec{r}_i)\Delta t \end{cases},$$

$$\begin{cases} \vec{k}_{r2} = (\vec{u}_i + \frac{f(\vec{r}_i)\Delta t}{2})\Delta t = (\vec{u}_i + \frac{\vec{k}_{u1}}{2})\Delta t \\ \vec{k}_{u2} = f(\vec{r}_i + \frac{\vec{u}_i\Delta t}{2}))\Delta t = f(\vec{r}_i + \frac{\vec{k}_{r1}}{2})\Delta t \end{cases},$$

$$\begin{cases} \vec{k}_{r3} = (\vec{u}_i + \frac{\vec{k}_{u2}}{2})\Delta t \\ \vec{k}_{u2} = f(\vec{r}_i + \frac{\vec{k}_{r2}}{2})\Delta t \end{cases},$$

$$\begin{cases} \vec{k}_{r4} = (\vec{u}_i + \vec{k}_{u3})\Delta t \\ \vec{k}_{u2} = f(\vec{r}_i + \vec{k}_{r3})\Delta t \end{cases}$$

(2.6)

The position ($\vec{r}$) and velocity ($\vec{u}$) from one point to another can thus be related by:

$$\begin{cases} \vec{r}_{i+1} = \vec{r}_i + \frac{1}{6}(\vec{k}_{r1} + 2\vec{k}_{r2} + 2\vec{k}_{r3} + \vec{k}_{r4}) \\ \vec{u}_{i+1} = \vec{u}_i + \frac{1}{6}(\vec{k}_{u1} + 2\vec{k}_{u2} + 2\vec{k}_{u3} + \vec{k}_{u4}) \end{cases}$$

(2.7)

Figures 2.9 (a-c) show calculated altitude change and plane change maneuvers for several different laser powers and spacecraft masses. Figures 2.9 (a) shows calculations of altitude transfers assuming 1 MW laser beam and 1 g probe. Fast, quasi-impulsive transfers on par with chemical rockets are possible in this case [49, 50]. From the calculation, it takes total of 583 s of illumination time (~10 min) to insert a spacecraft onto LEO to GEO transfer orbit (Fig. 2.9(a)). A 90 degree plane change maneuver requires even higher $\Delta v \simeq 10\ km/s$ which results in a longer illumination time needed (total of ~40 minutes assuming 1 MW/g) (Fig. 2.9(c)). Note that such plane change maneuvers are beyond the reach of chemical rockets at present. With higher power per spacecraft mass (i.e., larger P/m ratio) even faster transfers are possible. On the contrary, by relaxing the transfer time constraint, orbital maneuvers may be performed with lower power lasers (see also Fig. 2.5(b)). Hence, by requiring that a transfer is accomplished with total of 1 day of illumination time, we find that a $m = 10\ g$ spacecraft can be transferred from LEO to GEO by $P \simeq 100\ kW$ laser (Fig. 2.9(b)), while 90 deg. orbital plane change maneuver (Fig. 2.9(d)) is possible with $P \simeq 340\ kW$ laser. Slow transfer trajectories in Figs. 2.9(b) and 2.9(d) resemble those attained by electric engines [11, 50], however, unlike electric rockets these maneuvers are performed within 1 day (compare with Dawn spacecraft that took >5 years to attain post-launch $\Delta v \simeq 11\ km/s$ [42]). Calculations presented in Fig. 2.9 evidently show that laser propulsion offers a fundamentally different regime of operation, beyond the reach of electrical and chemical rockets. While our study pertains to an idealistic scenario, it provides a guideline for the efficiency of laser propulsion as compared to other means of space propulsion.
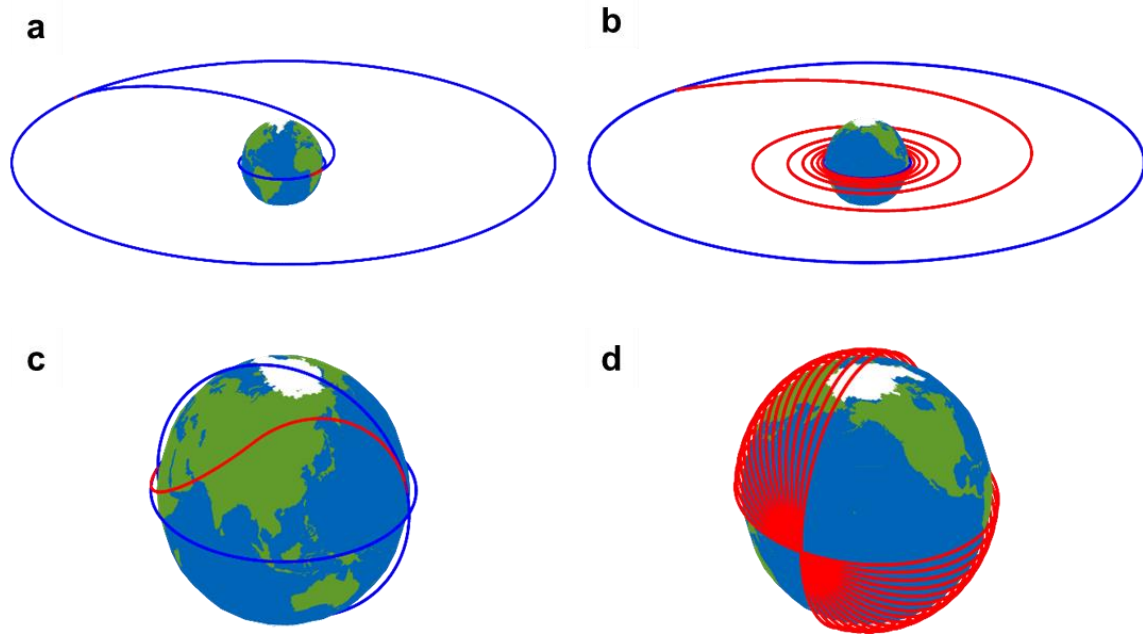
Figure 2.9 (a) and (b), Calculated orbital transfers form LEO to GEO for 1 MW/g and 10 kW/g, respectively. (c) and (d), Calculated 90 deg. inclination change maneuvers for 1 MW/g and 34 kW/g, respectively. In (a)-(d) highlighted parts of the trajectory denote phases of active laser propulsion.

Evidently laser sailing can provide new capabilities for orbital transfers and maneuvering and enables a new class of fast transit missions.

2.4.ii Interplanetary missions with laser sailing.

Next, we examine utility of laser sailing for fast-transit interplanetary and deep space exploration with light-weight laser driven probes. Launching any spacecraft onto an interplanetary mission or solar escape trajectory requires placing a spacecraft onto hyperbolic Earth escape trajectory [49]. Once on a hyperbolic Earth escape trajectory a spacecraft will reach the "edge" of the Earth's gravity well (i.e., boundary of Earth's sphere of influence at $\sim 9.29 \times 10^6\ km$) and enter interplanetary medium where its astrodynamics

is dominated by the solar gravity, Fig. 2.10. In the context of interplanetary and deeps space travel it is the velocity at the boundary of Earth's sphere of influence, v_{inf}, that dictates spacecraft's capability for exploring far reaches of space: the higher is the velocity v_{inf} the further out and faster the spacecraft will reach its target [49, 51-54].
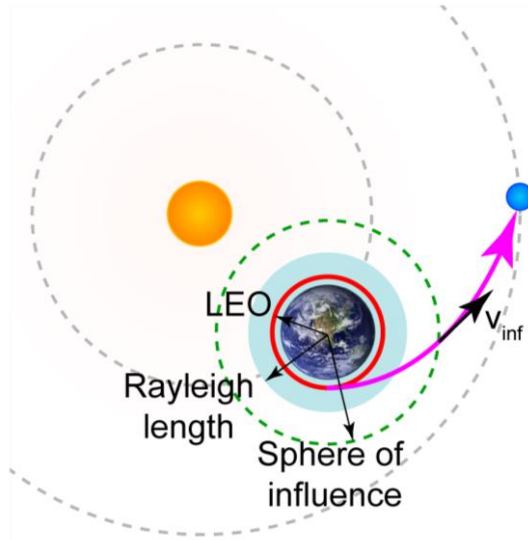
Figure 2.10 Conceptual illustration of the interplanetary transfer. Starting from LEO a lightsail is inserted onto a hyperbolic Earth-escape trajectory.

In Fig. 2.11 we plot v_{inf} as a function of laser power, P, and laser operation range, $z = \frac{\pi}{2}\frac{Dw}{\lambda}$ [43], that is, a distance over which lightsail can be continuously accelerated by a well-focused laser beam. Here we assume $w = 10\ cm$ lightsail and $m = 1\ g$ overall spacecraft mass. For a $w = 10\ cm$ lightsail the operation ranges of interest correspond to laser apertures with diameters ranging from $D = 2m$ to $D = 50m$. We observe that even with these moderate conditions (as compared to previous studies [20, 23]) velocities exceeding that needed for solar system escape [49, 54] can be reached (i.e., $v_{inf} > 12.2\ km/s$). Specifically, velocities 5 times higher than that of the New Horizon spacecraft

[52], a recently launched probe for Pluto and Kuiper exploration, are possible. Clearly, with such high velocities new opportunities for outer solar system exploration emerge.
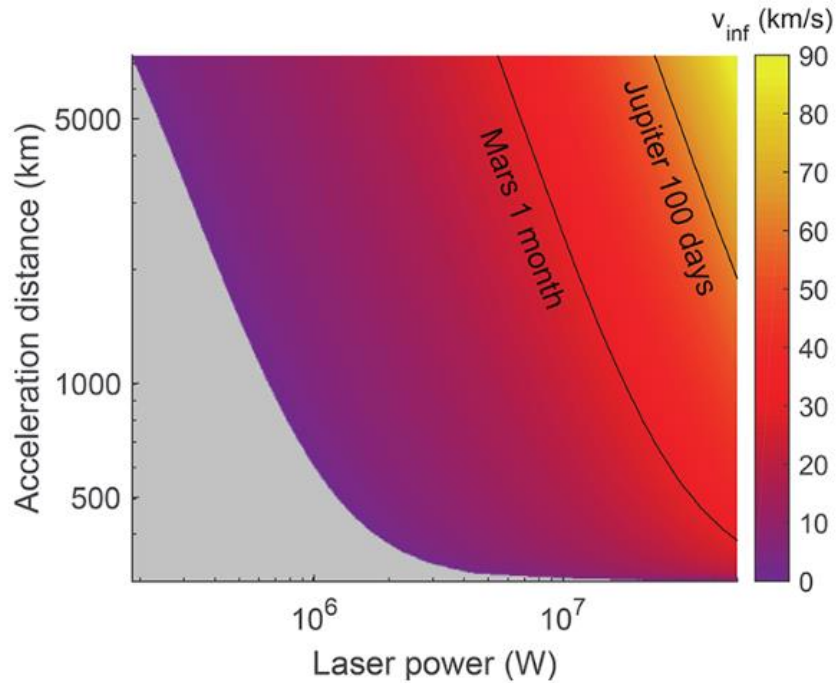
Figure 2.11. Lightsail hyperbolic excess velocity, v_{inf}, as a function of laser power and acceleration distance.

In this context, we draw a comparison between the spacecraft acceleration method discussed here and the traditional gravity assist maneuver employed in previous interplanetary and interstellar missions. Figure 2.12 illustrates the relationship between the velocity of Voyager 2 and its distance from the sun. Unlike Voyagers, which utilized gravity assist maneuvers around gas giants to achieve solar escape velocity, laser sailing allows reaching the solar escape velocities by accelerating the probe within the Earth's sphere of influence. Laser sailing eliminates the need for gravity assist maneuvers, reducing dependence on planetary phasing and allowing for a more flexible launch window.
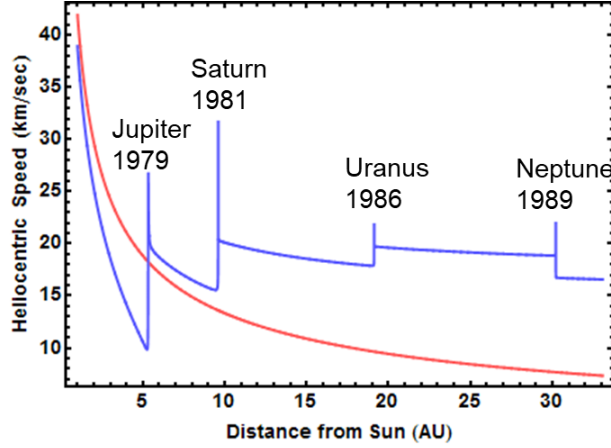
Figure 2.12 The velocity of Voyager 2 is plotted against its distance from the sun. The blue curve represents the velocity of Voyager, while the red curve depicts solar escape velocity at various distances. Voyager 2 achieved its velocity through flybys of four planets, utilizing gravity assist.

Important to note that the actual transit time to a given planet depends on its phasing with Earth (i.e., mutual positions of planets about the sun at any given moment of time [49, 50]), and can be found by solving a respective astrodynamics problem [50]. We implemented Lambert's equation to estimate the time of flight (TOF) to planets in the solar system. Assuming a restricted two-body problem, per Lambert's problem time of flight between two positions in space can be expressed as follows:

$$TOF = 2\sqrt{\frac{a^3}{GM}}\left(\alpha - \beta - (sin\alpha - sin\beta)\right)$$

(2.8)

where $\sin^2\left(\frac{\alpha}{2}\right) = \frac{s}{2a}$, $\sin^2\frac{\beta}{2} = \frac{s-c}{2a}$, and $s = \frac{r_1+r_2+c}{2}$, c is the distance between starting point and destination point, M is the mass of the sun, G is the gravitational constant. For interplanetary transfers a heliocentric picture is assumed with a starting point corresponding to Earth and ending point is a respective destination planet. Knowing origin

31

and destination in the heliocentric reference frame, distance c can be easily determined from simple trigonometric relations and will depend on the phasing between Earth and the destination planet. In Eq. 2.9, a is the semi-major axis of a transfer orbit connecting the origin and destination and depends on the spacecraft insertion velocity (i.e., spacecraft velocity in the heliocentric reference frame, $\boldsymbol{v}_{sc} = \boldsymbol{v}_E + \boldsymbol{v}_{inf}$, where $\boldsymbol{v}_E$ is Earth's orbital velocity. Now the major challenge is to identify the angle between $\boldsymbol{v}_{inf}$ and $\boldsymbol{v}_E$. Note that the magnitude of $|\boldsymbol{v}_{inf}| = v_{inf}$ in an idealistic scenario studied here is dictated solely by laser beamer parameters only (i.e., aperture and power; see Fig. 2.11).

To solve this problem, we consider specific energy relation. By denoting r_0, and v_0 as initial position and velocity of the spacecraft (i.e., at Earth in heliocentric frame), we obtain the following expression:

$$\varepsilon = \frac{v_0^2}{2} - \frac{\mu}{r_0} = -\frac{\mu}{2a},$$

(2.9)

Assuming the sun is at the focal point F of the transfer orbit, we solve for the other focal point F':

$$\begin{cases} |F' - r_d| = 2a - |r_d| \\ |F' - r_0| = 2a - |r_0| \end{cases}$$

(2.10)

where r_d is the heliocentric distance to the target planet. From this set of equations we can find F' for elliptical or hyperbolic transfer orbits. By knowing F, F', and a, we can then find the transfer orbit periapsis r' as follows:

$$\begin{cases} |r'| = a - \dfrac{|F' - F|}{2}, & \textit{if elliptical} \\[2mm] |r'| = a + \dfrac{|F' - F|}{2}, & \textit{if hyperbolic} \end{cases}$$

$$(2.11)$$

Employing the expression for the specific energy, we find the velocity at the periapsis of the transfer orbit, v':

$$\varepsilon = -\frac{\mu}{2a} = \frac{|v'|^2}{2} - \frac{\mu}{|r'|} \Rightarrow |v'| = \sqrt{2 \times \left(\varepsilon + \frac{\mu}{|r'|}\right)}$$

$$(2.12)$$

Once the transfer orbit is fully determined, we can find spacecraft state vector $\boldsymbol{v}_{sc}$ and $\boldsymbol{r}_{sc}$ at any given point on the transfer orbit. Therefore we can establish the initial velocity vector $\boldsymbol{v}_0 = \boldsymbol{v}_{sc,0}$ at Earth in the heliocentric frame. The required excess velocity v_{inf} is then calculated as:

$$v_{\text{inf}} = \sqrt{v_{sc}^2 + v_E^2 - 2v_{sc}v_E \cos(\phi_0)}$$

$$(2.13)$$

where v_{Earth} is the orbital speed of Earth, and ϕ_0 is the angle between vector $\boldsymbol{v}_0$ and $\boldsymbol{v}_E$. Also, for a given semi-major axis a, the time of flight to the destination is found as follows:

$$TOF = \begin{cases} \sqrt{\dfrac{a^3}{\mu}}\,((\alpha - \sin(\alpha)) - (\beta - \sin(\beta)), & \textit{if elliptical} \\[4mm] \sqrt{\dfrac{a^3}{\mu}}\,((\sinh(\alpha) - \alpha) - (\sinh(\beta) - \beta), & \textit{if hyperbolic} \end{cases}$$

$$(2.14)$$

where

$$\alpha = \begin{cases} 2\sin^{-1}\sqrt{\dfrac{r_0 + r + c}{4a}}, & \textit{if elliptical} \\[4mm] 2\sinh^{-1}\sqrt{-\dfrac{r_0 + r + c}{4a}}, & \textit{if hyperbolic} \end{cases}$$

$$(2.15)$$

$$\beta = \begin{cases} 2\sin^{-1}\sqrt{\dfrac{r_0 + r - c}{4a}}, & \textit{if elliptical} \\[4mm] 2\sinh^{-1}\sqrt{-\dfrac{r_0 + r - c}{4a}}, & \textit{if hyperbolic} \end{cases}$$

$$(2.16)$$

The complete derivation of the time of flight equation is provided in Ref. [55]. Figure 2.13

provides a geometric representation of the process of finding v_{inf}.
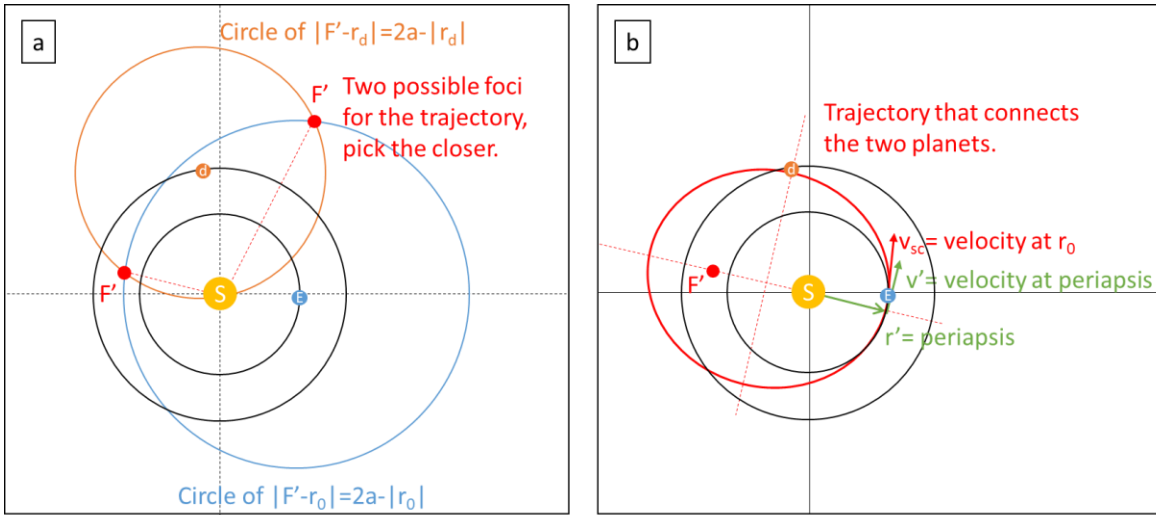
Figure 2.13 (a) The analysis starts by finding the imaginary focal point F', which can be

found through simple geometric relations (in this case at the intersection of two circles

with centers at the origin, i.e., Earth, and destination planets). Solution for F also allows

finding apse line and semimajor axis. (b) Once parameters of the orbit are known, once

can transfer depict an orbit and find velocity of the spacecraft at any point of the orbit..

Figure 2.14 depicts calculated transit times for all possible orientations between

Earth and other planets of the solar system. By solving the Lambert's problem, we find that

with $v_{inf} = 50 km/s$ Mars may be reached in 20 days (*cf.* with 200 days it took

Perseverance rover to arrive Mars), Jupiter in 120 day (*cf.* with 5 years of transit time for

Juno mission [1]), Pluto in 1000 days (*cf.* with 10 years of transit time for the New Horizons

[52]), and 100 AU in 10 years (*cf.* with 45 years for Voyager 1 [54]). The capability offered

by laser sailing even at moderate power and spacecraft requirements discussed here may

open new avenues for missions to interstellar space and capturing interstellar objects [56].

Such missions may also set a ground for future interstellar flight [20, 25].
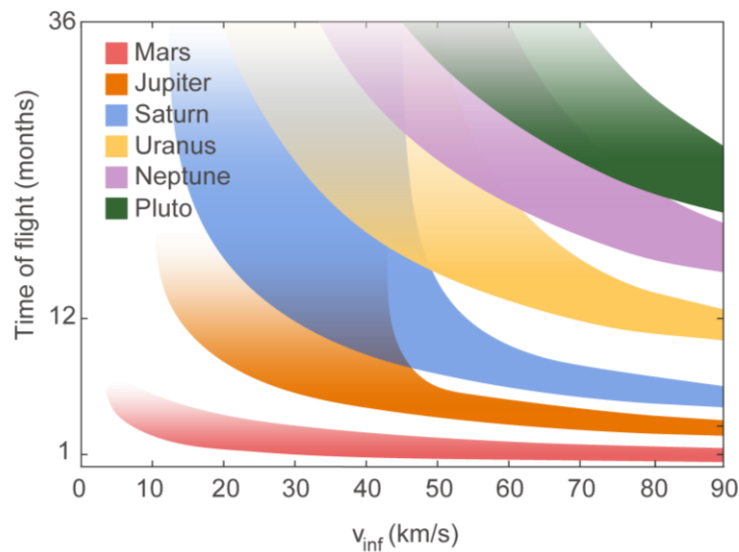
Figure 2.14 Calculated time of flight to different planets of the solar system depending on

the value of v_{inf}. Here the shaded "bands" correspond to possible planetary orientations

with respect to Earth.

Analysis of Earth orbital transfers and interplanetary transfers clearly shows that laser sailing can allow fast transit missions with small mass probes already with moderate laser beam power requirements. At the same time, the study we have performed so far assumes an idealistic system with a perfect reflection (i.e., near-unity momentum transfer) and ability to control the radiation pressure thrust vector in a desired direction. Future detailed studies are needed to account for practical cases going beyond these assumptions. For instance, in a realistic case the reflectivity, i.e., efficiency of radiation pressure momentum transfer would depend on the angle of laser beam incidence with respect to the sail normal. Deviation of the sail shape from a perfectly flat sail and laser beam profile different from the Gaussian would also need to be accounted to calculate actual thrust vector. Finally, while with metasurfaces [57-59] the direction of thrust vector can be decoupled from the surface normal allowing to induce radiation pressure force in desired directions, angle dependence of radiation pressure also needs to be considered in practical mission application scenarios.

2.5   Understanding Lightsail photonic design requirements

Orbital maneuvers discussed in the previous section require use of relatively high power lasers: ~100kW – 1MW to propel 1-10 g spacecraft. Notably, this regime of operation is drastically different from that of Starshot [20, 23, 25]. Specifically, a more than 4 orders of magnitude smaller laser power puts a different constrain on lightsail design [31, 32, 45, 60, 61], suggesting conceptually different performance metrics. Lower laser power implies that a wider class of materials may be used, beyond those considered in Starshot program [23]. Whereas shorter operation distances suggest that smaller area sails

with a radius on the order of 10 cm, and, hence, with a lower mass, m_s, may be used. In fact, the concept of operations considered here suggests that $m_s \ll m_p$, so that a larger fraction of the spacecraft mass constitutes the payload mass m_p (i.e., $\frac{m_p}{m_p+m_s} \to 1$), i.e., mass allocated for instruments and other spacecraft systems. For example, $1\ \mu m$ thick $w = 10\ cm$ lightsail would weigh less than 100 mg, $m_s \leq 0.1\ g$ (i.e., <10% of total spacecraft mass m).

To further illustrate this point in the Fig. 2.15 we plot the velocity gain, Δv, after $t = 1000\ s$ of illumination as a function of incident laser power and m_p/m_s ratio for a total spacecraft mass of $m_s + m_p = 1g$ (here again an idealistic scenario, Eq. 2.2, is assumed). For $m_s < 0.1 m_p$ contribution of the lightsail mass to achieving a desired Δv strongly diminishes. Small fraction of the lightsail mass provides flexibility in selecting lightsail materials and photonic design.

Evidently, a proper figure of merit for light sail design obtained from Eq. 2.2 is then:

$$
\begin{cases}
\Delta v = \dfrac{2}{c} Pt \max\left(\dfrac{R(m_s)}{m_s + m_p}\right), \\
\quad T < T_c
\end{cases}
$$

(2.17)

where $T < T_c$ condition ensures that the sail temperature, T, is kept below a desired threshold, T_c. In the limit of $m_s \ll m_p$ these conditions may be considered independently, implying that the figure of merit simplifies to searching structures that yield simultaneously high reflectivity $R(m_s) \to 1$ to maximize radiation pressure and high emissivity for radiative cooling to desired operation temperature $T < T_c$, while keeping $m_s \ll m_p$. In the

following analysis we discuss materials selection and photonic designs that can meet these conditions, namely high reflectivity and low operating temperature in an ultrathin film limit.
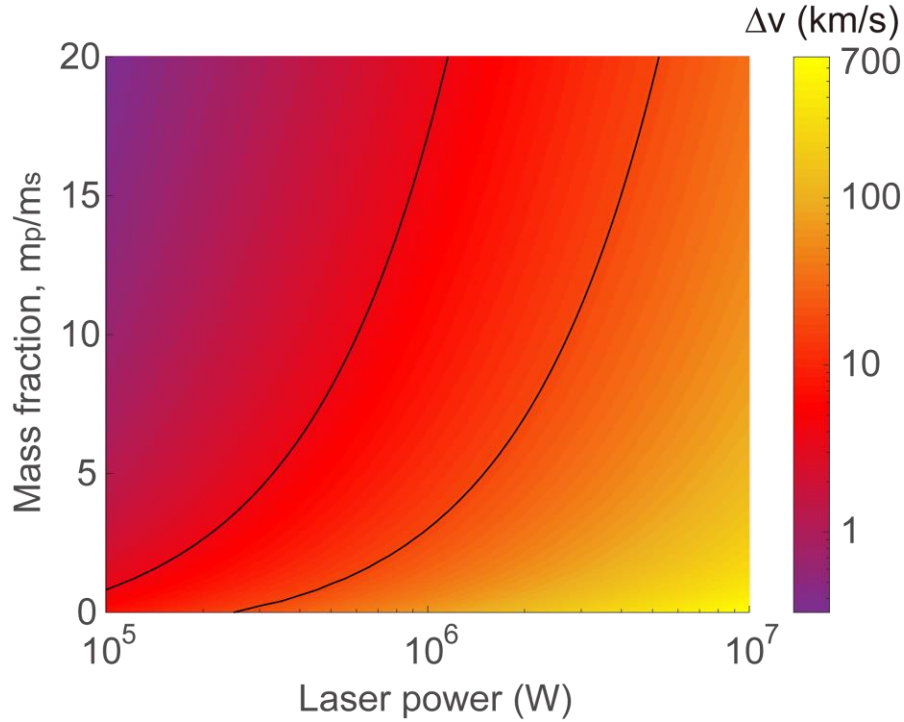
Figure 2.15 Velocity gain, Δv, with laser power and payload to sail mass ratio. 1000 s of total illumination time is assumed. The curves indicate velocity gain needed to perform LEO to GEO transfer and 90 deg. orbital plane inclination change (see also Fig. 2.9).

In order to identify materials and photonic designs that can meet our metrics, we first study the effects of laser absorption on sail temperature to determine the range of admissible laser absorptivities and thermal emissivities that ensure keeping the lightsail at a low operation temperature. At the equilibrium, sail temperature is found as a power balance between absorbed laser power $P_{abs} = \alpha P$ and power emitted as thermal radiation into the free space $P_{rad} = 2\sigma\epsilon T^4 \pi w^2$:

$$T = \left(\frac{\alpha}{2\epsilon} \times \frac{P}{\pi w^2} \times \frac{1}{\sigma} \right)^{\frac{1}{4}}$$

(2.18)

where α is the sail absorptivity at the laser wavelength λ (nonrelativistic dynamics ensures that Doppler shift may be neglected in our case), ϵ is a hemispherical sail emissivity, factor of 2 accounts for front and backside thermal emission (for an ultrathin film sail its front and rear sides within a first order approximation exhibit similar emissivity values [32]), πw^2 is the sail area, and σ is the Stefan–Boltzmann constant. Evidently for a given laser power, P, which is chosen to satisfy desired mission requirements (Fig. 2.5(b)), the sail temperature depends on α/ϵ ratio. In Fig. 2.16 we plot sail temperature variation with the incident laser power, P, and lightsail absorptivity to emissivity ratio, α/ϵ, for a sail with $w = 10 \ cm$ (i.e., wafer scale [36, 62]). Clearly in the range of powers that are of interest here ($P \leq 1 \ MW$) sail temperature may be kept below $T \leq 500 \ K$ for $\frac{\alpha}{\epsilon} < 10^{-3}$, which may be reached with a proper choice of materials. Hence, with the use of low loss dielectrics (e.g., TiO_2, Al_2O_3, MgF_2, BN) or wide bandgap semiconductors (e.g., Si, Si_3N_4, MoS_2, GaAs, C) below their absorption band, absorptivities on the order of 10^{-4} to 10^{-6} may be attained). In addition, nanophotonic engineering may allow design of thin thermally emissive surfaces with a relatively high emissivity ($\epsilon > 0.1$) [63-68].
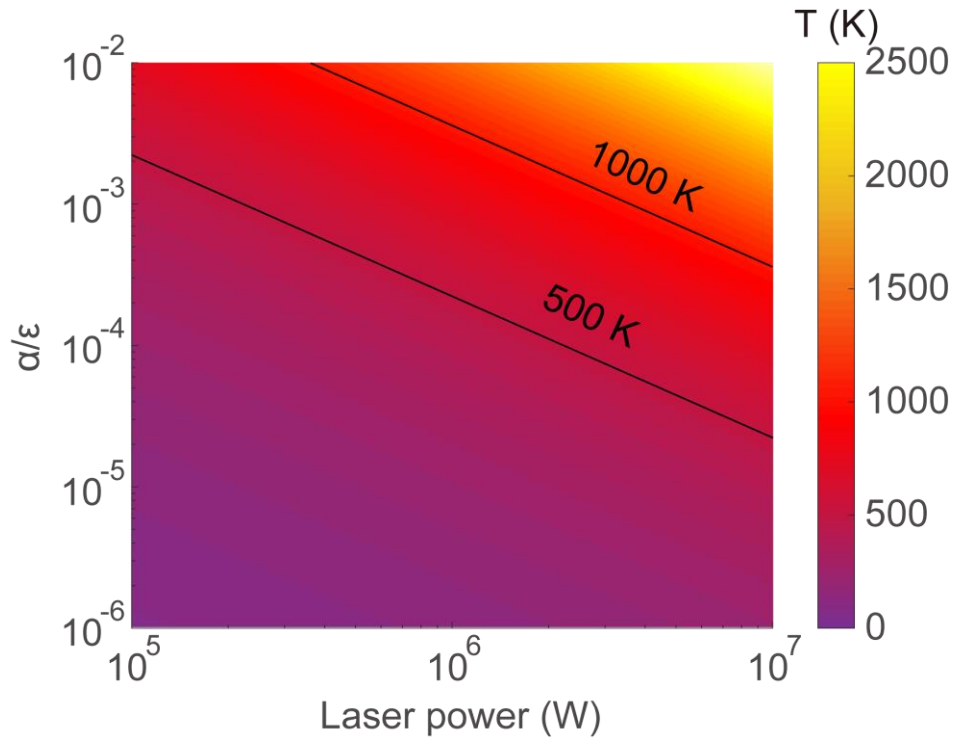
Figure 2.16 Lightsail temperature as a function of the laser power and α/ϵ ratio.

Together with α/ϵ ratio lightsail temperature depends on its area πw^2: larger area yields higher radiated thermal power and thus lower lightsail temperature for a given incident laser power P. Figure 2.17 plots minimum lightsail radius, w, needed to keep its temperature below $T = 500\,K$ as a function of the incident laser power, P, for different α/ϵ ratios. In all of the studied cases the area of a sail needed to radiatively cool it to moderate temperatures is rather small, i.e., $w \propto 10\,cm$. This suggests that small, wafer scale, spacecraft can be launched and propelled by laser beams to perform desired breakthrough fast transit missions.
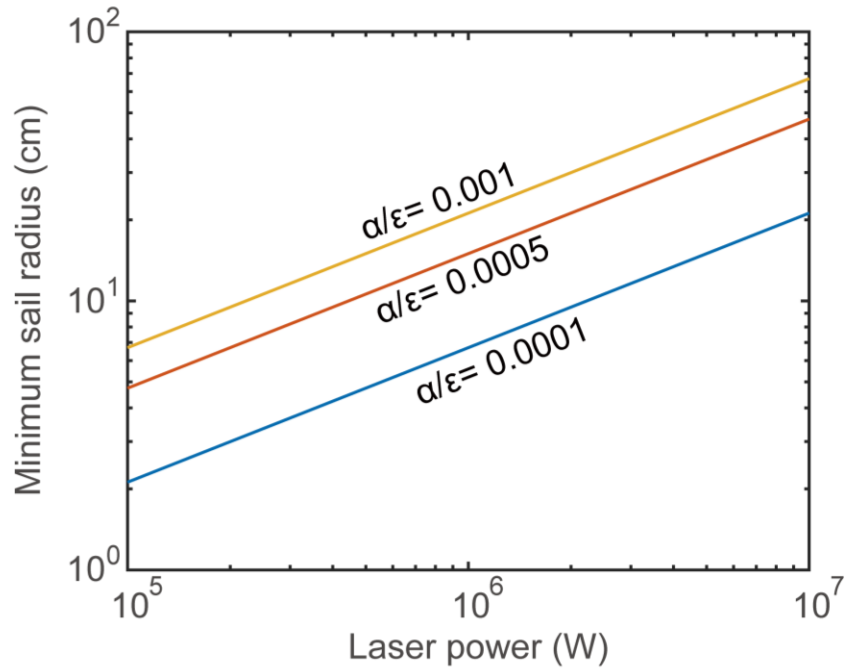
Figure 2.17 Minimum sail area needed to keep the sail at 500 K with laser power

variation for different α/ϵ ratios.

The analysis in this section demonstrates that a relatively small mass budget for the sail, in comparison to the payload, eases design constraints. This allows for the consideration of radiative cooling and the maximization of reflection for optimal momentum transfer independently. In addition, sail designs that are made of low loss (at the laser frequency) materials and high thermal emissivity are needed to withstand the laser power. Photonic design considerations are examined in the next section.

2.6 LightSail materials and nanophotonic designs

After determining the range of α/ϵ needed for a successful operation under high laser powers, we proceed to identify materials and photonic designs that can provide $R \simeq 1$, while offering low α/ϵ ratio and a small lightsail mass. We assume laser wavelength of $\lambda = 1.06\,\mu m$, which is dictated by the atmospheric transparency [67] and availability of low cost high power fiber lasers [69]. Transparent dielectrics, such as SiO$_2$, are ultra-low loss at the laser wavelength, however, their low refractive index ($n \leq 1.5$) leads to thicker and heavier structures. High refractive index materials ($n \simeq 3.5$), such as Si or GaAs, on the contrary, allow design of a diverse range of ultrathin functional photonic structures [70], nevertheless higher loss at the laser wavelength and weak absorbance in the infrared lead to higher operation temperatures. As optimal materials for lightsail design we consider silicon nitride and boron nitride, which although possessing lower refractive index when compared to Si, ($n\sim2$ vs $n \simeq 3.5$), are well suited for our needs. Specifically, crystalline stoichiometric silicon nitride (Si$_3$N$_4$) [71-73] and hexagonal boron nitride (hBN) [74, 75] possess ultralow loss at 1060nm (absorption coefficient ~ 11 m^{-1}). In addition these materials and their allotropies exhibit high infrared absorptivity [72, 76], which offers an efficient pathway for lightsail radiative cooling [63].

Figure 2.18 shows extinction coefficient, k, for SiN and BN respectively, [77, 78]. SiN clearly exhibits a broadband absorptivity in long wavelength infrared range. Absorptivity of BN, in contrast, is narrowband and peaks around 7µm.
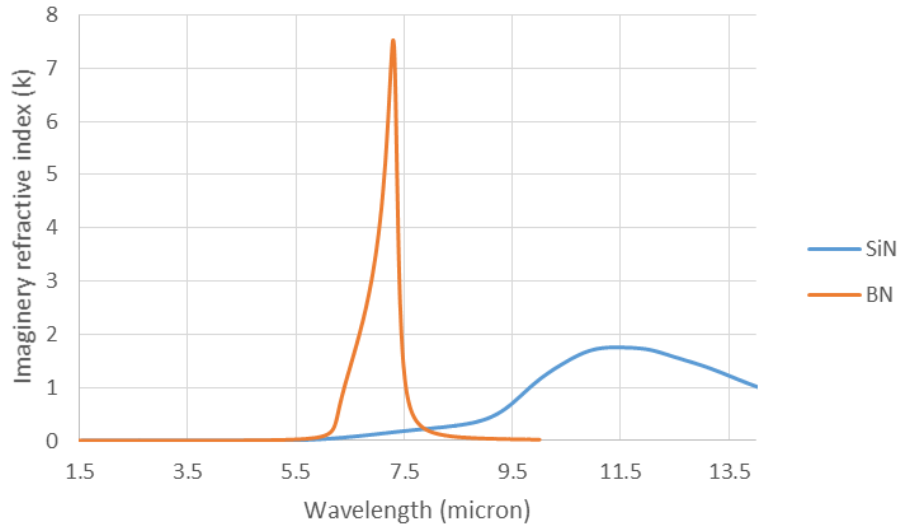
Figure 2.18 Optical extinction for SiN and BN. Optical constants are taken from [72] and

[76], respectively.

As mentioned in the previous section, in contrast to Starshot LightSail, which is constrained by a very stringent mass budget [23], design constrains in the context of the present discussion are significantly relaxed, as soon as $m_s \ll m$ criterion is satisfied. In this case lightsail reflectivity and its thermal emissivity can be optimized independently, as is conceptually illustrated in Fig. 2.19. In subsequent discussion we consider first design of a perfect reflector at the laser wavelength and then we study photonic designs that maximize the emissivity.
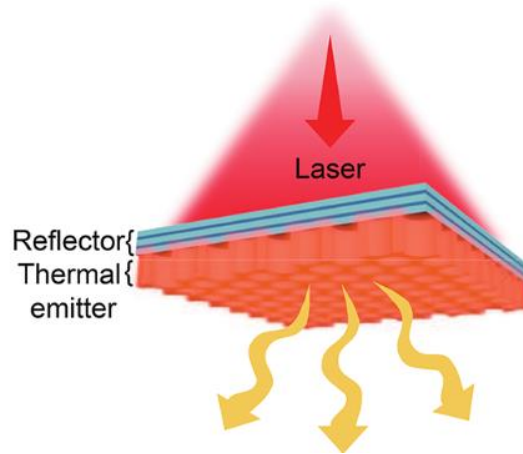
Figure 2.19 Conceptual illustration of the lightsail depicting an reflector layer that faces the incident laser beam and the thermal emitter layer that dissipates the heat radiatively.

2.6.i Ultralight reflectors for lightsail designs

To achieve high reflectivity at the laser wavelength we employ principles of nanophotonic design to design thin film and lightweight structures. As a motif for the photonic design of high reflectivity light sail we consider a Bragg grating and guided mode resonance (GMR) reflectors.
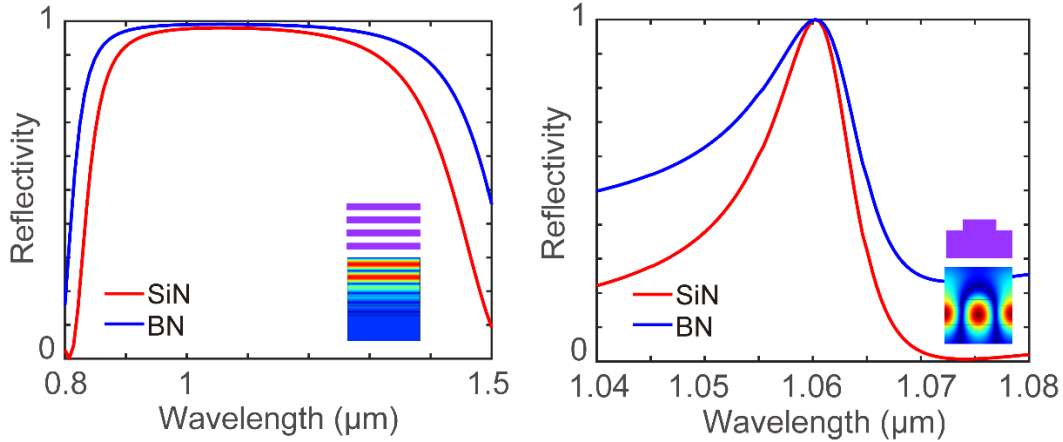
Figure 2.20 Reflection spectra for Si_3N_4 and hBN Bragg reflector (left) and guided mode resonance reflector (right) designs. Insets show respective geometries and calculated electric field intensity profiles at $\lambda = 1.06\mu m$

Figures 2.20 show two examples of lightsail reflector designs: Bragg stack and guided mode resonance (GMR) reflectors [79], respectively. With the use of full-wave FDTD simulations we optimize both structures to obtain a near unity reflectivity ($R \simeq 1$) at the target wavelength ($\lambda = 1.06\ \mu m$). Bragg reflector designs (Fig. 2.20 (left)) have a total thickness $\sim 1.3\ \mu m$ (silicon nitride reflector is comprised of 133 nm thick Si_3N_4 layer with 265 nm thick spacers between them; boron nitride design is made of 120 nm thick hBN layers with 265 nm thick spacer layers). Already 4-layer Bragg structures exhibit broad reflection band across $0.9\ \mu m - 1.3\ \mu m$ with near unity reflectance ($R > 0.98$) at the laser wavelength ($\lambda = 1.06\ \mu m$). GMR structures (Fig. 2.20 (right)), in turn, enable much thinner, and hence lighter, reflector structures. Specifically, optimal structures with near unity reflectance ($R > 0.99$) at $1.06\ \mu m$ have thickness of about 250 nm. Nonetheless, being resonant in nature [79] GMR designs exhibit much narrower reflectance bandwidth.

Low intrinsic optical absorption in Si_3N_4 and hBN at the laser wavelength, results in low laser light absorbance. Hence, nonresonant Bragg reflector structures exhibit $\alpha \simeq$

10^{-6}, whereas resonant light-structure interaction in GMR reflectors results in a 100 fold enhanced laser absorption, i.e., $\alpha \simeq 10^{-4}$. We note that many other structures may be used to achieve near-unity reflectivity as well, including metasurfaces [80], photonic crystal membranes [81], and more sophisticated designs obtained by advanced optimization techniques [82]. Our analysis may be generalized to these structures as well.

These designs assume that the spacer is a vacuum with refractive index $n = 1$. In practice, architectures with ultralow mass density and near unity refractive index should be used. We foresee three possible strategies for creating such structures. The first is with the use of aerogels, which are made of low loss and high temperature silica. Previously aerogel films as thin as 100~200 nm have been demonstrated [83]. Mechanical metamaterials made of nanostructured architectures is another approach. For example, stiff hollow sandwich plates made of few nanometer thick alumina have been shown recently [84] Such plates may serve as "sandwich" panels between functional material layers. Finally, the SiN material itself is known to have good mechanical properties, as it is one of the most common materials for MEMS devices[85-87]. Micro pillars can be designed to sustain hollow spaces across photonic structure.

In our study we assume normal incidence (i.e., $\theta = 0$) and optimize our structures accordingly. However, in practice reflectivity of the designed structures may depend on the incidence angle (i.e., $R = R(\theta)$). Figure 2.21 shows reflectivity as a function of the incidence angle for Bragg stack and GMR designs made of Si3N4 at the laser wavelength (1060 nm), respectively. Broad reflection band of the Bragg reflector (Fig. 2.20) results in angle insensitive designs: almost no variation is seen for 0-15 degs. On the contrary narrow, resonant, bandwidth of the GMR reflectors results in highly sensitive structures. Such

angular dependence may result in a smaller velocity gain and related drop of performance.

As such, in practice mission requirements (i.e., mutual laser – sail orientation and orbital

dynamics) may need to be taken into account. In this case, structures with a desired angular

dependence should be designed. In these cases, angular dependence constitutes another

additional trade parameter (as more angle insensitive designs would need more sail mass).
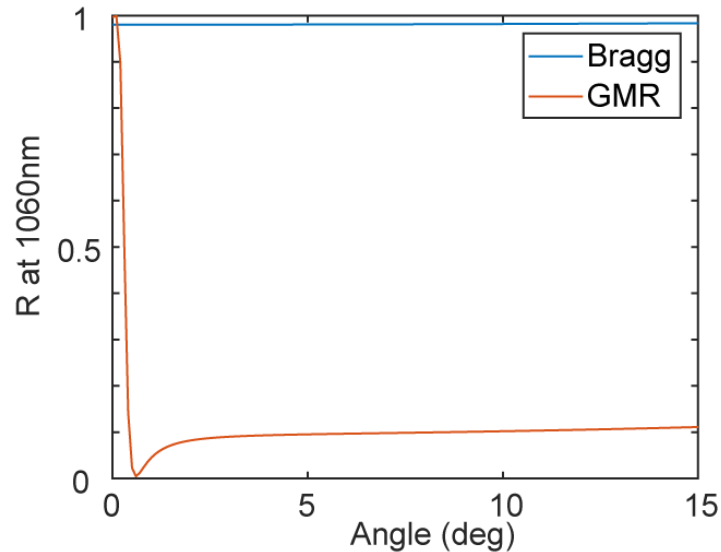
Figure 2.21 Angular dependence of reflectivity at laser wavelength for Bragg and GMR

reflectors.

Finally, we note that in our numerical calculations we assume 2D structures and TE

polarized waves. The density of the structures is estimated by extrapolating 2D designs to

a 3D structure, which provides a more accurate density estimate. Such an approach

significantly simplifies optimization (as compared to a full wave 3D optimization) and

yields good preliminary designs, which allows us to assess capabilities of laser sailing and

related figures of merit. We note that such 2D designs can be extrapolated to 3D structures

(verified numerically for a few studies cases). However, a dedicated 3D optimization may

be needed for structures where full polarization and angle of incidence control is necessary.

2.6.ii Thin film thermal emitters for lightsail

Next we study designs that yield high thermal emissivity. The mechanism of light absorption in silicon nitride and boron nitride is drastically different. Stoichiometric silicon nitride, i.e., Si_3N_4, is ultralow loss up-to $\simeq 8.3\ \mu m$ and is not suitable for design of efficient thermal emitters [72, 73]. At the same time Si rich silicon nitride, i.e., SiN_x, exhibits strong absorbance starting from $\sim 5\mu m$, which makes it well suited for radiative cooling across mid-infrared band [72]. Yet, a careful account of laser absorbance in non-stoichiometric SiN_x should be taken. In our case the thermal emitter layer is nearly completely shielded by the near-unity reflector (Fig. 2.19), and hence laser absorbance in the thermal emitter can be neglected. Boron nitride, in turn, exhibits strong polaritonic resonance at $\sim 7.3\ \mu m$ (and at $\simeq 13\mu m$), which is associated with formation of a Reststrahlen band with negative material permittivity in a range $6\mu m - 7\mu m$ [74, 75]. Phonon-polariton resonances in hexagonal boron nitride exhibit very high quality factors, which makes coupling of thermal radiation with a crystalline hBN challenging. Broader resonances are observed in boron nitride nanotubes (BNNT), which makes them better suited for thermal emission management [76]. In Fig. 2.22 we plot spectral emissivity ϵ_λ for thin BNNT (500 nm thick) and Si-rich SiNx (1 μm thick) films, respectively. The emissivity can be further enhanced by making use of micro and nanostructured surfaces. Specifically, by perforating the SiNx film (0.265 fill factor) we are able to achieve significant enhancement of emissivity (Fig. 2.22) in a broad spectral range, $\lambda > 6\ \mu m$. For BNNT films emissivity enhancement can be attained by resonant excitation of surface phonon-polaritons [74, 75]. In Fig. 2.22 we plot spectral emissivity of tapered surface phonon-polariton microresonators, which exhibit broad band absorbance across entire Reststrahlen band. Strong and broadband spectral

emissivity of both SiN$_x$ and BNNT films implies that these films may be kept at a reasonably low operating temperature even under high power laser irradiation.
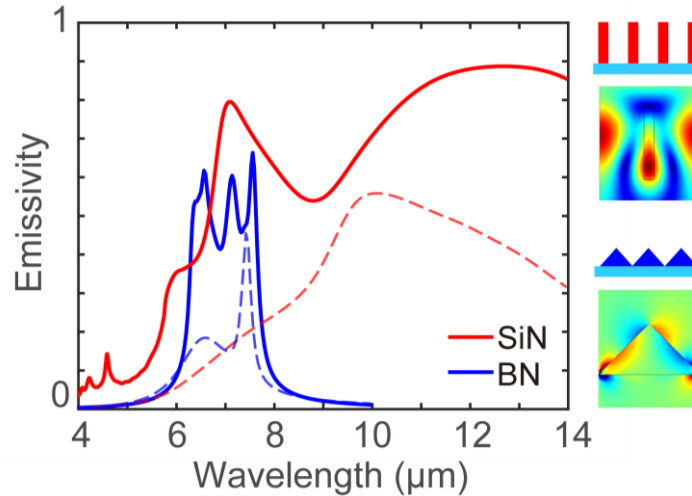
Figure 2.22 Calculated spectral infrared emissivity spectra for SiN$_x$ and BN thermal emitter designs. Dashed curves denote spectral emissivity of unstructured 500 nm thick BN and 1 μm thick SiN$_x$ films, respectively. Insets show schematic of the structure and electric field intensity profiles within one unit cell plotted at 7.7 μm and 6.6 μm for SiN$_x$ (top) and BN (bottom) emitters, respectively.

2.6.iii Overall lightsail design

A final lightsail design is made of a combination of reflector (e.g., GMR or Bragg) and an emitter layers, respectively. Figure 2.22 provides a brief visual summary of the reflector and emitter structures we have designed.
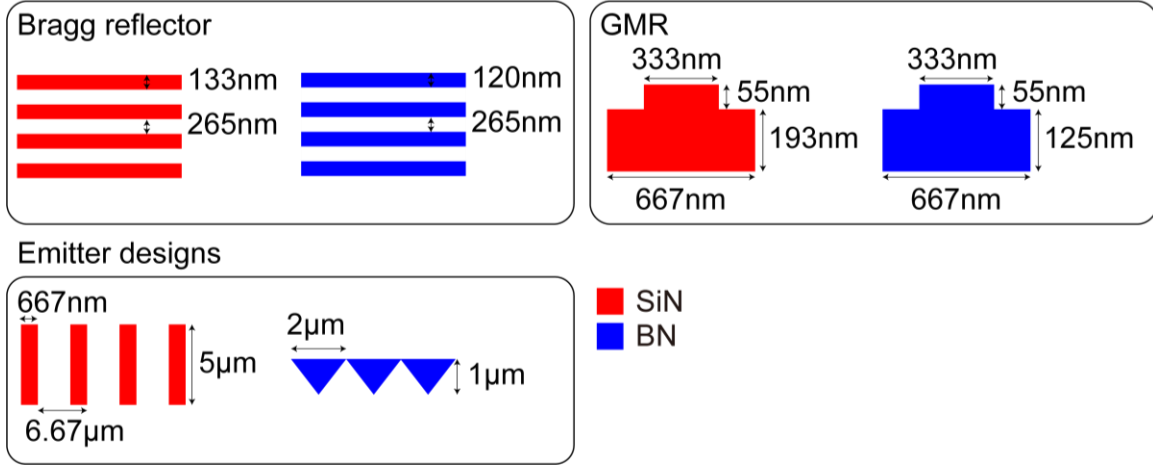
Figure 2.23 Dimensions of optimal reflector designs and thermal emitter designs. Red color indicates Si_3N_4 or SiNx material, and blue color indicates hBN or BNNT material.

Permutation of possible reflector and emitter designs therefore yields total of 8 possible overall lightsail designs, assuming that different material permutations are also permitted. Moving forward, for each of these 8 lightsail designs we study areal density, ρ, and absorptivity to emissivty ratio, α/ϵ. We note that both of these parameters directly translate to the overall figure of merit (Eq. 2.18). To be more specific we assume $P = 1\ MW$ of laser power, $w = 10\ cm$ lightsail radius, $m_p = 1\ g$ payload, and $t = 1000\ s$ illumination time, and calculate lightsail temperature, T, and spacecraft velocity gain, $\triangle v$. The temperature of the sail is found from the radiation balance $P_{rad}(T) = \alpha P_{laser}$, where

$P_{rad} = 2\pi w^2 \pi \int_0^\infty \epsilon_\lambda(\lambda) I_{BB}(T,\lambda) d\lambda, \quad I_{BB}(T,\lambda) = \frac{2hc^2}{\lambda^5} \frac{1}{e^{hc/\lambda k_B T}-1}$ is the blackbody radiation at temperature T, k_B is the Boltzmann constant, h is the Planck constant, and c is the speed of light, factor π approximates hemispherical emission and factor 2 accounts for a double sided emission. The emissivity ϵ at temperature T is founds as:

$$\epsilon = \frac{\int_0^\infty \epsilon_\lambda(\lambda) I_{BB}(T, \lambda) d\lambda}{\int_0^\infty I_{BB}(T, \lambda) d\lambda}$$

(2.19)

Here we assume that due to structure transparency and its thin thickness front and back side emissivities have similar spectra. This assumption was verified with full-wave simulations for several characteristic designs.

Figure 2.24 depicts all 8 point designs studied here on a figure of merit plot, i.e. on $(\triangle v, T)$ $(\rho - \alpha/\epsilon)$ plot. GMR reflectors exhibit 2 orders of magnitude higher laser absorptivity, α, than Bragg reflectors, which results in a higher lightsail temperature. Thus, lightsails with GMR reflectors demonstrate higher operating temperature (500K - 750K) as compared to Bragg reflector designs ($T < 300K$). At the same time, lightsails with GMR reflectors are lighter (as GMR reflectors are ~4x thinner than respective Bragg reflectors), which, in turn, results in a higher Δv. Broadband spectral emissivity of silicon nitride (Fig. 2.22) results in a better heat rejection (i.e., lower temperature) as compared narrow band BN thermal emitters. However, boron nitride being lighter than silicon nitride allows design of very light-weight lightsails, which eventually translates onto higher velocity gain, Δv.
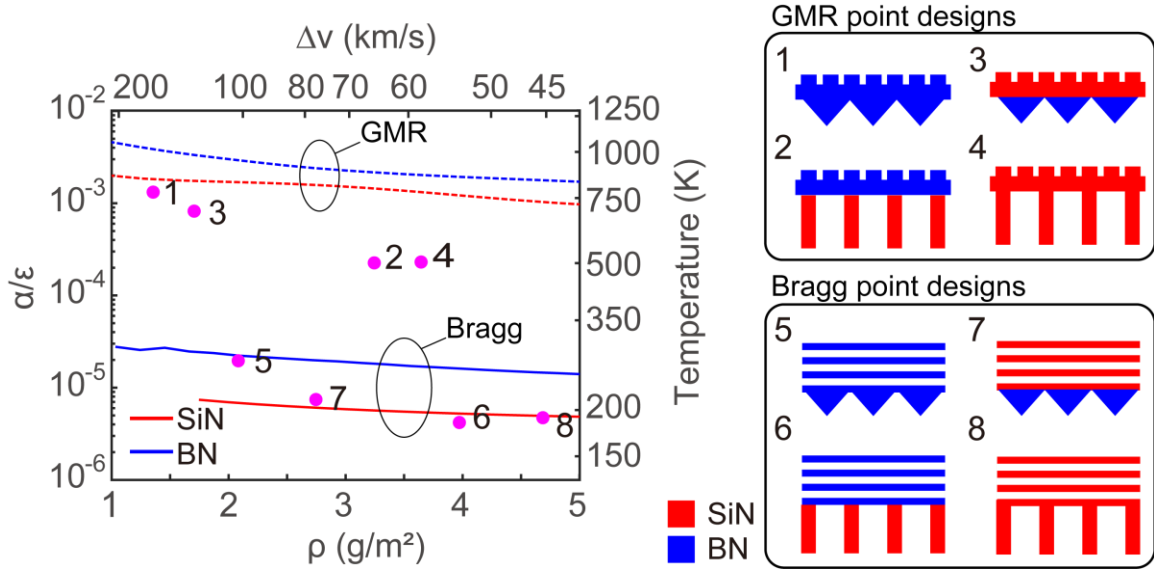
Figure 2.24 Calculated figures of merit for 8 lightsail designs obtained by different permutations of materials and reflector – emitter designs. Insets show schematically respective structures.

2.6.iv Other considerations

The effects of both solar irradiance and Earth thermal emission also play role in power balance and sail equilibrium temperature of the sail. Overall the power balance with the account of solar absorption and Earth thermal radiation emission will be modified to:

$$P_{rad}(T) = \alpha P_{laser} + \pi w^2 \cos(\theta_{sun}) \int_0^\infty \epsilon_\lambda(\lambda) I_{sun}(\lambda) d\lambda$$

$$+ \pi w^2 \cos(\theta_{Earth}) \int_0^\infty \epsilon_\lambda(\lambda) I_{Earth}(\lambda) d\lambda$$

$$(2.20)$$

where θ_{sun} is an angle between sunline and the sail, θ_{Earth} is an angle between a direction to Earth and sail (for low orbits an integral over all possible directions needs to be taken),

$I_{sun}(\lambda)$ and $I_{Earth}(\lambda)$ are spectral power densities of solar and Earth thermal radiation spectra.

The solar irradiance power received by the sail is $P = AI_{sun}$, where I_{sun} solar irradiance ($I_{sun} \simeq 1360 \ W/m^2$ at Earth) and A is the sail area. For a sail with 10 cm radius the solar power incident on the sail is ~40W. This power level is several orders of magnitude smaller than the laser power (>100kW). Moreover, in our case we study wide band gap materials, such as SiN_x and BN which are low loss across the solar spectrum. We estimate that solar radiation absorption will contribute <1W to the power balance – a value that is negligible from the point view of power balances considered here. At the same time in the context of Starshot program, which suggests use of lightsail designs made of lower bandgap materials (e.g., Si and MoS_2), solar radiation may play a more significant role. For example, a 10 m^2 sail with 10% solar absorptivity would absorb ~1kW of incident solar power.

Earth thermal emission, on the other hand may result in a stronger contribution to the power balance, as the sail emission band and Earth thermal radiation bands might overlap, particularly for lower sail temperatures. To illustrate the contribution of Earth thermal radiation we consider sails with SiN reflectors and thermal emitters as an example, specifically designs 4 and 8 in Fig. 2.24. In Fig. 2.25 we plot estimated equilibrium sail temperature with and without the contribution from Earth thermal radiation for the cases of GMR and Bragg reflectors (the choice of a reflector design impacts laser absorbance and its contribution to thermal radiation balance). Here, to get an estimate we assume that the SiN emission layer absorbs all of Earth thermal radiation incident on it (in practice the absorbed power may be smaller due to oblique sail orientation). Since the heat flux on sail

from Earth thermal emission depends on the orbit altitude, the sail is set to be on a 300 km altitude low Earth orbit, where the effect of Earth thermal emission are noticable. The analysis shows that for lower loss Bragg reflector designs Earth thermal emission is manifested more strongly as compared to more lossy GMR sail designs. Indeed, for a very small laser power absorption, as is the case for Bragg reflectors, contribution from Earth thermal radiation dominates the thermal radiation balance and results in sail heating to ~300K equilibrium. For stronger laser power absorptions, e.g., due to higher loss as in the case of GMR or for higher incident laser powers, the role of Earth thermal radiation is diminished.
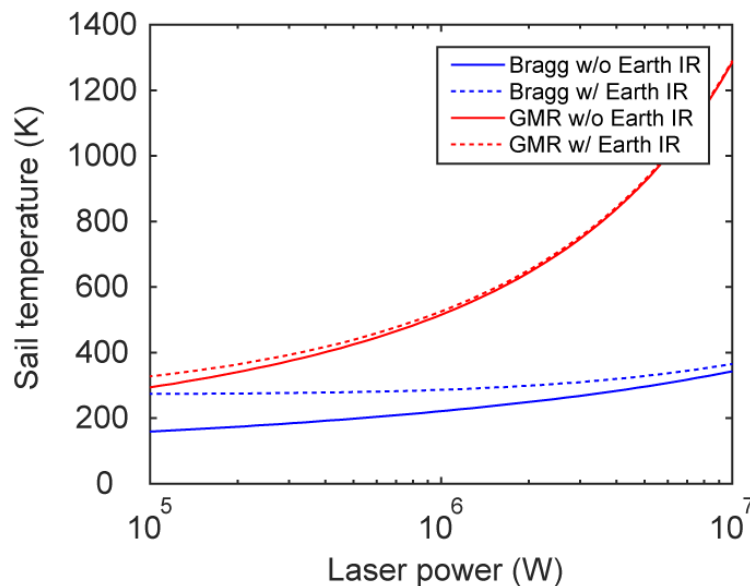
Figure 2.25 Estimated equilibrium temperature of the lightsail with (dotted line) and without (solid line) Earth thermal radiation emission contribution to power balance. The influence of Earth thermal emission on sail equilibrium temperature is diminished as the laser power increased.

Overall we conclude that for high bandgap materials contributions of solar and Earth thermal radiation are insignificant factors in the design of a lightsail. For other materials or

54

regimes of operation a more careful account of both effects needs to be taken into consideration.

2.7 Chapter conclusions

In summary, we have explored a conceptually different operational regime for laser-driven light sailing. We demonstrated that even within a moderate parameter range, laser-driven light sailing has the potential to surpass conventional propulsion methods, presenting new opportunities for Earth orbital maneuvering and space exploration. We introduced a figure of merit – Δv, and discussed materials and design strategies that maximize the figure of merit. We anticipate that laser-driven light sailing could herald a new era of space missions, facilitating fast-transit space exploration. lightsail

CHAPTER 3

Solar Sailing for Breakthrough Space Exploration

In this chapter we discuss solar sailing which uses sunlight for radiation pressure propulsion [88-90]. While propulsion physics is similar to that of laser sailing, need to operate under incident sunlight sets different requirements on sail materials and spacecraft design. Below we first provide a brief overview of solar sailing and then discuss key figures of merit for future breakthrough solar sail missions.

3.1 Solar sailing background

Solar sailing is an emerging in-space "propellant-less" propulsion technology that is receiving a lot of interest across the aerospace community. Solar sails are traditionally viewed as a slow and cumbersome alternative to electric rockets, having a relatively narrow niche for science missions. Hardly anyone can imagine a major solar sail mission to Europa or Titan. Nevertheless, solar sails, owing to a fundamentally different propulsion physics, which is based on light radiation pressure, have the ability to reach unprecedented velocities and orbits [3, 91, 92] that are inaccessible by electric or chemical rockets. In particular, solar sails have potential to perform very high delta-V maneuvers and enable a range of non-Keplerian orbits [93, 94]. This capability is of great interest for novel space missions that are beyond the reach of conventional spacecraft. Specifically, such missions as solar polar imaging, fast transit interplanetary missions, interstellar probe and artificial Lagrange points have been envisioned recently [95, 96].

The last decade has seen several successful technology demonstration missions, including IKAROS [97], Nanosail-D [98] and Lightsail 2 [99]. Figure 3.1 provides a brief overview of these solar sail missions. The most notable of these is IKAROS, which was the first solar sail mission and the first interplanetary mission of its kind designed and operated by JAXA. Launched in 2010, a 310 kg spacecraft featuring a 196 m^2 sail flew by Venus in December of 2010. IKAROS showed that radiation pressure propulsion is feasible and can be utilized for navigation in space. Furthermore, IKAROS allowed testing a number of emerging technologies, including embedded photovoltaic panels and liquid crystal reflectivity control devices for attitude control [100, 101].
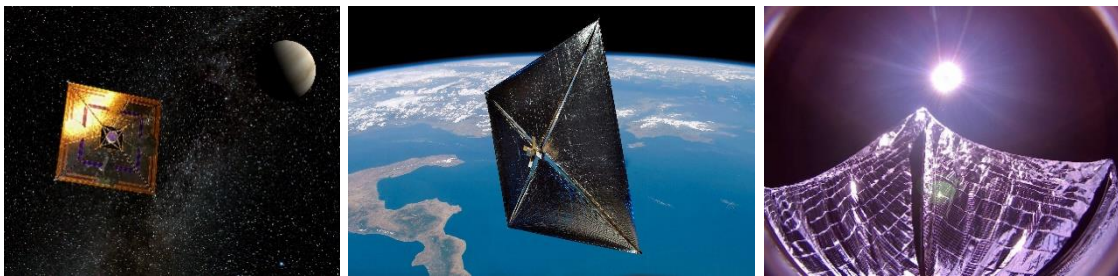
Figure 3.1 (Left) Artistic depiction of IKAROS - the first sucessful solar sail interplanetary misison [18]. (Middle) Artististic depiction of Nanosail-D2. Image from NASA. (Right) Photographic image of deployed LightSail-2 [99].

Subsequent solar sail missions - Nanosail-D2 by NASA (2011) and LightSail-2 (2015) by Planetary Society – further verified sail deployment and tested ability for maneuvering at Earth orbit. Notably, both Nanosail-D2 and LighSail 2 were built as small 3U CubeSat spacecraft.

One of the key metric for solar sail propulsion in space is sail area to the overall spacecraft mass ratio, A/m. The larger is the sail area the larger is the radiation pressure

and related thrust. On the other hand, smaller mass translates to a higher acceleration for a given thrust. Therefore, it is highly desirable to build spacecraft with large A/m ratios. The area-to-mass ratio of recent solar sail missions ranges from 2 to 10 m^2/kg (with IKAROS being the heaviest one).
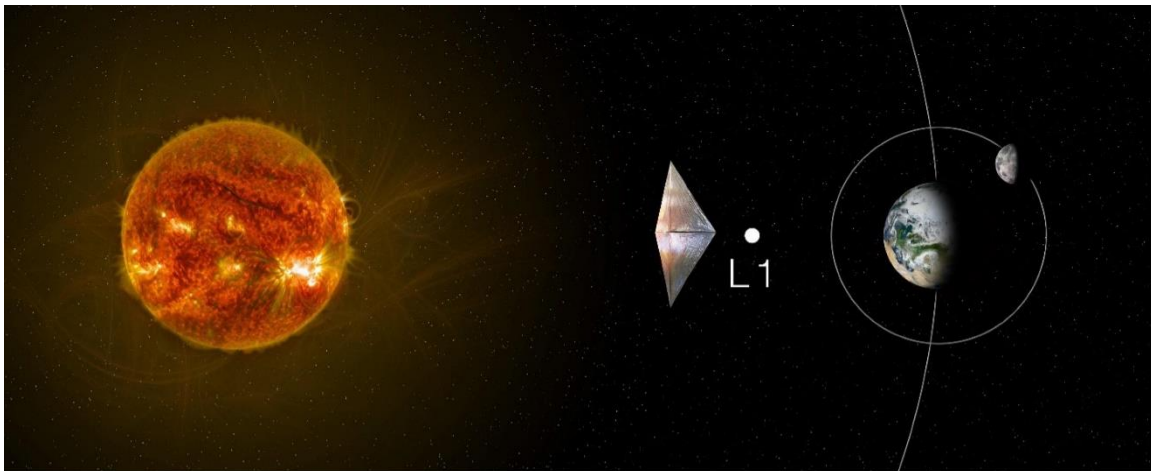
Figure 3.2 Schematic illustration of the Solar Cruiser mission, which aims to place a spacecraft at an artificial Lagrange L1 point closer to the sun for early space weather warning. Image credit: NASA.

While early tests have proved to be successful, next generation of solar sail missions would necessitate larger sail areas and larger area-to-mass ratios. A notable example is a Solar Cruiser mission [40, 41], Fig. 3.2. Solar Cruiser is a planned interplanetary solar sail mission that sets an ambitious goal of launching the largest sailcraft to date, 1653 m^2 area and ~90 kg mass. The area-to-mass ratio in this case is ~18.5 m^2/kg. Owing to its higher area-to-mass ratio Solar Cruiser will be the first spacecraft to demonstrate effective off-shift of Lagrange L1 point [96], which is of great importance for early space weather warning. Figure 3.3 summarizes size and area-to-mass ratios of solar sail missions flown and planned [58]. A trend for larger area-to-mass ratio is evident. Future developments therefore call for lighter sail materials and more efficient spacecraft

designs. Part of the work described in this thesis is related to studying ultrathin film solar sail materials.
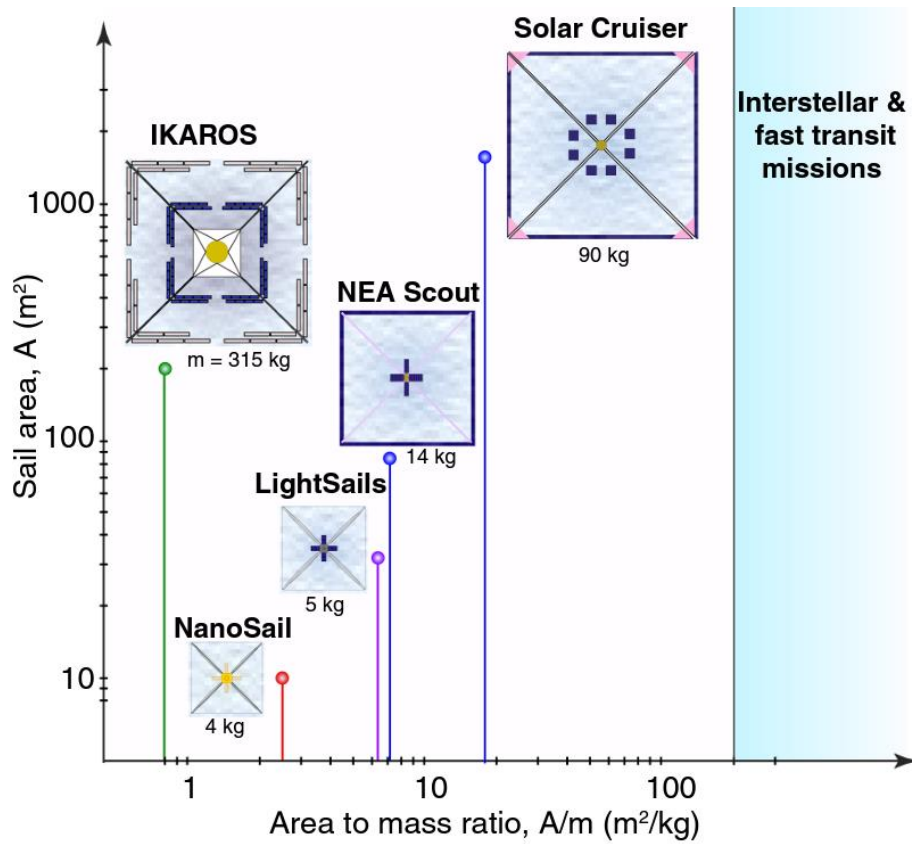
Figure 3.3 Schematic illustration of solar sail missions flown and planned, after Ref. [58].

In addition to building lighter spacecraft (i.e., with higher A/m ratio), future interplanetary and heliophysics missions would benefit from getting closer to the sun. Examples of such missions include solar polar orbiter and fast transit interplanetary exploration missions (see Fig. 3.4). Solar polar imaging mission is a long envisioned mission of sending a solar sail spacecraft onto a polar orbit about the sun [102, 103]. Reaching polar orbits requires very high delta-V maneuvers, which are by far beyond the reach of conventional spacecraft. As an example, recently launched Solar Parker Probe, while reaching as close as 9 R☼ from the surface of the sun, gets only to a modest 3°

inclination to the plane of ecliptic [104]. Furthermore, by getting close to the sun, solar sails can harness higher solar radiation flux in combination with larger gravity to perform more efficient maneuvering. If available, solar sails with close solar approaches would allow faster climb to the polar regions and faster missions to outer planets and interstellar medium [101].
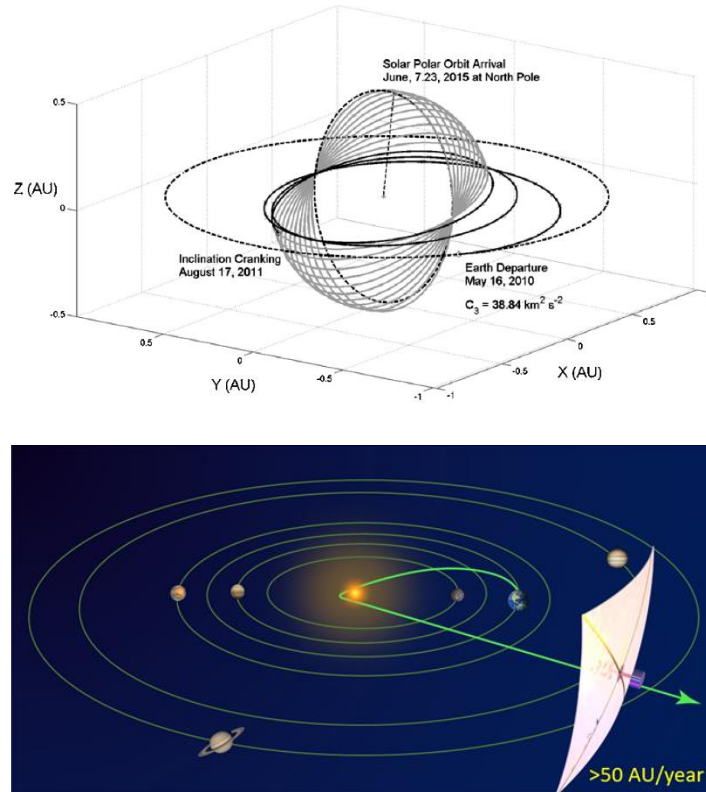
Figure 3.4 (Top) Solar polar orbiter mission concept [105]. (Bottom) Concept of a fast transit interplanetary probe mission.

3.2 Extreme solar sailing

In the context of fast transit outer space exploration of great interest is so-called "extreme solar sailing", in which solar sails benefit greatly from maneuvering in the vicinity of the sun. By making a close perihelion slingshot maneuver (as shown in Fig. 3.5(a)), velocities in excess of 60 AU/year (>300 km/s) are conceptually possible for ultralight-weight systems (A/m $\geq$ 300 m^2/kg) and perihelion distances $<$ 5 R$_\odot$ (Parker Solar probe's nearest approach is ~9 R$_\odot$ [106]). Velocities that potentially can be accessed by solar sails exceed those of other proposed propulsion concepts, including solar thermal [28], large chemical rockets utilizing solar and Jovian slingshot maneuvers [29–31], and nuclear electric propulsion [5, 29, 32]. With such high velocities, solar sailing may pave the way to a new era of solar imaging, deep space and interstellar exploration.

Figure 3.5(b) shows calculated heliocentric exit velocity with perihelion distance for different sail area to an overall spacecraft area-to-mass ratio. The exit velocity here is calculated according to Ref. [58]:

$$v_{\text{inf}} \cong \sqrt{-\frac{2\mu_s}{1AU + d_0} + 2(2R_s + \alpha)\frac{S_{1AU}}{c}\frac{(1AU)^2}{d_0}\frac{A}{m}}.$$

(3.1)

where μ_s is the solar gravitational parameter, c being the speed of light, m is the mass of the sailcraft, d_0 is the perihelion distance, R_s and α are the reflectance and absorbance of the solar sail, and $S_{1AU} \simeq 1360 \ W/mm^2$ is AM0 solar flux at Earth. Evidently, solar sail velocity depends on its optical properties (i.e., solar reflectivity and absorptivity), sail area to total spacecraft mass ratio, A/m, and the perihelion, d_0. Smaller d_0 and higher A/m ratio yield higher cruise velocities. Clearly, the exit velocity increases significantly when

the perihelion is <10 R☼ and the spacecraft is sufficiently lightweight. With the use of a powered slingshot, a lightsail may be placed on hyperbolic escape trajectories with high excess velocity that can reach tens of AU/year, enabling interstellar missions. In this case, Voyager 1 can be surpassed in 2.5 years, and the solar gravity lens location reached in just 8.5 years [4]. As such, extreme solar sailing is of great promise for fast transit outer space missions.
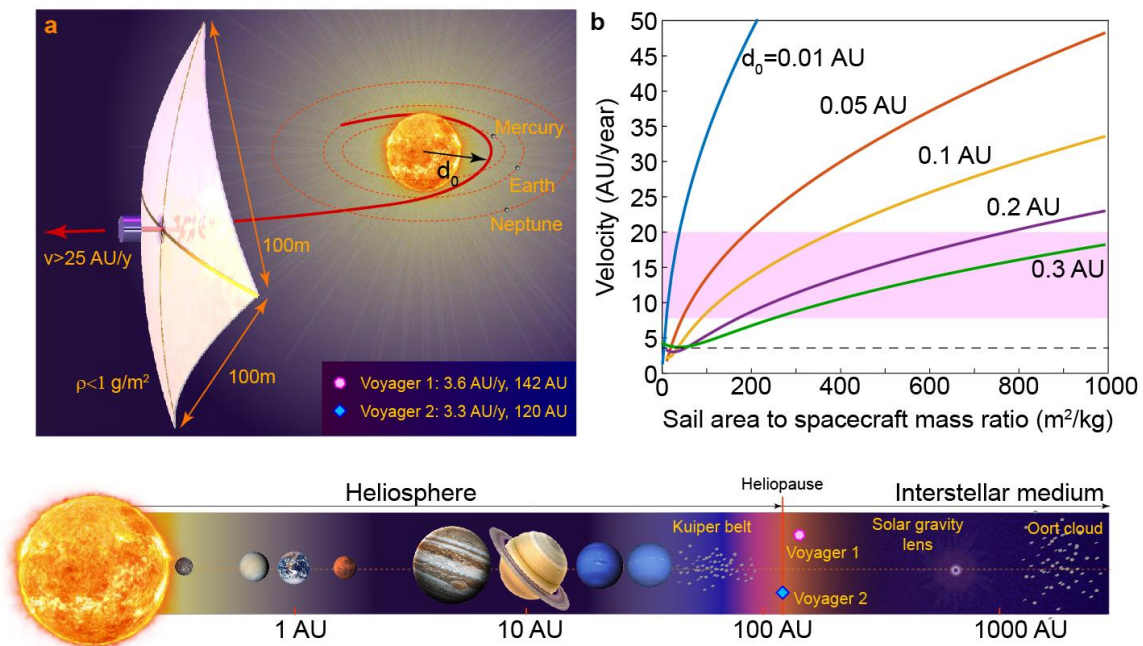
Figure 3.5 Solar sails for interplanetary and interstellar space missions. (a) Schematic of an extreme solar sailing mission. By making use of a powered gravity assist in close proximity to the sun, a sailcraft may be propelled to over 60 AU/year. Example solar sail parameters are shown. Inset shows velocity and current distance from the sun for Voyagers 1 and 2—the only two probes that have left the heliosphere. (b) A calculated sailcraft heliocentric excess velocity (i.e., solar system exit or cruise velocity) with perihelion distance for different sail area to spacecraft mass ratios. Here an ideal, flat perfectly reflecting, sail is assumed. The inset below panels (a) and (b) illustrates the

scales in the solar system, shows the positions of Voyagers 1 and 2 and the heliosphere

boundary. Figures are altered from Ref. [58].

The concept of operations of an extreme solar sailing mission is as follows. Once the sailcraft leaves the Earth's sphere of influence, the sail dynamics is fully governed by the solar gravitation attraction and solar radiation pressure. At first the sail is brought close to the sun by orienting sail at an angle with respect to the sunline (i.e., at an angle with respect to incident radiation); Fig. 3.6 conceptually illustrates this maneuver [58]. In this case radiation pressure will induce a force component that is directed against the velocity vector causing the sail to lose specific energy and gradually fall toward the sun. Conceptually this maneuver is similar to orbit raising or lowering performed by low thrust propulsion systems. Once near perihelion the sail is re-oriented to face the sun and is kept that way (excluding minor potential trajectory corrections). This phase is known as a powered slingshot or Oberth maneuver, where gravitational attraction and the radiation pressure interplay to create a strong propulsive force. The sail stays that way for an active post-perihelion propulsion phase, and is inserted onto a hyperbolic fast-transit trajectory.
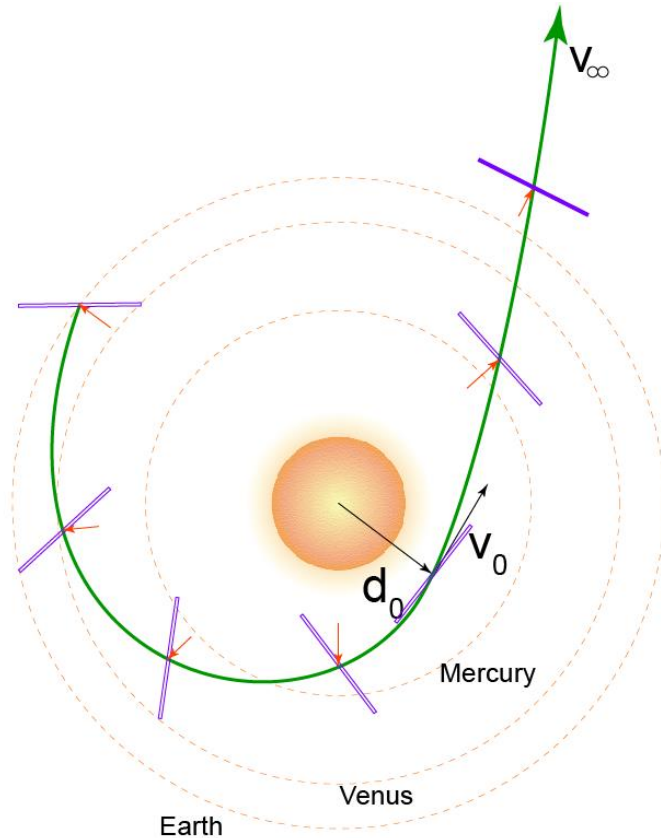
Figure 3.6 Schematic illustration of the sail spiraling in toward the sun and powered

slingshot, after Ref. [58].

While there have been several solar sail flight demonstrations within the last decade,

extreme solar sailing requires new materials and sail designs beyond that of current

technology. Present solar sails are thin aluminized polyamide films: ~100 nm thick

aluminum deposited atop of a ~1-5 μm thick polyamide (e.g., Mylar^{TM} or Kapton^{TM}) [88,

89]. While this technology is well established, and flight proven, such solar sails are not

suitable for missions with close perihelion approaches, implying that conventional solar

sails are not suitable for the high Δv escape missions. Extreme solar sailing requires a new

generation of lightweight sail materials and sail systems, which can get to <10 R☼

perihelion. As we discuss below such systems and missions are possible with a proper

technology development. We further note that the need for high temperature materials was highlighted in several of previous works, where such options as graphene, beryllium, and dielectric sails were discussed [107-109].

3.3 Present day sail materials

As mentioned future solar sails have a potential to enable a range of breakthrough missions. However, a significant research effort is needed to enable lighter spacecraft and reaching closer to the sun. One of the major limitations of present day solar sails is the material of the sail membrane. Present day solar sails are made of aluminized polymer films with ~50-100 nm thick aluminum and a few micron thick polymer (e.g., CP1^{TM}, Mylar^{TM}, or Kapton^{TM}) support layer [99, 110, 111], which possess relatively high areal density and exhibit low degradation temperatures. For instance, Solar Cruiser sail membrane is made of a 2.5 μm thick CP1 coated with a thin layer of aluminum. Glass transition of CP1 is $\simeq 520 K$ and relatively large solar absorptivity of Al (~8-10%) constrain the minimum perihelion to 122 $R_{\odot}$ (0.57 AU) [96, 99, 110-113], precluding Solar Cruiser and similar sails from getting close to the sun. Table 3.1 summarizes typical materials used for the design of solar sail membranes (commercially available) by their areal density and their respective glass transition/melting temperature.

Table 3.1 Summary of currently used sail materials based on commercial vendor datasheets.

Mylar	Vendors 1, 2	Vendor 3
Density	0.7 g/m²	4.3 g/m²
Main thickness	~0.5 µm	3 µm
Glass transition temperature	~250°C (520 K)	

DuPont	
Density	10.8 g/m²
Main thickness	7.5 µm
Glass transition temperature	~360°C (630 K)

CP1	Nexolve	Spin coat
Density	3.85 g/m²	
Main thickness	2.5 µm	≤1 µm
Glass transition temperature	~250°C (520 K)	

Kapton^{TM} films have higher melting temperature ~630 K (with some high grade versions reaching ~750 K). However, Kapton^{TM} films thinner than 7.5μm are hard to fabricate, making Kapton based sails too heavy. Therefore, most of present day sails use CP1 as a support layer, which can be made as thin as 2.5 μm (potentially even thinner; e.g., sub-micron thick Mylar films are commercially available). At the same time, lower glass transition temperature of CP1 and Mylar precludes the use of these materials for close solar approach missions.

To further illustrate the limitations of current sail materials it is instructive to study sail temperature defined by a thermal balance of the heat generated due to sunlight absorption in sail materials, on one hand, (i.e., $P_{in} = P_{sun} = \alpha S$, where $S = S_{1AU}/d_0^2$ and $S_{1AU} \simeq 1360\ W/mm^2$ is AM0 solar flux at Earth) and thermal radiation emission on the other (i.e., $P_{out} = P_{rad} = \sigma T^4$). The equilibrium sail material temperature, T, at perihelion, d_0, is then given as:

$$T \cong \left(\frac{\alpha}{\epsilon} \frac{S_{1AU}}{\sigma} \frac{(1AU)^2}{d_0^2} \right)^{\frac{1}{4}}$$

66

where ϵ is thermal emissivity of the sail material, σ is the Stefan-Boltzmann constant, α is solar absorptivity. In Fig. 3.7 we plot temperature of aluminized sail with perihelion distance for different values of thermal emissivity (assuming that it can be engineered). The front-side (i.e., Al side) emissivity is $\epsilon \simeq 0.04$ (although it slightly increases with the temperature increase), whereas back-side (i.e., polymer side) emissivity is $\epsilon \leq 0.1$. Currently used aluminized CP1 sail can reach at most 122 $R_{\odot}$ (0.57 AU) perihelion. Kapton based sails can get even closer to ~84 $R_{\odot}$ (0.39 AU). That is, current polymer-based sails are not able to get even to an orbit of Mercury. By engineering thermal emissivity of sail materials the sails may be brought closer to the sun. The theoretical limit in this case is given by $\epsilon = 2$, which corresponds to both sides of the sail emitting as an ideal black body (in practice we expect that for such ultrathin films the double sided emissivity will be <1). In this case Kapton based sails can get to 0.1-0.13 AU and CP1 (and Mylar) based sails get to 0.15-0.18 AU. That is, even assuming a theoretical limit, polymer-based sails are not capable of reaching beyond 20 $R_{\odot}$. By substituting low melting/glass transition point polymer substrate with higher temperature films the sails may be brought closer to the sun. However, in this case relatively low melting point of aluminum (~930 K) and its relatively high absorption (~10%) limit the use of aluminum to ~12−15 $R_{\odot}$ minimum perihelion, as shown in Fig. 3.7.
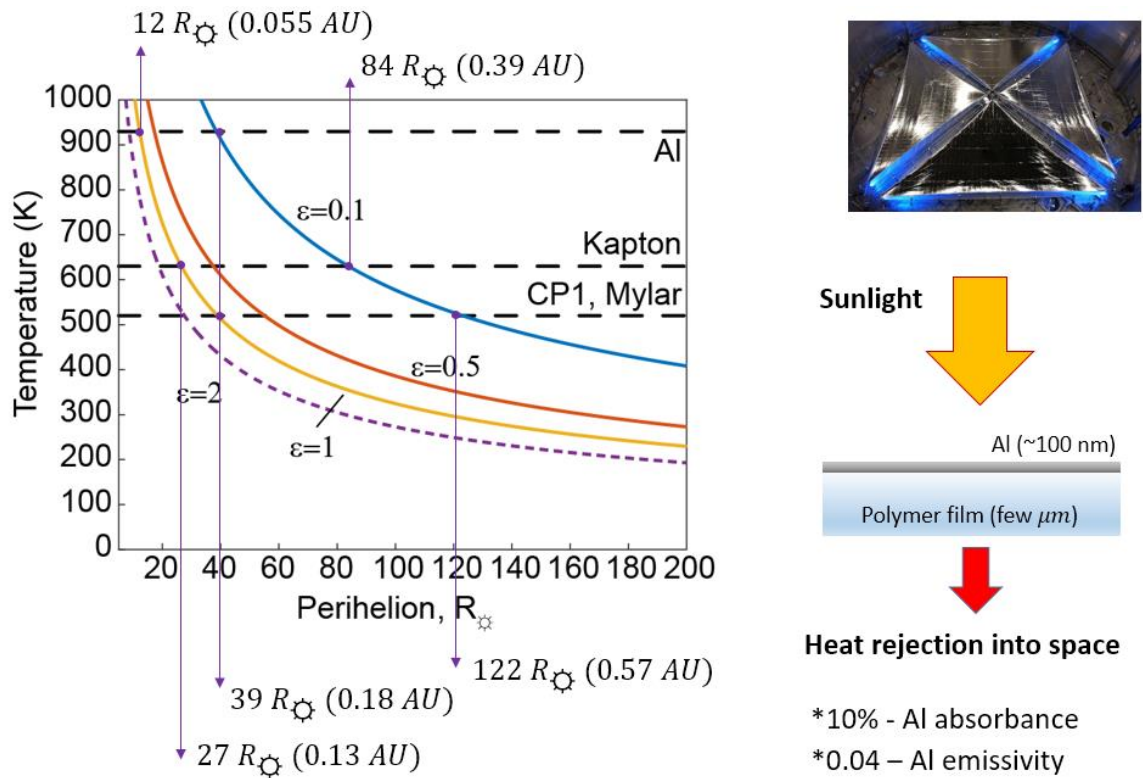
Figure 3.7 Calculated temperature of an aluminized sail material with perihelion distance for different sail backside emissivities. Dashed lines denote melting/glass transition points of respective sail material constituents. Here, the sail absorptivity is set as α=0.1, which corresponds to 10% of sunlight absorption in Al.

3.4 Materials for extreme solar sailing

Sun is continuously emitting electromagnetic radiation as a black body at ~5770 K. The spectrum of this radiation in space at Earth orbit is known as Air Mass Zero (AM0) spectrum (Fig. 3.8). And the overall irradiance at Earth orbit is ~1360 W/m^2. The intensity of radiation varies inversely proportional to heliocentric distance. In this study we view the sun as a point source, where the irradiance scales with the distance as:

$$I_{sun} = S_{1AU} \left(\frac{1AU}{d_0} \right)^2$$

(3.3)
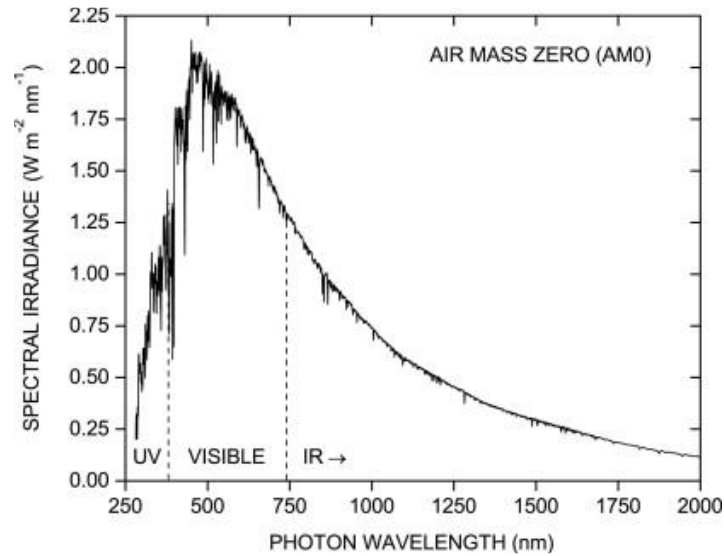
Figure 3.8 AM0 solar spectrum.

Solar spectrum is very broadband, therefore sail materials must reflect a significant fraction of the entire spectrum (desired reflectivity >0.7) and withstand damaging radiation effects across all spectral bands, particularly high energy part (UV) of the spectrum.

To find the suitable material for extreme solar sailing, a numerical model is developed to analyze the equilibrium temperature of sails made of different high

temperature materials. Sail temperature is found as power balance between absorbed solar radiation and the emitted thermal radiation (as shown in Fig. 3.9(a)):

$$P_{sun}(d_0) = P_{rad}(T)$$

(3.4)

where

$$P_{sun} = A \int_0^\infty d\lambda \, \alpha(\lambda) \, S_{1AU} * \frac{1}{d_0^2}$$

(3.5)

in which A is the area of the sail, α is the absorptivity of the sail, d_0 is the distance to sun in solar radii, λ is the wavelength, and

$$P_{rad} = A \int d\Omega \cos \theta_e \int_0^\infty \epsilon(\lambda) I_{BB}(T, \lambda) d\lambda$$

(3.6)

where ϵ is the emissivity of the surface, I_{BB} is the blackbody radiation at temperature T, and $\int d\Omega \cos \theta_e$ is the angular integral of the emission. Note that the absorption spectrum and the emission spectrum here are essentially the same since we are solving the problem in an equilibrium state. The inputs of this model is spectral absorptivity α (or ϵ) of the sail material, and the distance from the sun d_0. We define the input that generates the lowest equilibrium temperature in this model as the ideal spectrum. The ideal spectrum of a solar sail material is schematically shown in figure 3.9(b). The reflectance should be as high as possible across the wavelength range of incident solar radiation to minimize absorbance, whereas it is desirable to have thermal emissivity close to 1 elsewhere to maximize radiative cooling.
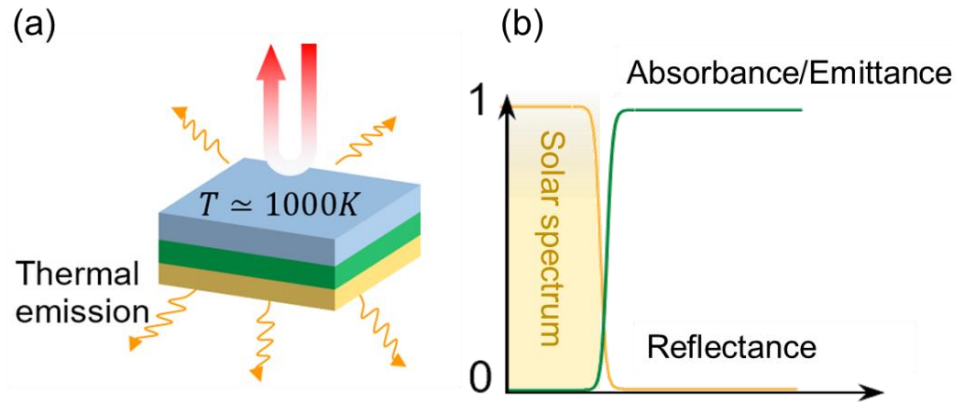
Figure 3.9. (a) Schematic of a sail material reflecting solar radiation and using thermal radiation to balance the sail temperature. (b) Schematic illustration of an ideal spectral response of the sail material.

To understand sail design criteria, we have conducted an extensive analysis of potential material candidates. A list of materials that includes materials from different categories that resemble the ideal spectrum are surveyed and their potential use for solar sailing is analyzed. In our survey we have examined refractory metals, high temperature ceramics, and emerging materials such as hexagonal boron nitride and graphene. In Fig. 3.10, we compare solar radiation absorptivity of various materials. Here materials with >1000 K melting point were chosen. Refractory metals and compounds generally exhibit high solar radiation absorptivity, although at the same time possess higher melting point (data for aluminum currently used in solar sails is plotted for comparison). Many of high temperature ceramics are transparent dielectrics and demonstrate low absorptivity across solar spectrum. However, in general dielectrics have lower melting point as compared to refractory metals and alloys.
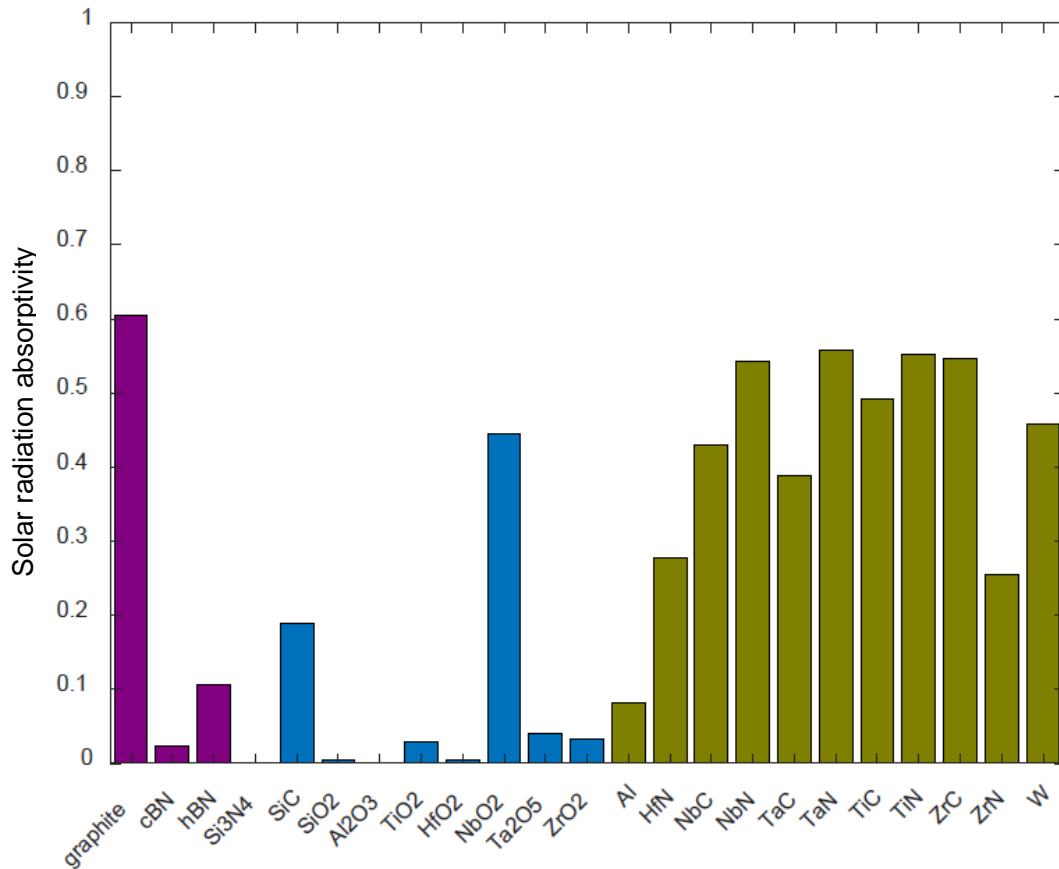
Figure 3.10 Solar absorptivity for metals (yellow), ceramics (blue), and boron nitride and

graphite (purple).

Next, based on simple radiation balance between solar power absorbed (across

entire solar spectrum) and thermal radiation dissipated into free space, we have studied the

closest distance to the sun a given material can reach. As many materials have a limited

availability of measured data on optical properties (i.e., refractive index and extinction),

particularly across such a broad range of wavelengths (i.e., from 100 nm to >10 μm), we

have developed a "digital spectrum" model. The model allows assessing performance of

materials with missing spectral data, and more importantly to simulate the effect of having

engineered spectral response. In this analysis, we combine real material data with an

idealistic spectrum for wavelength ranges where data is missing. Figure 3.11 shows an example of such hybrid spectrum.
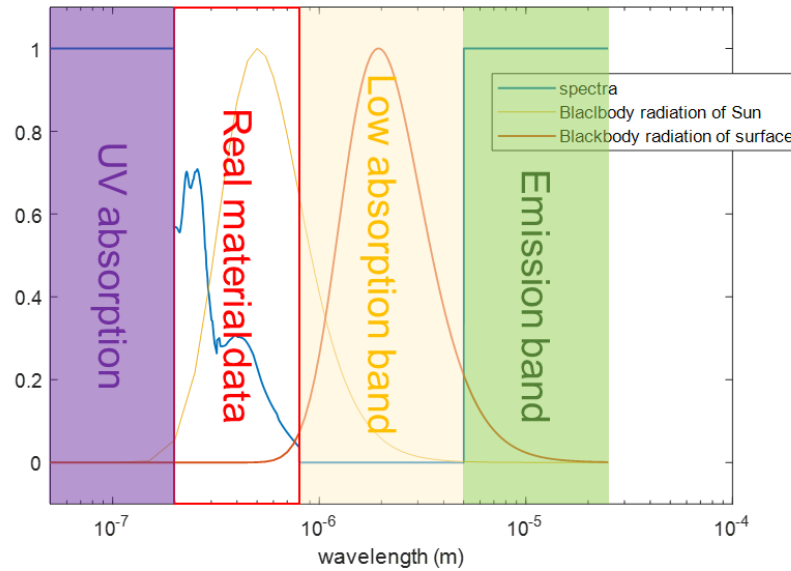
Figure 3.11 An example hybrid spectrum (blue curve) consisting of UV absorption band, real material data, low absorption band, and emission band.

In Fig. 3.12 we plot the minimum perihelion distance for solar sails made of different materials (here closest approach is defined by the temperature at which melting point for a given material is reached).
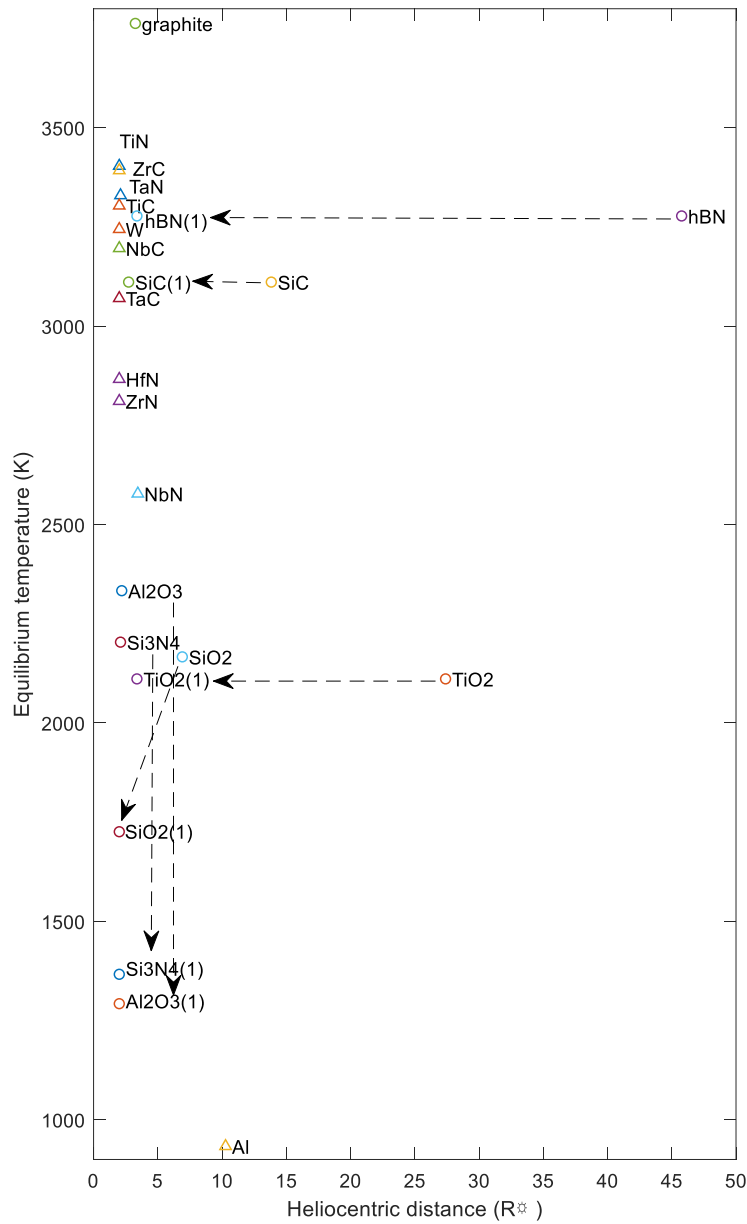
Figure 3.12 The graph plots the closest heliocentric distance for sails made of various materials. The x axis is the perihelion distance, and the y axis indicates the equilibrium temperature of the sail at the corresponding distance. Refractory metals and metal compounds are denoted by triangular marker, ceramic materials and graphite are marked by circles. The arrows indicate the expected improvement with thermal emission engineering (see description in the text).

74

As can be seen metals and dielectrics present two conceptually different alternatives for sail design. As metals are not transparent (we assume 100 nm thick) to solar radiation their backside emissivity may potentially be engineered to reach unity (e.g., by depositing thermally emissive coatings as will be discussed later). Therefore, for metallic sails (denoted with triangles in Fig. 3.12) we assume emissivity of unity to estimate sail temperature and minimum perihelion. Of course, many metals and metal compounds may have high infrared absorptivity on their own, particularly at elevated temperatures, which would contribute to further improvement of the performance. Here, however we neglect the emissivity of metals and assume only unity backside emissivity. That is, our estimate is on a conservative side. According to Fig. 3.12, most of refractory metals and metal compounds can get to $2R_\odot$ (minimum distance considered in this study), despite their very strong solar absorbtivity (Fig. 3.10). Aluminum for comparison can get only to $12R_\odot$ in a best case scenario. At the same time, the temperature of such metals exceeds 2500 K and in many instances reaches >3000K.

For dielectric sails (which are thin film) solar radiation interaction with the entire body of material needs to be taken into account (that is, backside of the sail cannot be considered independently as is done for metals). In this case we assume 100 nm thick materials and study their solar absorptivity and double sided thermal emissivity that a given material exhibits. We observe that thin 100 nm thick films of SiN, Al_2O_3 can get to $2 R_\odot$. Other dielectrics possessing much narrower infrared emission bands cannot get as close (the closest is for SiO_2 at $7 R_\odot$, the range of other dielectrics studied (i.e., TiO_2, hBN, and SiC) is $>15 R_\odot$). By engineering the thermal emissivity (e.g., by properly nanostructuring materials) the range and perihelion distance of dielectric based materials can also be

75

improved. To emulate such a scenario, we have assumed a unity spectral emissivity for $\lambda \geq 5$ μm, while keeping solar absorptivity of sail materials as is. The result of such a hypothetical scenario is indicated with dashed arrows in Fig. 3.12. In this hypothetical case the temperature of SiN and Al_2O_3 can be reduced to below 1500 K, whereas SiO_2 can be brought to 2 $R_\odot$ with ~1750K. hBN and SiC can be brought to ~3 $R_\odot$, although temperature of these materials will exceed 3000K even in the hypothetical case.

In addition to temperature and optical properties of candidate materials, we have taken into account materials density. Per this survey we find that silicon nitride (SiN) and titanium nitride (TiN) as the best possible candidate materials for a solar sail design owing to their high melting temperatures (2170 K and 3200 K, respectively), their potential ability of reaching small perihelia, good optical properties (see discussion below), and low mass densities (3.17 g/cm^3 and 5.4 g/cm^3, respectively). Other good material options include SiO_2, hBN, and Al_2O_3.

TiN and SiN exhibit drastically different properties and provide two distinctly different alternatives to designing solar sails. Specifically, we identify two conceptual approaches to high temperature solar sail material design: metalized sails and dielectric sails, see Fig. 3.13.
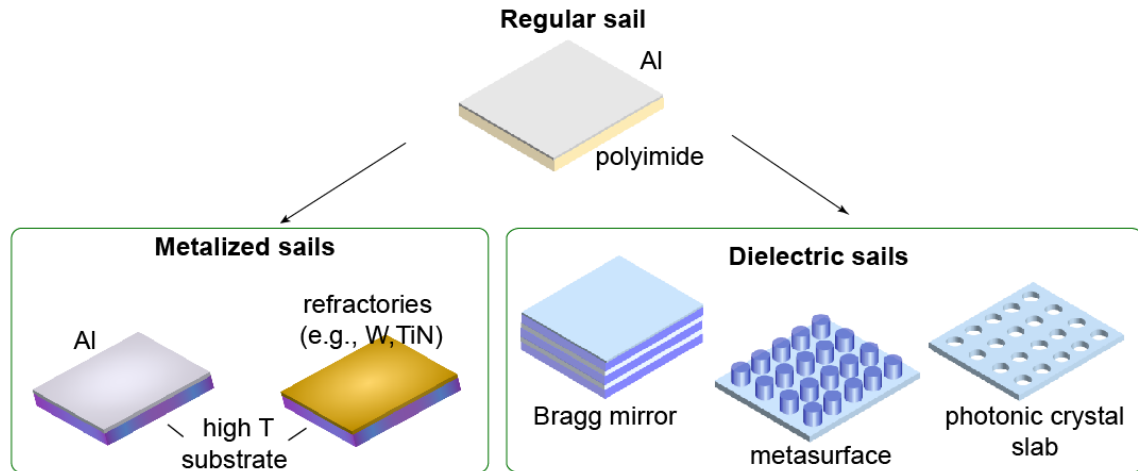
Figure 3.13 Two possible approaches for extreme metamaterial solar sail design, after

Ref. [58].

With a knowledge on the performance of various materials, we suggest two approaches to realize an ultra-lightweight solar sails that can survive strong radiation flux near the sun (Fig. 3.13). The first approach is based on metalized sails with polymer substrate substituted with higher temperature films. For example, by substituting low temperature polymers with higher temperature (e.g., >1000 K) inorganic substrate materials, the operation temperature of aluminized sails increases to 900 K (limited by the melting point of Al itself). TiN is a high temperature ceramic exhibiting metallic properties [114]. A metamaterial design based on TiN is reminiscent of the currently used aluminized polyimide sails [96, 99, 111, 112]. Specifically, a TiN-based sail comprises a ~75 nm thick TiN film that is deposited atop of a sub-micron thick inorganic high temperature film which acts as a substrate (e.g., graphene composites, carbon nanotubes (CNT) or boron nitrite composites [115-122]). TiN-based sails would reflect about 60% of sunlight and absorb the other 40%. This corresponds to 80% efficiency for momentum transfer under normal incidence as compared to an ideal flat perfectly reflecting sail. To control temperature raise

and prevent overheating, the backside of the substrate is coated with a thin thermally emissive surface that functions to cool by radiative means. For example, a 500-nm thick CNT film [121] is expected to have emissivity of $\epsilon \approx 0.7$ at $T \geq 1800\ K$, which can be further enhanced by depositing few nm of tungsten (W) [123] (being metallic in nature, sun-facing TiN surface has very small emissivity $\epsilon \leq 0.05$). Our calculations indicate that such films may get up to 3R☼ perihelion before reaching a melting temperature of 3200 K (Fig. 3.14). The overall design has an areal density of 0.96 g/m^2, with melting point over 3000 K.
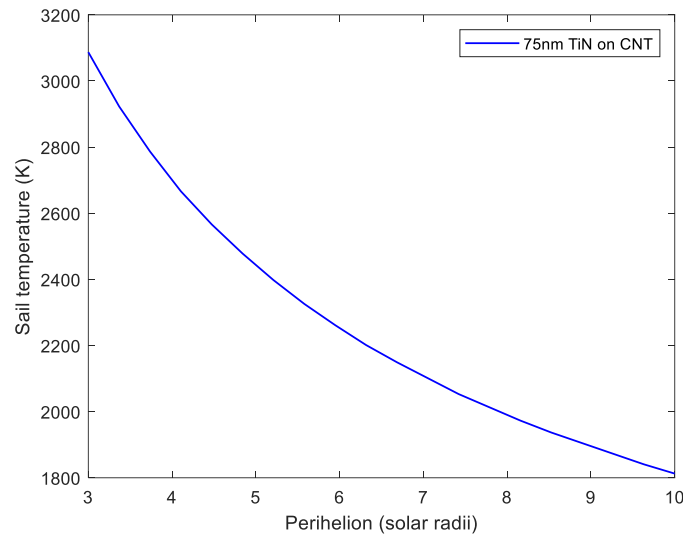
Figure 3.14 TiN based solar sail. Sail temperature with perihelion distance. Inset shows sail schematic. Melting point of TiN is ~3200 K

Silicon nitride (SiN) presents a conceptually different alternative to metamaterial sail design. Thin SiN-based films absorb sunlight only weakly ($\leq 0.1\%$). With proper emissivity control, the combination permits maintaining of relatively low temperatures ($\sim 1600\ K$) even at very close perihelion distances ($<3\ R$☼ from the surface of the sun). However, SiN, being naturally transparent, reflects only a fraction of the sunlight and consequently is not efficient for momentum transfer and adequate creation of propulsive

thrust. To boost the reflectivity of SiN and enhance radiation pressure momentum transfer, nanostructured metamaterials [124-128] made of SiN [129, 130] can be used.

For this purpose, we have examined several SiN nanostructured thin films that are ultralight and possess high reflectivity. Figure 3.15 shows two conceptual designs one based on multilayer films (i.e., Bragg stack) and another utilizing a photonic crystal structure. In both cases, films with an areal density of ~1 g/m^2 and ~60% solar reflectivities can be designed. Figure 3.15 (right) shows spectra for the two structures across the visible band. A broadband reflectance of solar radiation is possible (solar reflectivities ~60% are possible). Designs with higher reflectance at a cost of a slightly higher areal density are also possible.

The multilayer design exhibits lower solar absorptivity and can potentially get to 3 R☼ perihelion while maintaining temperature <1700K, which is well below the SiN melting point, as shown in Fig. 3.15 (left). The grating design exhibits a slightly higher solar absorptivity, and therefore can get to about ~6 R☼ perihelion. While SiN metamaterial fabrication is more elaborate, lower temperature of such metamaterial does present a more attractive approach when compared to TiN.
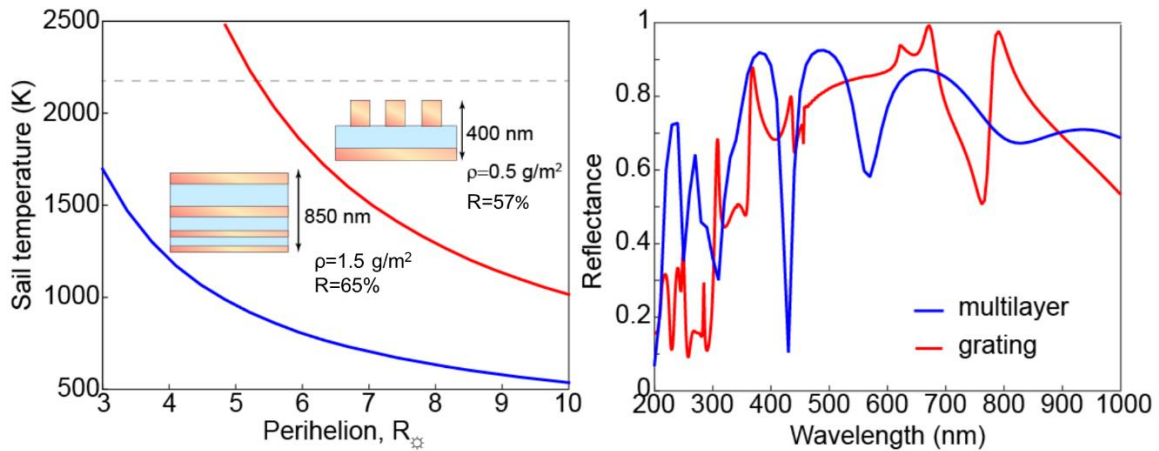
Figure 3.15 SiN metamaterial sail. Calculated temperatures (left) and spectra (right) for two optimized meta-structures. Insets show schematic illustrations of geometries. Here silicon nitride layers are separated by vacuum gaps (e.g., with the use of aerogels or microarchitectured "honeycomb" truss)

3.5   Chapter conclusions

Extreme solar sailing allows accelerating spacecraft to velocities well beyond the reach of regular rockets. Such extreme missions necessitate high temperature solar sails that can get very close to the sun and endure extreme environment of solar corona. We have outlined key trade parameters for sail materials designs. We then surveyed material candidates for high temperature solar sails and showed that several different material classes exist, which could potentially allow getting to 2-5 solar radii perihelion. We then discussed nanophotonic strategies to design lightweight and high reflectivity solar sails that can meet stringent mission criteria. Two distinct sail material design approaches were identified and discussed.

CHAPTER 4

Solar sail material fabrication

In this Chapter we examine methods for fabricating ultrathin polymer-free sail materials. Our study discusses fabrication approaches for depositing specularly reflective metallic films atop of free-standing carbon nanotube films. Optical properties and thermal performance of fabricated samples is examined.

4.1 Two-layer sail material design

As mentioned in Chapter 3, increased solar radiation flux for small perihelion missions challenges design of sail materials. Conventional sail materials made of polyimides (e.g., CP1 and Mylar) [96, 111], which have low glass transition and melting points (~520K) [131]. As such current solar sails can't get closer than 0.5AU perihelion. Therefore, getting closer to the sun (e.g., <0.2AU) necessitates developing sail materials that are based on high temperature components. The idea of removing polymer substrates has been examined since 1970s [132]. For example, it was suggested that freestanding ultrathin metallic films (e.g., Al) can be used for the purposes of solar sailing. Other ideas, such as graphene and beryllium sails have also been expressed recently [107, 109]. However, to the best of our knowledge, practical implementation of these proposals is yet to be examined. Following the design approaches outlined in Chapter 3, in this Chapter we study a bi-layer design where polymer substrate is substituted with an inorganic thin film. We explore fabrication of such thin film solar sail materials, and examine optical properties in the context of future solar sail missions.

Thin film fabrication technology has matured along with the advancement in semiconductor industry. The film thickness, surface quality, and electric properties can be well controlled with near atomic precision. However, most of the fabrication methods are perfected for thin films on substrates, and the fabrication of ultrathin non-polymer freestanding films remains nontrivial. Such freestanding thin films are of great interest for many emerging applications. For instance, metallic freestanding thin films are of importance for flexible transparent electrodes to be used in displays. Other applications include membrane filters and catalysts [133-135]. While several different studies on fabrication of freestanding metallic films have been performed in prior years, study of optical and thermal properties of such ultrathin films is lacking. In particular, in the context of the solar sailing high optical performance (i.e., specular reflection) and small areal density are highly desirable.

As fabrication of large area freestanding metal films can be challenging, we chose to fabricate such films atop an ultrathin carbon nanotube (CNT) substrate film. Our choice of CNTs is motivated as follows. Firstly, large area mechanically robust free-standing in ambient atmosphere carbon nanotube films as thin as 200 nm with ~160 MPa tensile strength have been demonstrated recently [136]. Secondly, carbon nanotubes have potential for high thermal emissivity [137-139]. Third, carbon nanotubes can withstand very high temperature environment, exceeding 1000° C [140, 141] (although structural transformations for single wall nanotubes have been reported at ~1800° C [142]). Furthermore, carbon nanotubes films and composites are lightweight (~1.3-1.4 g/cm^3) due their porous nature.

82

In our study, we chose to work with multiwall CNTs [143], however, our results can be extended to single wall CNTs as well. While several different techniques exist to fabricate submicron CNT thin films, including spin coating [144], spray coating [145], blade-coating [136], and vacuum filtration [146] for the sake of simplicity in our proof-of-concept studies we chose to work with the vacuum filtration method. We further note that while a number of works reported ultrathin CNT fabrication, study of optically smooth surfaces has not been performed yet.

As a baseline for sail materials design we consider a bi-layer film, schematically shown in Fig. 4.1. The top layer is ~100 nm of specularly reflective metallic film, whereas the bottom layer is a thin, ~1 µm thick, CNT film serving as a robust support substrate. In our experience a substrate is needed as ~100 nm thick metal films are not stable and can't be made freestanding over large areas. On the other hand, while thicker metal films are stable and can be easily handled, their areal density becomes large for future sail material applications.
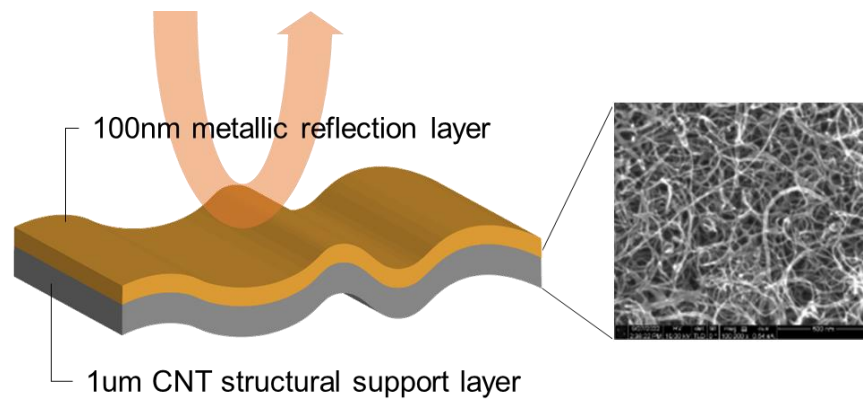
Figure 4.1 The two layer sail material designed for extreme solar sailing

4.2 Limitations of current polyimide films

To understand limitation of materials currently used in solar sailing, we have performed thermal tests in ambient atmosphere. Specifically, we examined Mylar and Kapton films on a hot plate. In Fig. 4.2(a) Mylar is shown on the left side and Kapton on the right side. Both films are fixed on a frame of aluminum foil. The two samples are then put on the hotplate of increasing temperature in ambient atmosphere for 10 minutes for 200~400 °C. The samples do not show visible notable change at 200 °C (fig. 4.2(b)). However, at 300 °C Mylar starts to burn. Mylar film partially disappears as shown in Fig. 4.13(d), while Kapton is not showing any visibly notable changes (Fig. 4.2(c)). At 400 °C Mylar nearly completely disappears (Fig. 4.2(f)). At this temperature, brown spots start to show up atop Kapton film, and the film starts to ripple (Fig. 4.2(g)). As a result, the maximum operation temperature of Mylar is below 300 °C, while the operation temperature for Kapton can be above 300 °C and below 400 °C. While these tests are performed in ambient atmosphere, they give a good idea of limitations organic films have. Even in vacuum decomposition of organic films at <500 °C is expected.
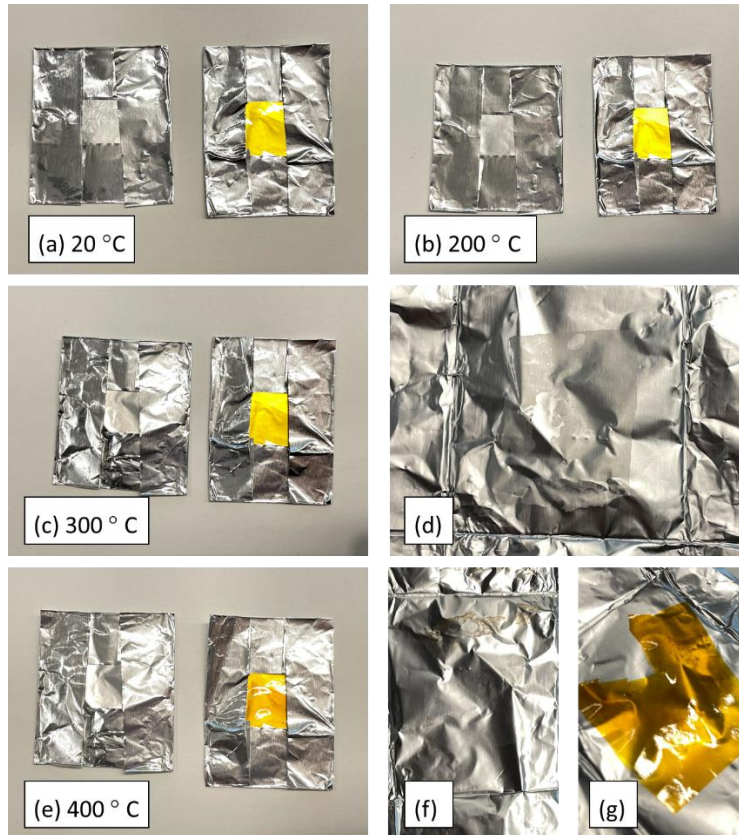
Figure 4.2 (a) 0.5 μm Mylar and 7 μm Kapton film at room temperature (b) after 10 minutes on 200 °C hotplate. (c) after 10 minutes at 300 °C (d) Mylar film damaged at 300 °C (e) after 10 minutes at 400 °C (f) Mylar film mostly gone. (g) Kapton film showing signs of burning.

4.3 The choice of metal coating for sail materials

To understand the influence of metal coatings on the performance sail materials, in Fig. 4.3, we plot the projected sail material temperature as a function of perihelion for Al, Pt and TiN coatings. The temperature of the sail is estimated assuming thermal equilibrium (see Eqs. (3.4)) and assuming that optical properties do not vary as a function of temperature. For this estimate we use optical constants for afore mentioned materials measured at room temperature [147-149]. We further assume that the backside emissivity is in the range of 0.5-1.

Evidently, the choice of front side coating largely affects the closest distance to sun a potential solar sail can get to. Smaller absorptivity of Al (~10%) as compared to Pt and TiN (~60%), results in a lower temperature of the Al–based sail material. However, low melting point of Al precludes from getting to <~15 $R_\odot$ perihelion. Pt offers a higher melting point while at a cost of higher solar absorptivity. Pt based sails can potentially operate as close as 6 $R_\odot$ perihelion. A much higher melting point of TiN allows getting as close as 1.3 $R_\odot$ from the surface of sun (although at these distance other effects, such influence of solar corona plasma need to be considered).
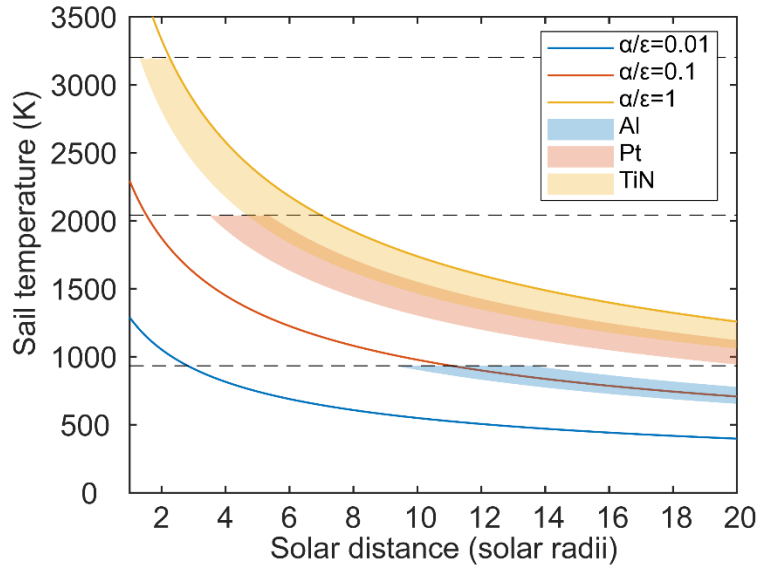
Figure 4.3 Sail material temperature as a function of perihelion distance for several different sail materials. Dashed lines indicted respective melting points.

4.4 Fabrication of thin films

The first stage of the overall sail material fabrication procedure assumes fabricating a smooth, thin, and freestanding substrate for subsequent coating. In the context of solar sail materials development, optically smooth films are essential to minimizing undesired sunlight absorption and maximizing solar reflectivity to achieve high radiation pressure.

4.4.i Graphene oxide films.

At initial stages of this work we examined fabrication of freestanding graphene oxide (GO) film with vacuum filtration. Despite knowing the fact that graphene oxide degrades at an elevated temperature (starting from 325°C) [150], we use GO thin film as a platform to test the fabrication approach during the early stages of this project. Vacuum filtration is adopted due to its capability to fabricate ultrathin freestanding films. The process uses vacuum filtration to create a constant flow inside the GO flake-water

87

suspension. The flow aids the flakes to align themselves and create a robust film via self-assembly [151-153] (Fig. 4.4). The GO film is then peeled off from the filter membrane after drying.
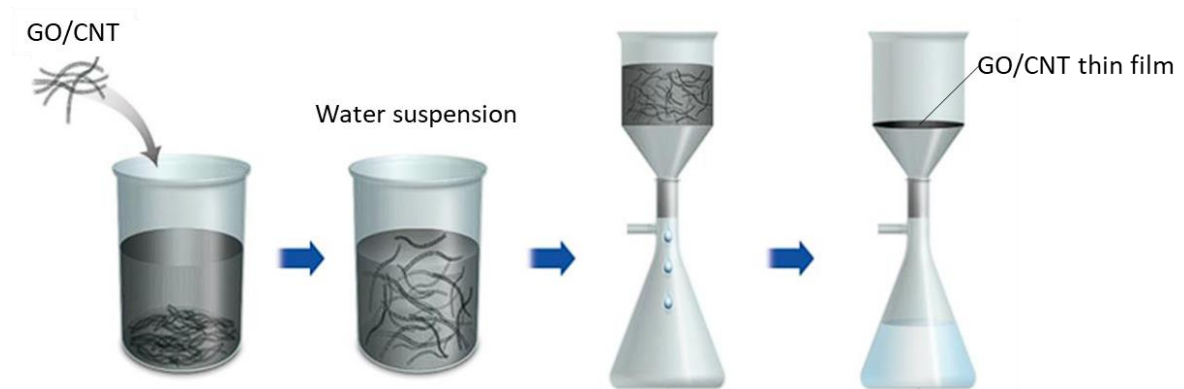
Figure 4.4 Vacuum filtration for GO and CNT thin films. Figure altered from [154].

Figure 4.5(a) shows a photograph of the vacuum filtration set up, and Fig. 4.5(b) depicts a fabricated free standing GO film. The fabrication method can be directly applied to other materials, such as boron nitride and carbon nanotubes, and graphene composites.
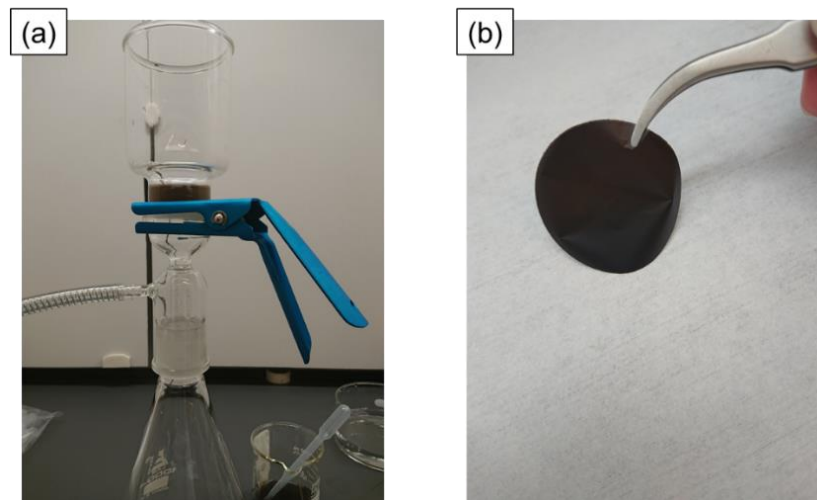
Figure 4.5 (a) Vacuum filtration setup. (b) Freestanding GO film.

From Fig. 4.5(b) one can easily observe that the GO film has a matte surface, which implies that the surface of the film is not optically smooth. In order to prepare an optically

smooth surface we modified the fabrication process. Specifically, an atomically smooth piece of silicon wafer is placed on top of the liquid suspension during the process of vacuum filtration, and the smooth surface of silicon wafer helps the GO flakes to align in a laminar fashion while the water dries out (Fig. 4.6).
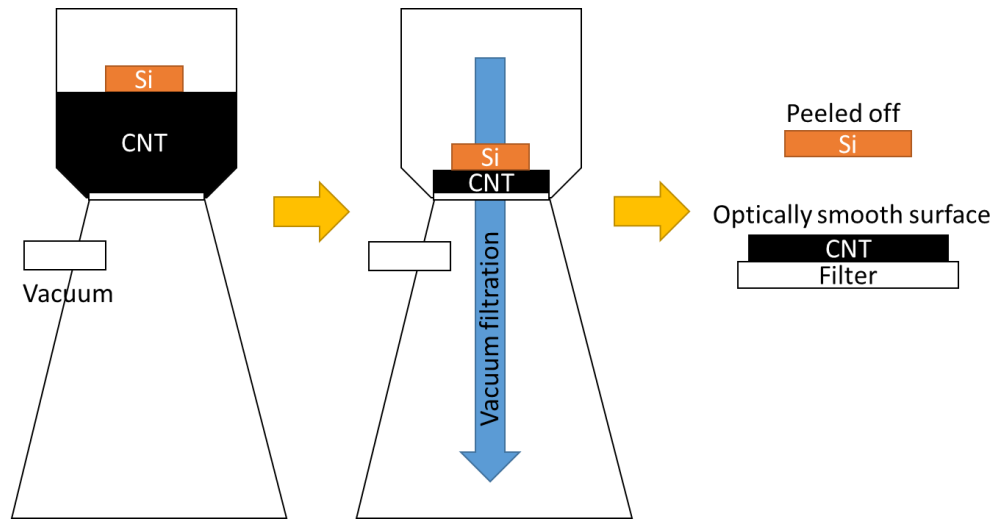
Figure 4.6 Silicon chip assisted vacuum filtration.

Figure 4.7 compares the surface roughness of GO films produced with and without the help of silicon wafer. Figure 4.7(a) shows the optical microscope image of the GO film fabricated with silicon wafer, and Fig. 4.7(b) depicts the result of fabrication without use of the silicon wafer. The silicon chip assisted fabricated shows a smaller grain size as compared to a film made by common vacuum filtration.
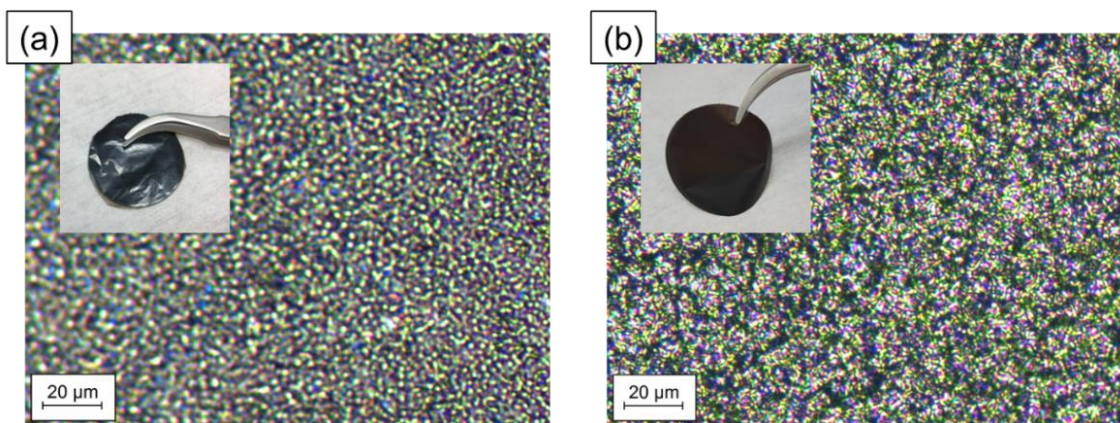
Figure 4.7 (a) the microscope image of GO film fabricated with the help of silicon wafer. The inset depicts photographic image of the respective film. (b) the microscope image of GO film fabricated without the help of silicon wafer. The inset depicts a photographic image of the fabricated film.

We also tried to further reduce the thickness by reducing the concentration of the GO suspension used. Figure 4.8 (left) shows a thin semi-transparent film that we have fabricated. Here we start by sonicating 1 mg of GO powder in 100 ml DI water. Then we use 10 ml of obtained suspension for each fabrication round. The estimated areal density is 1 g/m^2 for each 47 mm diameter film. Figure 4.8 (middle) proves that we are capable of maintaining the smooth surface while reducing the thickness of the film. Finally, as a test of this approach we have deposited a layer of ~30 nm TiN through sputter coating. As can be seen in Fig. 4.8 (right) the resulting surface is specular reflective too.
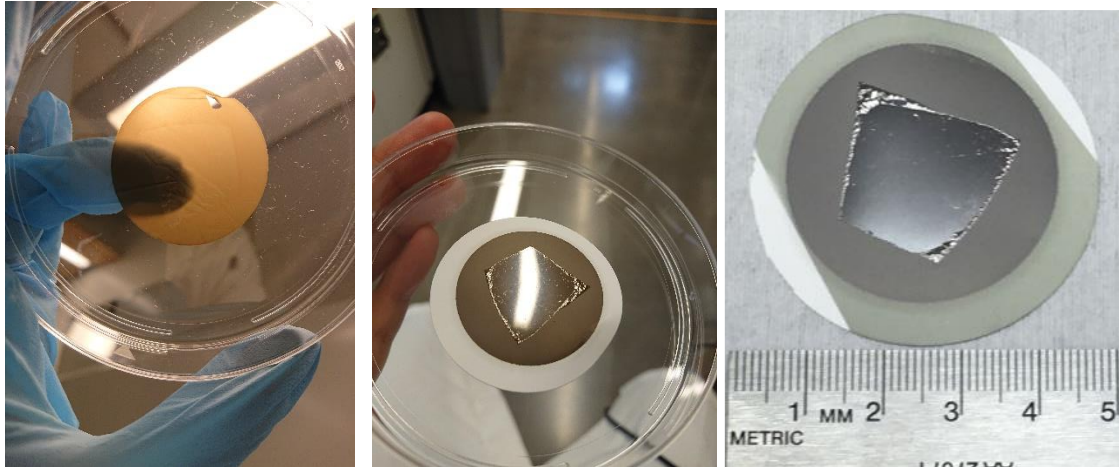
Figure 4.8 (Left) shows the transparency of the ultrathin GO film. (Middle) shows the specular reflection of the ultrathin GO film. (Right) smooth patch of GO film with 30 nm of TiN coating.

Despite the successful trials on GO film, it is not suitable for the final sample. GO film thermally reduces to reduced graphene oxide (rGO) as the temperature increase. During this process carbon atoms leave the surface in the form CO_2, and create voids on the surface [150, 155]. The voids increase the surface roughness of the film, resulting in a non-specular film, which is detrimental for solar sail applications. Although the defect on the film can be controlled through annealing and careful regulation of the temperature, it is out of scope of this research.

4.4.ii Carbon nanotube films.

We have therefore extended fabrication approach to multiwall carbon nanotube MWCNT films. We again use vacuum filtration to fabricate thin films. We use a commercially supplied MWCNT liquid suspension (water suspension of MWCNTs from NanoAmor; 2%wt MWCNT water suspension). We then dilute 1 g of the suspension in 150 ml water. We then take 4 ml of the diluted suspension and further add 6 ml of DI water

to it. The liquid goes through vacuum filtration and form a piece of CNT film on the filter paper. A centimeter size circular sample is fabricated, and the thickness of the CNT film is controlled by the amount of liquid suspension used. Figure 4.9 (top left) is a photo of a sample fabricated in such manner. Figure 4.9 (top right) displays an electron microscope image showing the surface morphology of the film. For samples shown here, the CNT layer is ~1µm thick as shown in Fig. 4.9 (bottom). To obtain the image in Fig. 4.9 (bottom), the CNT film is transferred from the filter paper onto a centimeter square silicon chip. The sample is then put under an SEM, and a trench is created using focus ion beam. The cross section can be observed by the SEM when the sample is tilted.
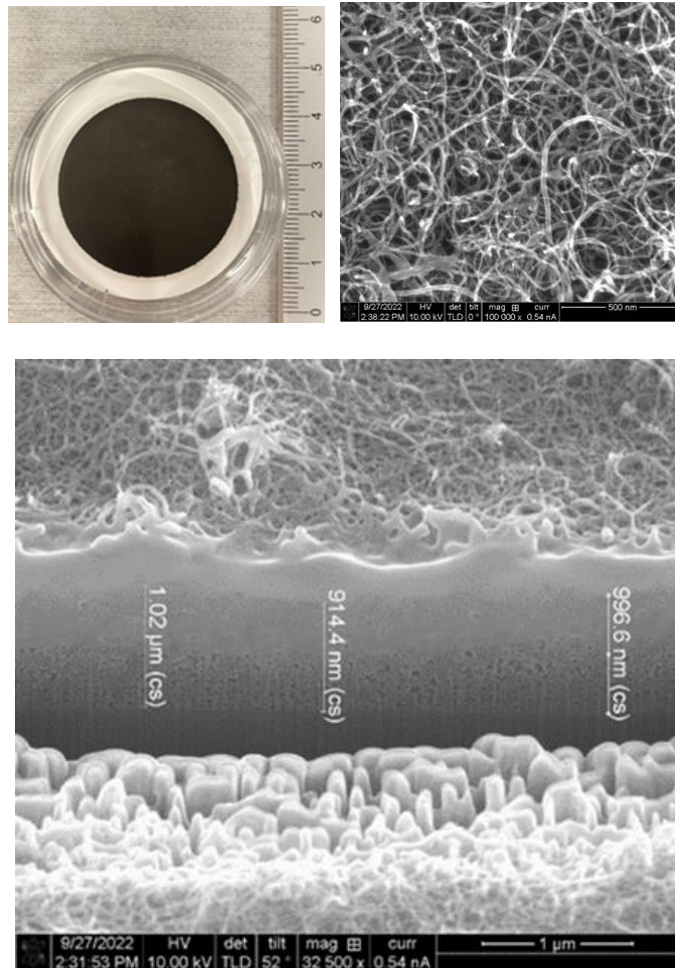
Figure 4.9 (top left) A photographic image of the fabricated MWCNT film attached to the filter membrane. (top right) SEM image of the surface morphology of the fabricated MWCNT film. (bottom) Cross-section SEM image that shows the thickness of CNT film fabricated by vacuum filtration.

At this point we faced another problem of separating the thin film from the filter paper to create a freestanding sample. Once the thickness of the fabricated films is too small, it becomes unfeasible to peel off by tweezers (as was done for GO in Fig. 4.7.a). We tried dipping the fabricated CNT/filter paper sample into liquid etchant to etch away the filter paper, however due to the CNT film being wetted by the liquid etchant, the CNT film

tends to break during the process of fishing it out of the liquid. To avoid the issues related to liquid etchants, we developed a different fabrication process to achieve a coupon size freestanding solar sail material sample suspended on a frame.

The surface finish of the CNT film, similar to the GO film, is unfortunately not optically smooth, making deposition of an optically smooth reflective thin layer on top of it to be a nontrivial task. Direct deposition on top of the CNT film simply gives a matted surface finish. With the developed fabrication process, we successfully circumvent the issue of rough surface finish and are able to obtain an optically smooth surface coating as the reflection layer. The overall fabrication process is shown in Fig. 4.10.
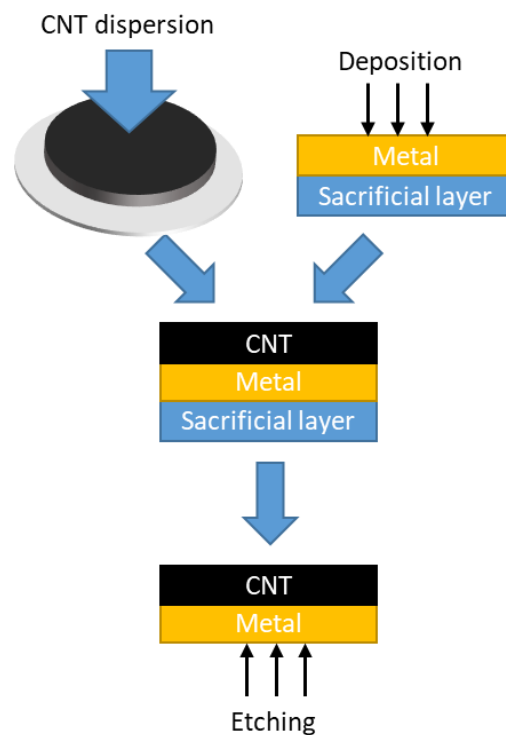
Figure 4.10 fabrication of metal coated CNT solar sail samples

4.4.iii Sacrificial layer assisted fabrication.

The fabrication flow is as follows. First, the CNT thin film is fabricated by vacuum filtration as discussed previously. The film is then separated from the filter paper by dissolving the filter paper with acetone, and instead of directly fishing out the CNT film, it is wet transferred in acetone to other substrates. This method is capable of transferring CNT films onto Kapton, Mylar, glass, and silicon substrates. Figure 4.11 shows a photograph of CNT thin films being wet transferred onto various substrates.
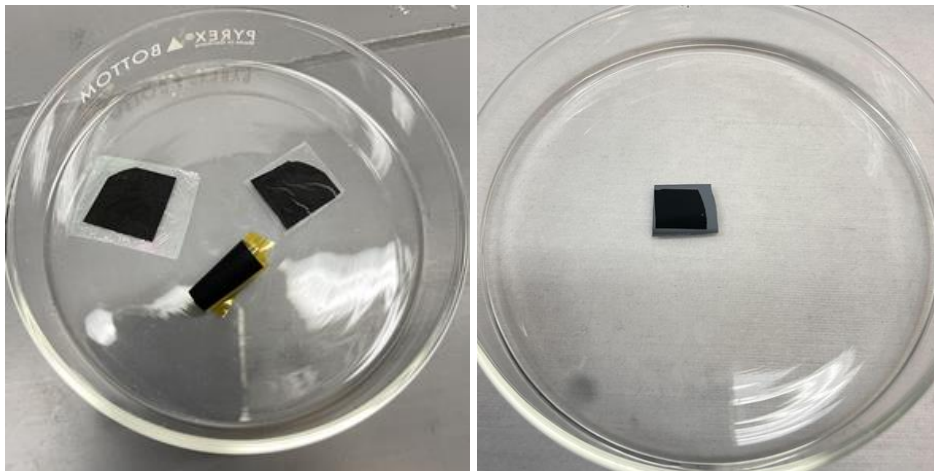
Figure 4.11 CNT thin films being transferred onto Mylar and Kapton (left), and silicon substrate (right).

However, even by transferring to an optically smooth surface such as silicon, the surface of the film is still not prepared for an optically smooth coating. Instead of directly depositing metal films onto fabricated rough CNT films, we deposit the reflective coating onto an optically smooth sacrificial substrate such as silicon or Mylar as the first step and then utilize transfer CNT film atop (see Fig. 4.10). The sacrificial layer is then dry etched away, keeping the freestanding bi-layer thin film material. For ease of handling, part of the sacrificial layer is kept on the samples as frames to hold the freestanding part. In our

fabrication, we deposit the titanium nitride reflective coating via sputtering, and platinum and aluminum by electron beam deposition.

For the first trial, we chose double sided 100 nm silicon nitride coated 525 µm thick silicon substrate as the sacrificial substrate. A centimeter size squared window of silicon nitride is etched away with 2.5 min of reactive ion etching (RIE), exposing the silicon underneath. Silicon can be further etched away to release thin film sample. This approach allows keeping a rather thick frame to support a freestanding thin film. 6 hr of 75°C KOH wet etch is applied to the substrate before the CNT film is transfer onto the backside. The silicon nitride acts as a etch mask in this step, and the KOH bath thins the exposed part of the silicon substrate down to 50~100 µm. After transferring the CNT film onto the backside, 1 hr of xenon difluoride dry etch is applied to etch away the remaining silicon. The 100nm silicon nitride would be etched away by the gas too. The reason of using dry etch as the final step to release the thin film, is to prevent the CNT film from breaking in liquid. Figure 4.12 plots the process flow that we adopted when using silicon nitride coated silicon substrate as the sacrificial layer. Both aluminum and CNT are highly selective to silicon and silicon nitride in fluoride etching.
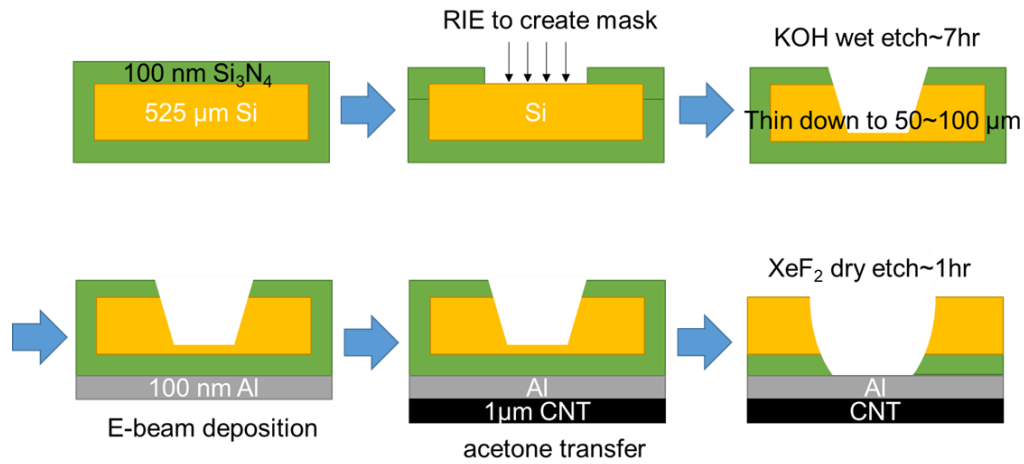
Figure 4.12 Fabrication process flow when using silicon nitride coated silicon substrate

as the sacrificial layer.

Fig. 4.13 shows freestanding sample suspended on a silicon frame. The sacrificial

substrate in the middle is etched away by fluoride vapor. The thin film in the middle is the

specular reflective aluminum layer with the 1 μm thick supportive CNT layer. The areal

density of the film is estimated to be 0.4 g/m^2. The exposed metal surface copies and

maintains the surface roughness of the smooth sacrificial layer throughout the process. Fig.

4.13 shows the front (left) and the backside (right) of the sample with the black CNT film.
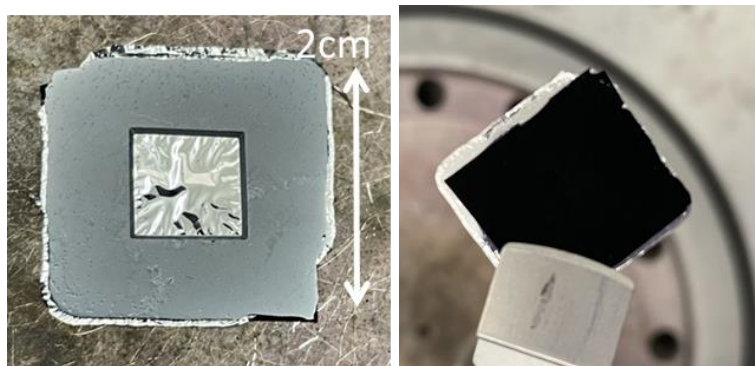
Figure 4.13 Front (left) and back (right) side photos of freestanding solar sail samples

suspending on silicon frames.

4.4.iv Film characterization.

The solar sail material, while being reflective, would inevitably absorb a portion of the solar radiation causing material heating. To understand materials behavior under thermal influence we have performed a thermal cycling test. Specifically, we have measured reflectivity of the sample before and after exposing to a high temperature environment. The spectrum is collected at 5 different points on a free standing sample by microscope reflectometer, and then the sample is subjected to 10 thermal cycles that is comprised of 1 minute on a 450 °C hotplate, and 1 minute of cool down in ambient air. We note that the ideal experiment should be conducted in vacuum (so as to mimic space environment), however, vacuum system that supports temperature as high as 450 °C was not available to us at the time of the measurement. Figure 4.14 compares the difference in reflectivity of the aluminum coated sample before and after the hotplate treatment, along with theoretical curve and the reflection of aluminum directly deposited onto a rough CNT surface. We also fabricated a sample that is fixed to a flat surface to eliminate the wrinkling of the film, which could potentially affect the reflectivity measurement. The results show that the reflectivity of the freestanding and fixed sample closely follows the theoretical curve for a 100 nm aluminum thin film. The reflectivity of the samples fabricated by the method developed in this paper is significantly higher than the reflectivity of aluminum thin film directly deposited onto the CNT surface (which is rough).
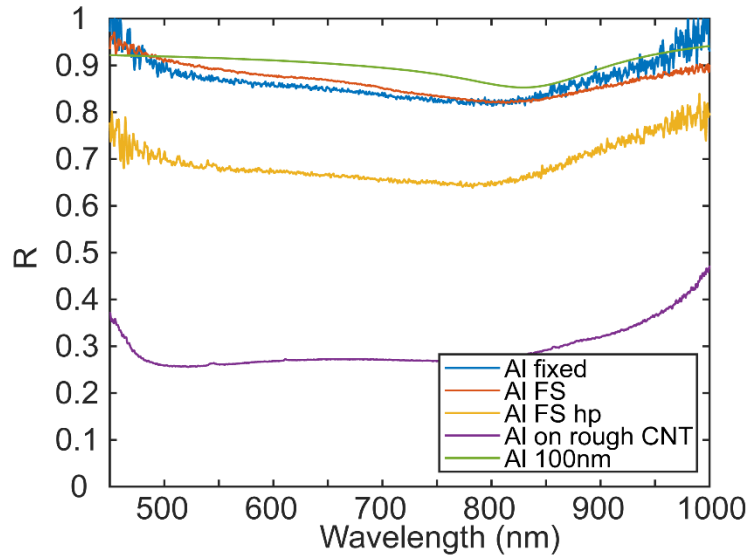
Figure 4.14 Reflectivity of aluminum coated solar sail material samples before and after heat treatment, compared to theoretical curve, a reference sample, and aluminum directly deposited onto MWCNT films.

This difference can be seen also in the photographic images presented in Fig. 4.15. The sample on the left side, fabricated by the above method, is specularly reflective, while the directly deposited aluminum on the right has a matte finish.
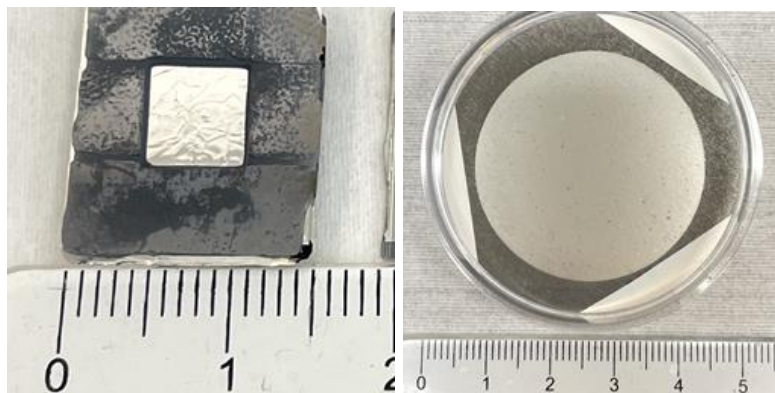
Figure 4.15 The reflective surface is optically smooth when fabricated following the method developed in this study (left), whereas the surface finish of the aluminum deposition is visibly rough when directly applied on top of vacuum filtration CNT films without any further treatment (right).

99

After thermal cycling, the reflection drops by approximately 20% (Fig. 4.14). To analyze the cause of the drop, we performed energy-dispersive X-ray spectroscopy (EDS) on the sample before and after thermal cycling. Using the fluorine component that the film gets from fluorine etching as a reference point, it can be observed that the oxygen component increases on the thin film after thermal cycling (Fig. 4.16), indicating oxidization of the aluminum film due to heating in the ambient air. Nevertheless, the film remains specular reflective as indicated by the photos in the insets. We can see that for both samples (i.e., pre thermal cycling on the left and post thermal cycling on the right in Fig. 4.16), the specular reflection is preserved and there is no visibly detectable change other than extra wrinkling of the freestanding film.
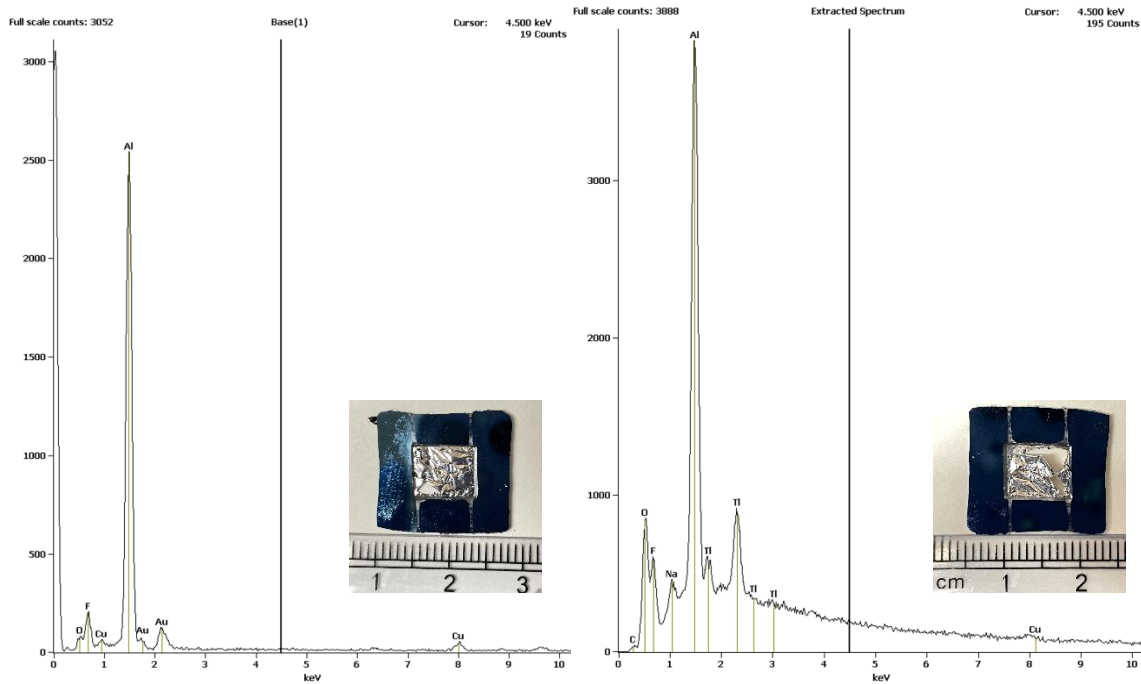
Figure 4.16 The EDS results and the photos of the solar sail sample before (left) and after (right) thermal cycling. The oxygen component on the Al side increases after thermal cycling. The insets are photos taken before (left) and after (right) the thermal cycle.

We further explore if thermal cycling causes microscale deformation of the films. For this purpose, we perform bidirectional reflectance distribution function (BRDF) of the sample before and after thermal cycling. This measurement probes the light scattered from the reflective surface and reveals information on macroscale surface roughens. The study of light scattering from optical thin films can provide useful information on thin film morphology. The power spectral density (PSD) of the surface roughness can be calculated and used to determine the change in roughness of the thin film sample. In order to determine the PSD function, BRDF method is used. BRDF measures the differential power of scattered beam dP per solid angle of receiver aperture $d\Omega$ in the θ_s direction and per incident power P_i coming from the θ_i direction. The angles used in BRDF are shown in Fig. 4.17.
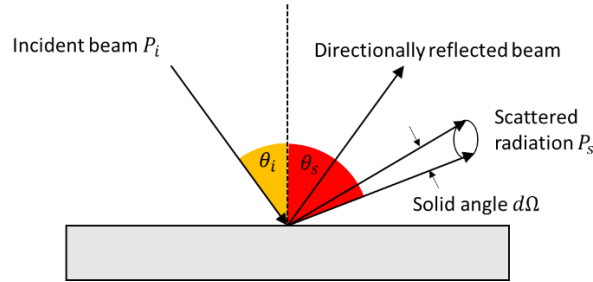
Figure 4.17 The angles defined in BRDF technique. Figure replotted from [156].

The PSD is presented as a function of spatial frequency, where

$$f = \frac{\sin\theta_s - \sin\theta_i}{\lambda}$$

(4.1)

and

$$\text{BRDF} = \frac{\frac{dP_s}{d\Omega}}{P_i \cos\theta_s}$$

(4.2)

where $\frac{dP}{d\Omega}$ is the measured scattered power per acceptance angle of the detector. Here we consider the surface to be relatively flat, and apply the Rayleigh-Rice vector perturbation theory, yielding a function that links the BRDF and PSD functions[156]

$$\text{BRDF} = \frac{16\pi^2}{\lambda^2} cos\theta_i cos\theta_s \, \text{PSD}(f)$$

(4.3)

This relationship allows us to extract the topographic structure of a surface from BRDF measurements.

The BRDF measurements are performed with an optical setup shown in Figure 4.18. It consists of a 532 nm laser diode as a light source with the beam diameter of 1 mm. The light scattered by the sample is measured with a Si photodiode detector (PD). The PD is mounted on a rotation stage with resolution of 0.1 deg. For a fixed angle of incidence, angular distribution of the intensity scattered in the plane of incidence is measured by rotating the detector around the sample.
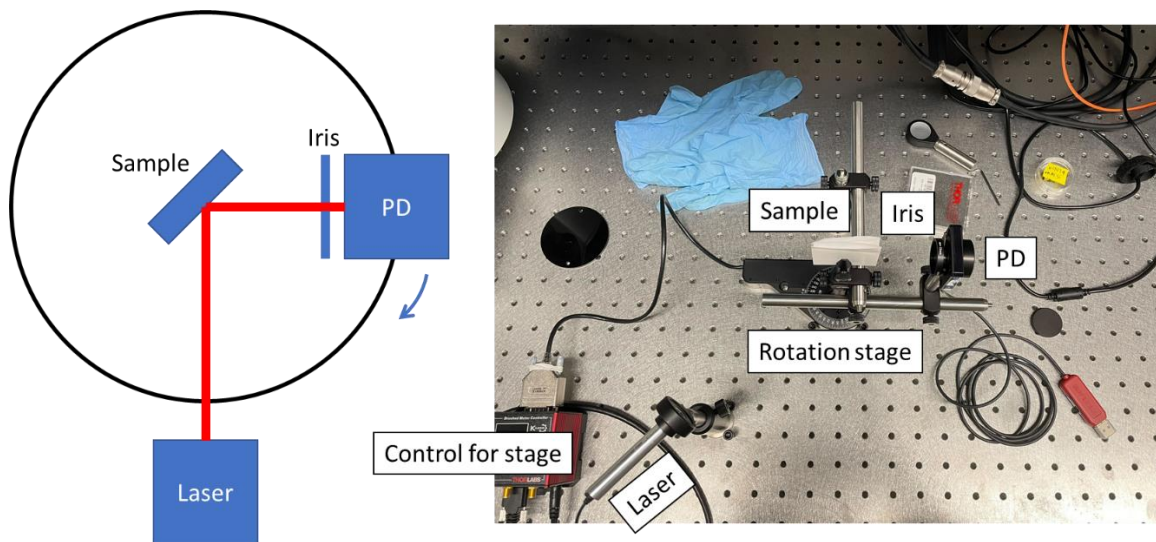
Figure 4.18 Schematic (left) and photo (right) of the setup for BRDF measurement.

Fig. 4.19 plots the PSD of the freestanding Al-on-MWCNT sample before and after thermal cycling, compared with a flat fixed samples. The directly deposited aluminum exhibits an optically rough yet macroscopically flat surface, as evidenced by its broadband behavior on the PSD plot. In contrast, the optically smooth and macroscopically flat mirror presents a curve that peaks at the origin. The freestanding sample, however, develops wrinkles upon the removal of the sacrificial layer. In the plot, we note a shift in the PSD curves of the freestanding sample away from the origin at the lower spatial frequency end, aligning with the fixed sample at the higher spatial frequency end. This suggests that they share similar microscopic features.

Upon comparing the PSD curve of the sample before and after thermal cycling, differences emerge at the low spatial frequency end, indicating some alterations in the macroscopic shape likely attributed to sample handling. Conversely, at the high spatial frequency end, the two curves closely resemble each other, signifying the preservation of microscopic features after thermal cycling.
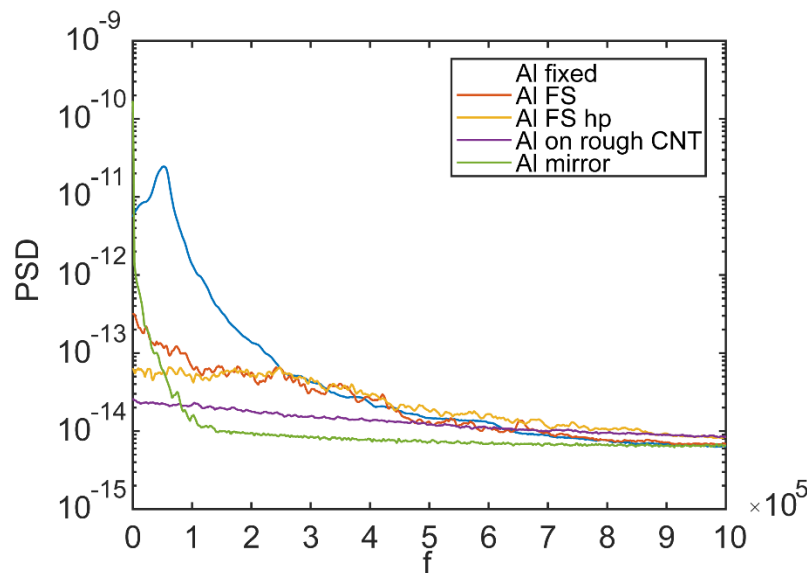
Figure 4.19 PSD of the freestanding sample before and after thermal cycling, compared with a flat fixed samples of aluminum directly deposited on CNT film and aluminum mirror.

4.4.v Pt and TiN sail materials.

Having investigated the changes in Al-coated CNT samples under elevated temperatures, we now shift our focus to the study of alternative coatings, namely Pt and TiN. In this exploration, we replace the 100nm aluminum with 100nm platinum using the same fabrication process. The reflectivity is measured and depicted in Fig. 4.20 (left), alongside the reflectivity of platinum deposited on a flat Si substrate for reference. A theoretical curve for a 100 nm platinum is also presented as a reference. The reflectivity of the freestanding sample demonstrates a strong correlation with that of the reference sample and the theoretical curve.

In Fig. 4.20 (right), a photo of the centimeter-sized platinum-coated freestanding MWCNT film suspended on the silicon frame is shown. A mirror-like reflection is evident, similar to the case of aluminum-coated samples studied above.
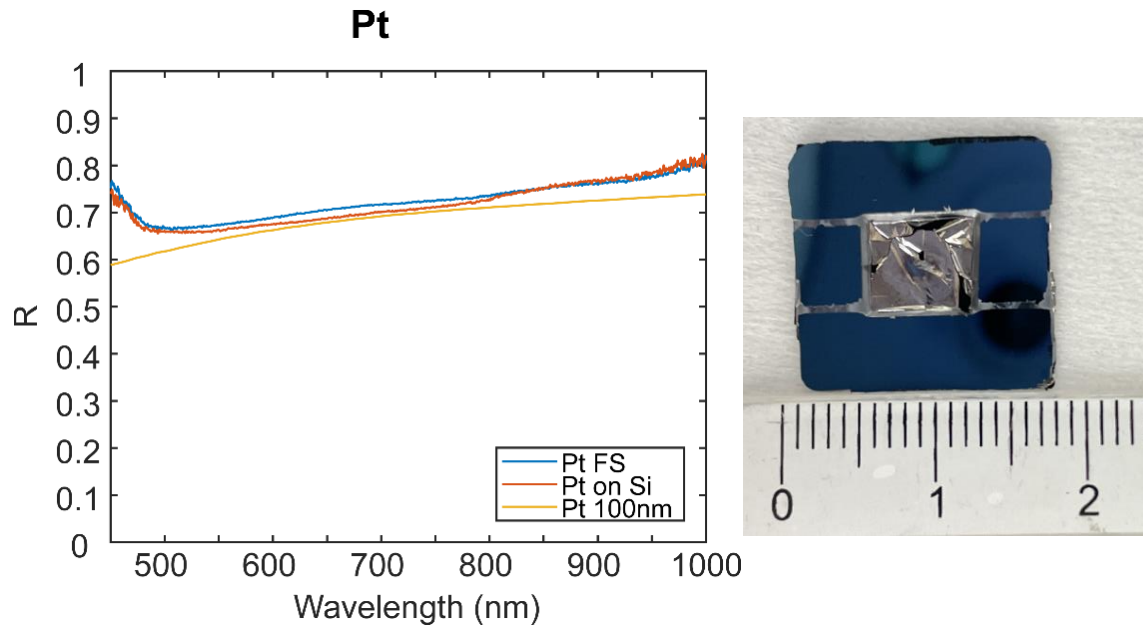
Figure 4.20 (Left) Reflectivity of solar sail material sample with Pt reflection layer, compared with reference sample and theoretical curve. (Right) Photograph of the fabricated Pt-MWCNT solar sail sample suspended on silicon frame.

Next we turn our attention to TiN sail material fabrication. Direct extension of the fabrication procedure used for Pt and Al is not applicable for TiN fabrication. Specifically, titanium nitride has low selectivity against the fluoride etching gas that we used to release the thin film from the sacrificial silicon substrate. To circumvent this issue, we maintain the overall fabrication process flow, however change the sacrificial layer to a 0.9 μm thick Mylar thin film. In this case Mylar is removed by O_2 plasma reactive ion etching (RIE). First, approximately 100 nm of TiN thin film is deposited onto 0.9 μm thick Mylar film via sputtering. A centimeter size 1 μm CNT thin film is then transferred on top of the TiN. Finally, the Mylar film is etched away via 10 minutes of O2 plasma RIE. Photos of the resulting sample are shown in Fig. 4.21. The photo on the left side shows the front side of the sample. The circle in the middle is where the thin film is released from the sacrificial Mylar film through etching. The TiN coating is specular reflective with a yellow tone. The

photo on the right side shows the backside of the sample with CNT thin film transferred onto the TiN coated Mylar film.
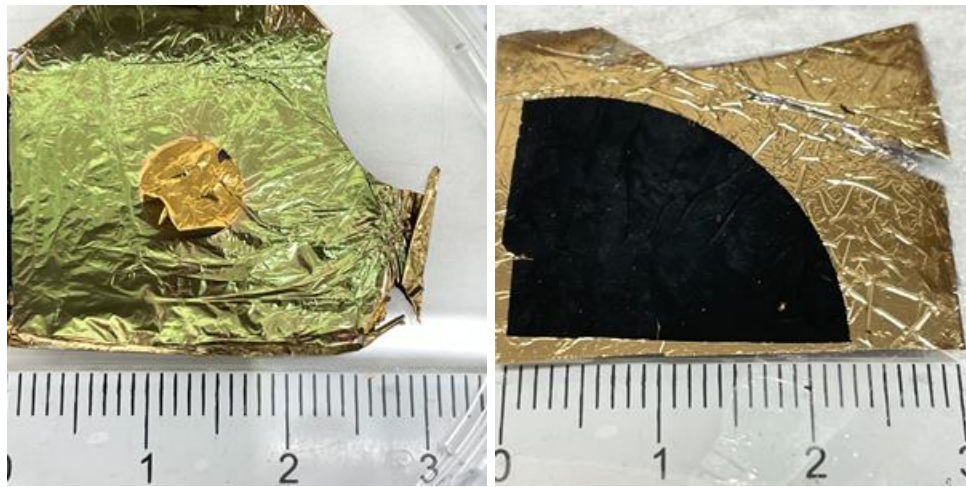
Figure 4.21 Front (left) and backside (right) of the titanium nitride coated MWCNT film.

The circle in the middle is the freestanding part.

The reflectivity of the TiN sample is measured and plotted alongside the reference sample of TiN-coated Si substrate and the theoretical curve (Fig. 4.22). The reflectivity curve aligns with the trend of the theoretical curve, albeit with some discrepancy. This difference may arise from the material data used, considering that TiN is a compound deposited by sputtering. The material data used to calculate the theoretical curve may differ from the true material properties due to variations in the Ti-to-N ratio [153].

Discrepancies between the reference sample of TiN on the Si substrate and the freestanding film result from differences in substrate material (CNT versus Si) and potential TiN degradation during plasma etching. Nevertheless, this set of results on Pt and TiN demonstrates that the reflective layer's material can be substituted with other reflective surface coatings, while maintaining specular reflective quality using the same fabrication process.
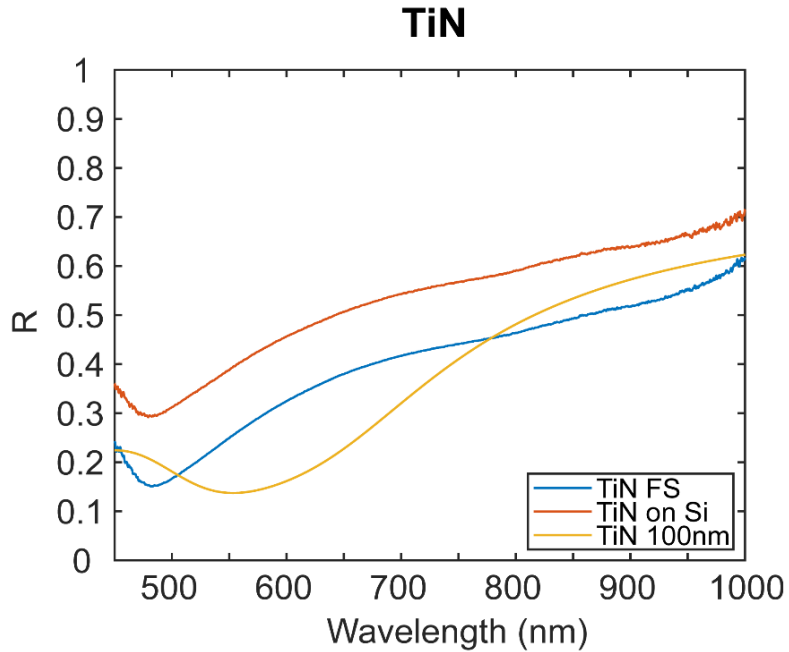
Figure 4.22 Measured reflectance of the TiN coated solar sail sample with the reference sample of TiN coated Si substrate and the theoretical curve.

4.5 Chapter conclusions

In conclusion, we outlined a fabrication process for thin film solar sail materials. The fabrication process enables creating freestanding, 1 μm thick MWCNT films with a specular reflective surface atop. Such thin films extend the operational range of solar sailing closer to the sun, enabling a conceptually new set of missions.

CHAPTER 5

Silicon Nitride Solar Sail Material Inverse Design

In the Chapter 3 we have explored a relatively simple solar sail material architectures, which were based on existing photonic design templates. In this Chapter we extend this study further and consider use of inverse design techniques to examine more efficient sail material design prototypes. In this Chapter we explore silicon nitride based photonic solar sail designs and show that inverse design techniques allow to optimize for reflectance while minimizing sail density and operating temperature. Our study shows that inverse design offers a great potential for the design of advanced solar sails.

5.1 Key trade parameters

We being our study by examining interplay of key parameters on solar sail performance. Specifically, taking solar sail exit velocity as a an objective function, we examine its dependence on the main sailcraft parameters, such as areal density and reflectivity, on solar sail velocity [58]. The expression 3.1 provides a convenient tool to conduct trade studies to understand the performance limits based on the sail material properties, sail area and spacecraft mass. We consider a square sail with two diagonal booms, on par with Lightsail 2, NEA Scout, and Solar Cruiser, as shown in Fig. 5.1.
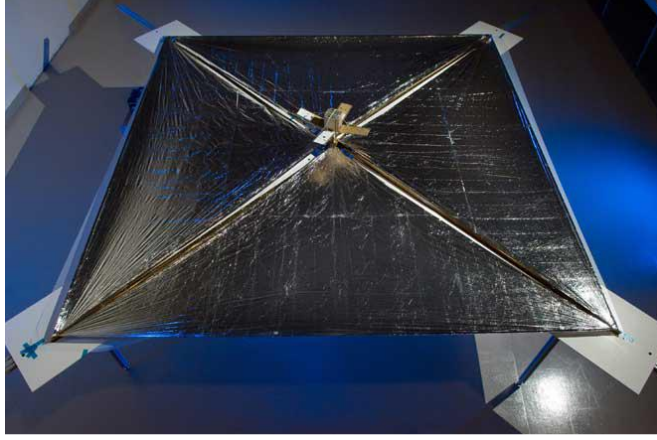
Figure 5.1 *Square solar sail. Credit: NASA/MSFC/D. Higginbotham.*

The sailcraft mass may be split into three key constituents: $m = m_s + m_{pl} + m_{supp}$, where m_s is mass of the sail material, m_{supp} is mass of the sail support (i.e., booms), and m_{pl} is the mass of the spacecraft bus that carries all key spacecraft components, such as instruments, power systems, control electronics, attitude control, communication and other systems. Boom mass may be approximated as $m_{supp} = 2\sqrt{2}\, a\rho_b$, where ρ_b is boom average linear density and a is the length of sail side (i.e., sail area $A = a_s^2$). In principle, boom linear density is not constant and is also a function of the sail area. Boom density should be chosen according to a maximum load the sail may experience, which grows for larger sail areas and smaller perihelia.

The expression for the hyperbolic excess velocity (Eq. 3.1) is then modified as:

$$\mathrm{v}_{inf} = \sqrt{-\frac{2\mu_s}{1AU + d_0} + 2(2R_s + \alpha)\frac{S_{1AU}}{c}\frac{(1AU)^2}{d_0}\frac{a_s^2}{2\sqrt{2}a\rho_b + a^2\rho_s + m_{pl}}}.$$

(5.1)

where ρ_s is the sail material areal density.

For the sake of analysis we set target velocity as 60 AU/year. In Fig. 5.1 we plot several parametric trade studies in which we analyze the exit velocity with the sail side

length by varying only one of the sailcraft parameters at a time. This study shows that the exit velocity is very susceptible to the perihelion distance (Fig. 5.2a), as expected. Reaching target of 60 AU/year requires very small perihelia (<5 R☉). The velocity is also very sensitive to sail material parameters – areal density (Fig. 5.2b) and reflectivity (Fig. 5.2c). As can be seen sail exit velocity strongly depends on the sail reflectivity, and it may be better to design higher reflectivity sail materials in expense of sail material density.
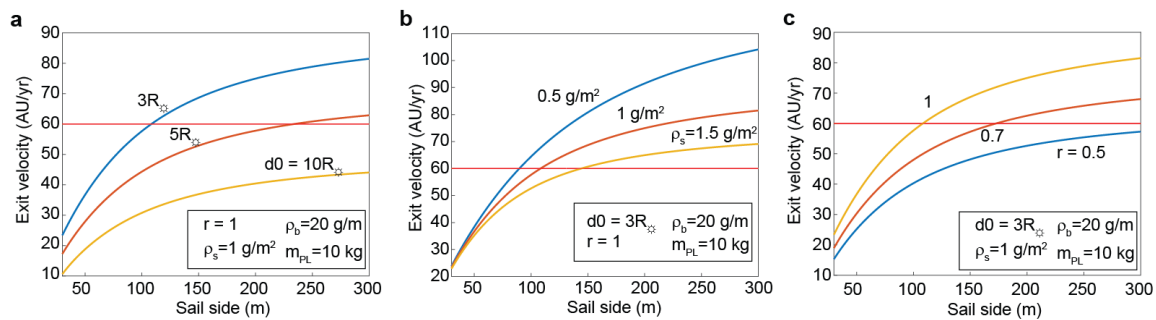
Figure 5.2 Trade studies of the exit velocity with sail area for different sail parameter variations based on equation 5.1 (a) for different perihelia for different payload masses, (b) for different sail areal densies, (c) for different sail reflectivities. Insets in each panel denote parameters that are kept fixed.

5.2 Bragg reflector and metasurface

Bragg reflectors comprised of alternating layers of high and low refractive index materials present a straightforward approach to achieving broadband reflection. Figure 5.3 plots reflectance for a 7-layer Bragg reflector constructed of alternating stacking of silicon nitride thin films and low refractive index films (refractive index~1). Such Bragg reflector reflects ~42% of the solar radiation and has an areal density of 0.97 g/m^2. Here solar reflectivity is calculated as:

110

$$R_s = \frac{\int_0^\infty R(\lambda) S_{1AU}(\lambda) d\lambda}{S_{1AU}}$$

(5.2)

where $R(\lambda)$ is the spectral reflectivity of the material.

$$R_s = \frac{\int_0^\infty R(\lambda) S_{1AU}(\lambda) d\lambda}{}$$
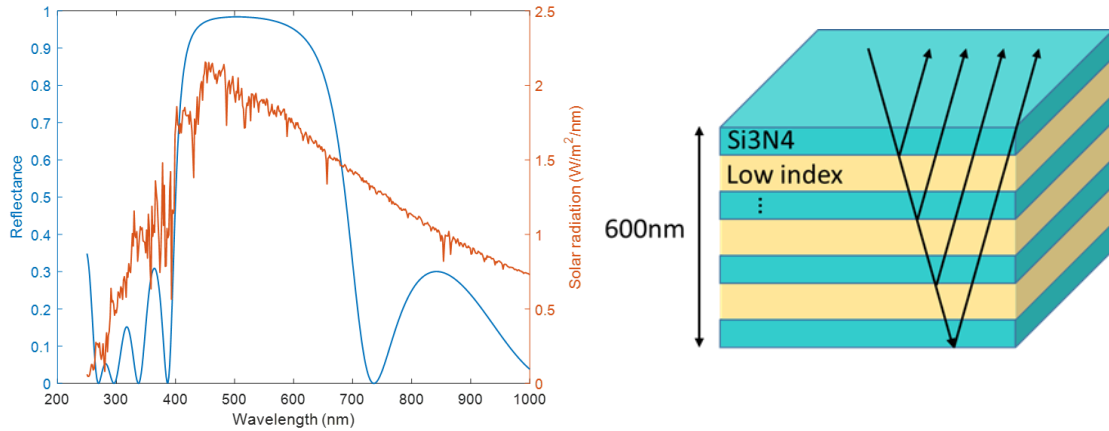
Figure 5.3 (Left) The reflection spectrum of silicon nitride Bragg reflector. Solar radiation spectrum is also show for a reference. (Right) Schematic illustration of a 7-layer Bragg reflector. The Bragg reflector is designed to a center wavelength of 500 nm. We observe a reflection band from 400~700 nm, and the tail of the solar radiation above 700 nm is not covered by the band.

Photonic metamaterials [126, 127] present another alternative to solar sail material design. Metamaterials derive their properties not from the properties of the base materials, but from the nanoscale architecture. We examine the use of metamaterials to deign solar sails out of transparent silicon nitride thin films [124, 128, 129]. Figure 5.4 shows one of the designs we have identified. The structure reflects 35% of the solar radiation, and has an areal density of 0.52 g/m^2, which is nearly half of the Bragg reflector, studied above.
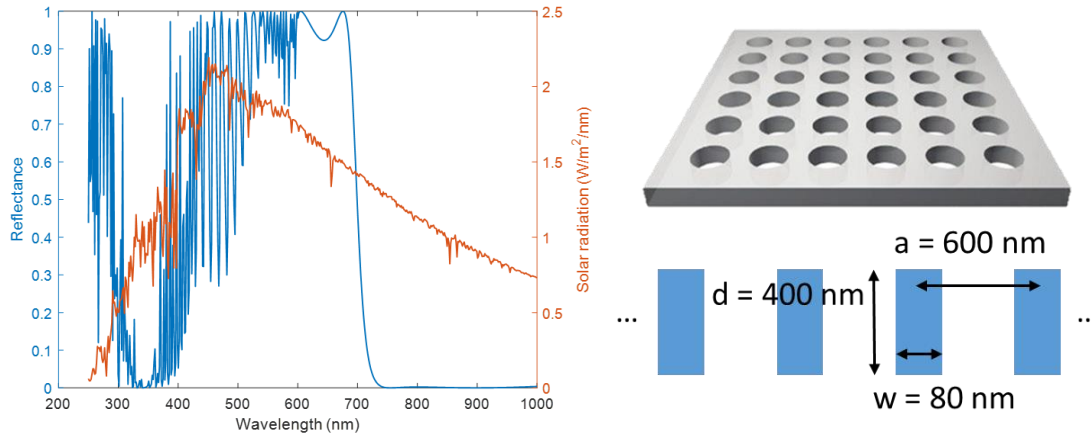
Figure 5.4 (Left) The reflection spectrum of silicon nitride metasurface reflector with the solar radiation spectrum. (Right) Schematic illustration and dimensions of the metasurface studied.

Multilayer Bragg stacks exhibit higher solar reflectivity as compared to metasurfaces, however Bragg stacks typically have higher areal density. Nevertheless, both of these simple designs fail to reach solar reflectivity of 70%, which is needed for solar sailing at 60 AU/year (see Fig. 5.2c).

The bandwidth of a Bragg reflector is insufficient to achieve a >70% solar reflection. Adding more unit cells does not significantly widen the bandwidth. To design a broadband reflector that covers a larger fraction of the solar radiation spectrum, altering the thickness of each layer in the Bragg stack. Such an approach allows getting a broader response. However, unlike the case of the periodic Bragg reflector, the parameter space for such a multilayer design is large. For this purpose to discover optimal designs we employ inverse design techniques.

113

5.3 Solar sail designs by particle swarm optimization

Computational design of micro and nanophotonic structures with desired optical responses and dispersion properties has emerged as a versatile engineering tool. It has enabled a breadth of applications from integrated optics [157, 158] and metasurfaces [31, 60, 82] to radiative cooling [158, 159] and accelerators on chip [160, 161]. Computational design relies on numerical optimization algorithms that search across a virtual space of possible geometries and materials to find designs with responses close to desired target specifications. Here, we implement particle swarm optimization (PSO) to optimize the silicon nitride multilayer stack for a solar sail material design. Particle swarm optimization (PSO) is a heuristic optimization method that is applicable to a range of computationally complex problems with multi-objective figures of merit (FOM). PSO solves a problem by having a population of candidate solutions, referred to as particles, and moving these particles around in the search-space. The movement of each particle is influenced by its locally best-known position but is also directed toward the best-known positions in the search space. These positions are continually updated as other particles discover better solutions. This dynamic is anticipated to drive the swarm towards optimal solutions [162].

In our study, we choose solar sail escape velocity (Eq. 5.1) as the figure of merit. This figure of merit, depends on sail material reflectivity, minimum perihelion distance a sail can get to, and sail material density (see also Fig. 5.2). We make use of transfer matrix method [163] to calculate sail reflectivity, absorptivity and emissivity. In addition to optical properties we track the overall density of a multilayer stack. We then iteratively modify structural properties of the system (i.e., thickness of each layer) based on particle swarm optimization algorithm to find structures that maximize the figure of merit.

114

5.4 SiN optical constants

Our solar sails designs are based on silicon nitride and therefore it is critically important to understand dispersion of its optical constants (i.e., refractive index and extinction coefficients) across a wide UV to MIR spectral band. At the same time SiN optical properties depend on the deposition technique. Low loss silicon nitride is often fabricated by LPCVD or with a high temperature annealing [164, 165]. Such SiN films possess near-stoichiometric composition. This leads to materials with high thermal stability, high refractive index, and low optical extinction. On the other hand, high loss silicon nitride films are usually fabricated by PECVD, where high temperature is not required in the process. These films are rich in Si-H and N-H bonds, which can introduce optical absorption losses across the spectrum.

The low-loss silicon nitride is beneficial for designing high-reflectivity and small solar absorptivity structures. The high-loss silicon nitride, in turn, demonstrates enhanced infrared absorption starting from ~7 µm due to a larger number of defects and dangling bonds (a related IR absorption band in the low-loss SiN is strongly red shifted). In Fig. 5.5 we plot silicon nitride refractive index (Fig. 5.5 (top)) and extinction coefficient (Fig. 5.5 (bottom)) according to several different data sources[71, 77, 166-169]. As can be seen the extinction coefficient, k, varies substantially depending on the source of data (and related methods of thin film growth). As a result one may expect strong effect of SiN optical properties on sail material performance.
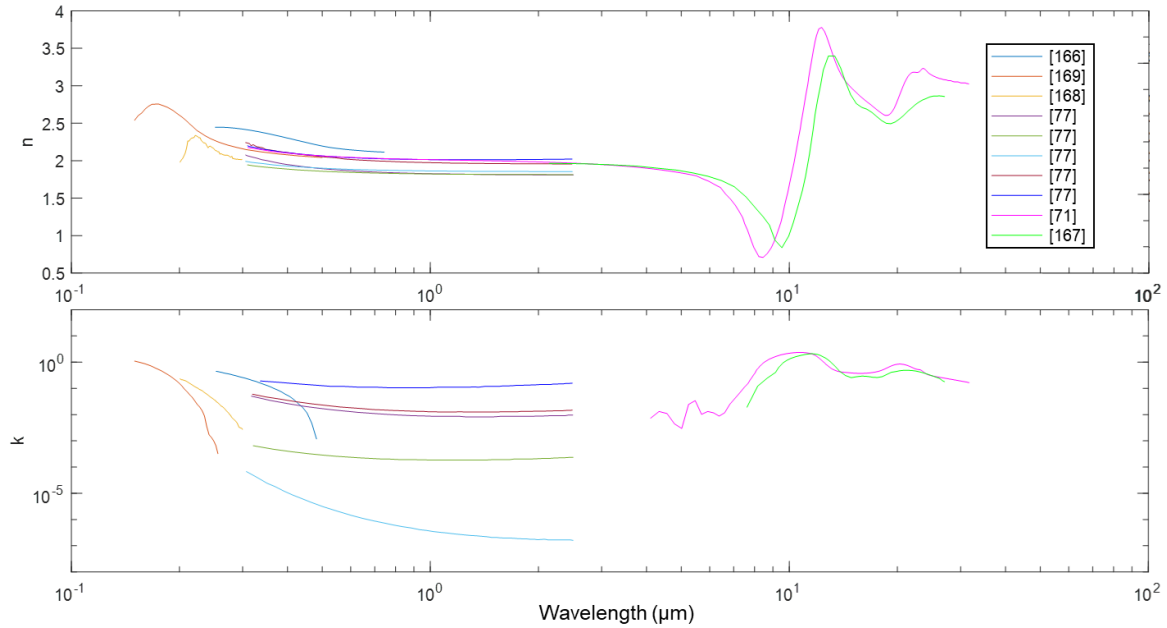
Figure 5.5 Optical constants of silicon nitride produced by different fabrication method or parameters. Real part n (top) and imaginary part k (bottom).

To assess different material properties on the sail performance and estimate the dynamics in two limiting cases, we have aggregated SiN data from different sources into one function which coves UV [169], visible [77], and IR spectral bands [71] (i.e., effectively stitching data together). This approach allows assessing limiting cases of high and low optical extinction. The resulting approximate SiN complex refractive index is plotted in figure 5.6. The high loss data has k values ~0.01 throughout most of the visible wavelength, while the low loss data has k values as low as 10^{-7}.
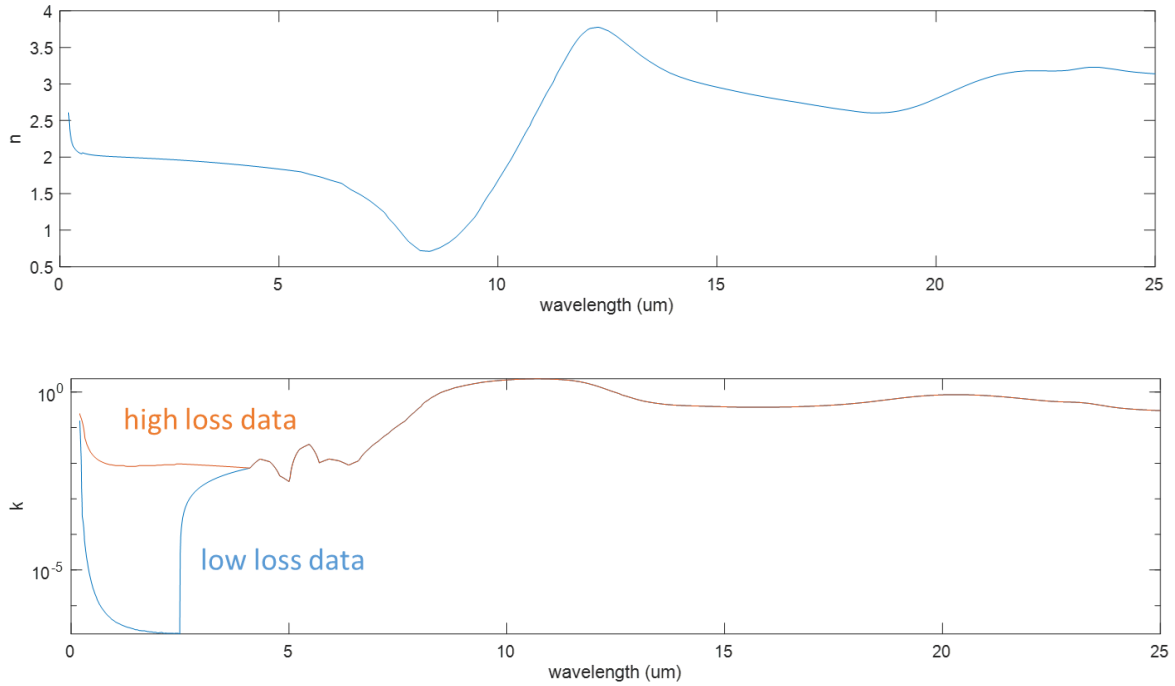
Figure 5.6 Aggregated SiN refractive index data for high loss and low loss cases. Real part n (top) and imaginary part k (bottom) are shown.

5.5 Particle Swarm Optimization of sail photonic designs

Utilizing PSO and SiN data above we study multilayer sail material optimization. In our designs we fix the number of layers and with the PSO algorithm vary their thicknesses. The result of such optimization for a low-loss silicon nitride is shown in Table 5.1. Figure 5.7 shows an example of an optimized 7-layer structure and a related reflectance spectrum.

Table 5.1 Optimization results for multilayer sails using low-loss silicon nitride data

	5 layers	7 layers	11 layers	15 layers
Reflectivity	0.5679	0.6562	0.7659	0.8357
Absorptivity	3.5438e-04	4.3566e-04	7.8678e-04	0.0013
Emissivity	0.0705	0.0949	0.1637	0.1502
Perihelion distance ($R_\odot$)	< 1	< 1	< 1	< 1
Sail temperature (K)	951.9038	929.4589 K	940.6814	1114.6
Areal density (g/m^2)	0.9494	1.4145	4.5016	6.8215

According to the table, optimization clearly shows improvement in reflectivity as compared to the Bragg reflectors. We attribute such an improvement to a wider reflectivity bans (see Fig. 5.7). Adding more layers helps improving reflectivity even further (e.g., 11-layer structures yield reflectivity as high as 70%), however, at a cost of increased areal density. For low-loss SiN, all of the designs can reach 1 $R_\odot$ and maintain a reasonable sail temperature (assuming thermal balance calculations only).
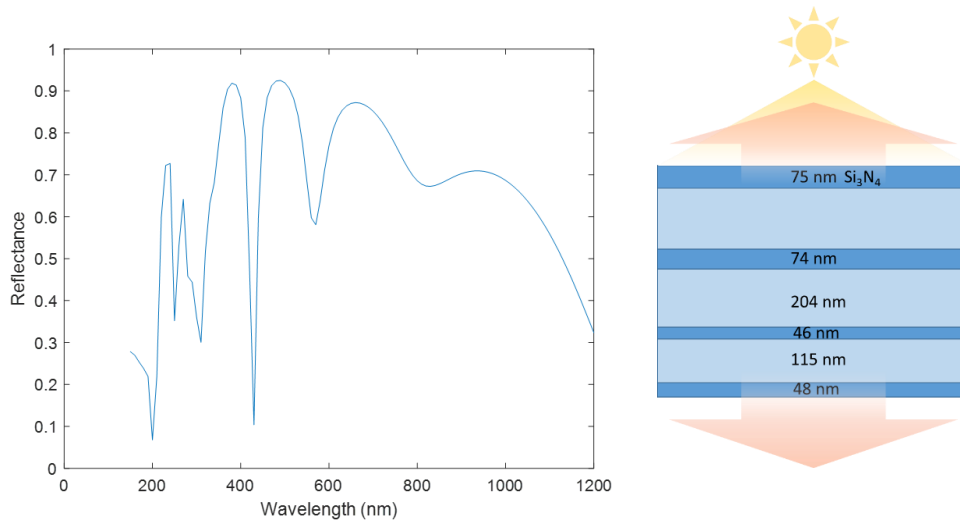
Figure 5.7 The reflectance of a 7-layer design optimized by PSO. A broad reflection band can be achieved by multilayer design.

In order to examine the worst case scenario, we conduct the same optimization process using high-loss silicon nitride data this time (see also Fig. 5.6). The results for this case are shown in Table 5.2.

Table 5.2 Optimization results for multilayer sails using high-loss silicon nitride data

	5 layers	7 layers	11 layers	15 layers
Reflectivity	0.5370	0.6048	0.7056	0.7541
Absorptivity	0.0687	0.0986	0.1021	0.1268
Emissivity	0.0354	0.0573	0.0658	0.1124
Perihelion distance ($R_\odot$)	11	11	10	9
Sail temperature (K)	2173	2173	2173	2173
Areal density (g/m^2)	0.8736	1.7461	1.7256	3.7460

For high-loss SiN structures, the minimum perihelion distances the sail can get to is significantly increased. The optimization further yields thinner structures (i.e., smaller areal density) to minimize solar absorptivity. However, thinner layers result in smaller overall solar reflectivity.

Next, we implement PSO to study metasurface designs. We start from optimizing a simple 2D grating. The structural parameters and the reflectance of an optimized structure are plotted in Fig. 5.8. The solar reflectivity is 5% higher than that obtained by parametric sweep (Fig. 5.4). Such 2D grating also possesses lower areal density.

a = 0.612 μm
d = 0.204 μm
ff = 0.508
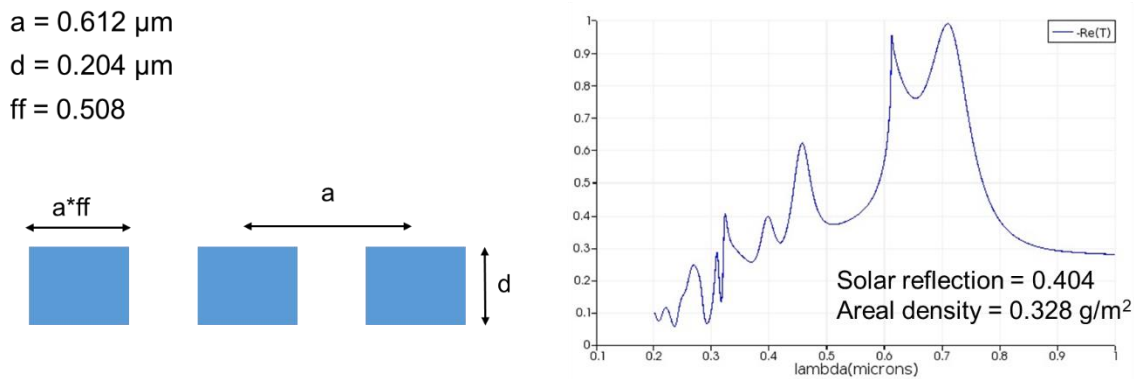
Figure 5.8 PSO results for a 2D grating structure.

We also explore other geometries (Figs. 5.9-5.11). Grating on a slab (Fig. 5.9) further improves the reflectivity to 46.7%, however at a cost of a slightly increased areal density. A multilayer grating-slab design (Fig. 5.10) allows improving both reflectrace and areal density: ~58% and $0.736\ g/m^2$, respectively. By adding another one more layer (Fig. 5.11), solar reflectivity of 62.4% is achieved with areal density <1g/m². Note that although these simulations are done in 2D with TE polarization, the designs can be generalized to 3D as well.

a = 0.668 μm
d = 0.300 μm
ff = 0.474
dg = 0.090 μm

Solar reflection = 0.467
Areal density = 0.736 g/m²
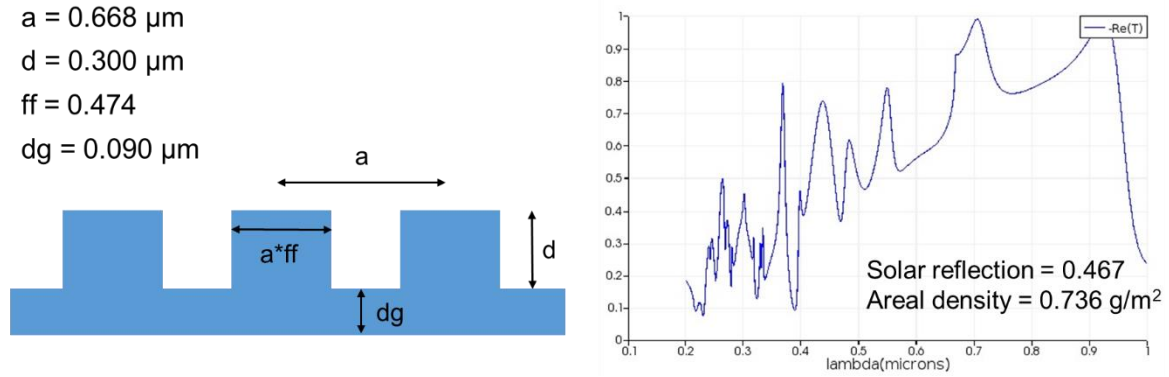
Figure 5.9 PSO results for grating on a slab.

a = 0.620 μm   d2 = 0.066 μm
d1 = 0.203 μm   dg = 0.144 μm
ff = 0.424

Solar reflection = 0.579
Areal density = 0.483 g/m²
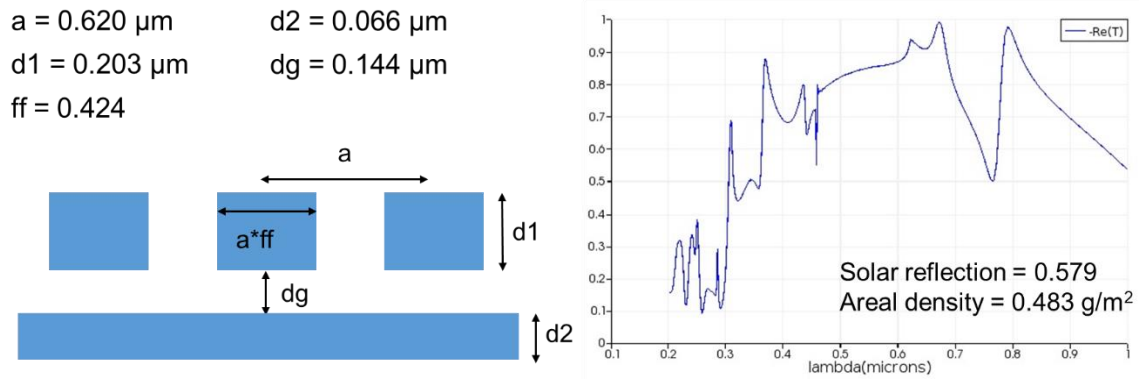
Figure 5.10 PSO results for grating on a slab with gap in between.

a = 0.659 μm   ff = 0.438   d2 = 0.056 μm
d = 0.268 μm   d1 = 0.111 μm   dg = 0.201 μm

Solar reflection = 0.624
Areal density = 0.902 g/m²
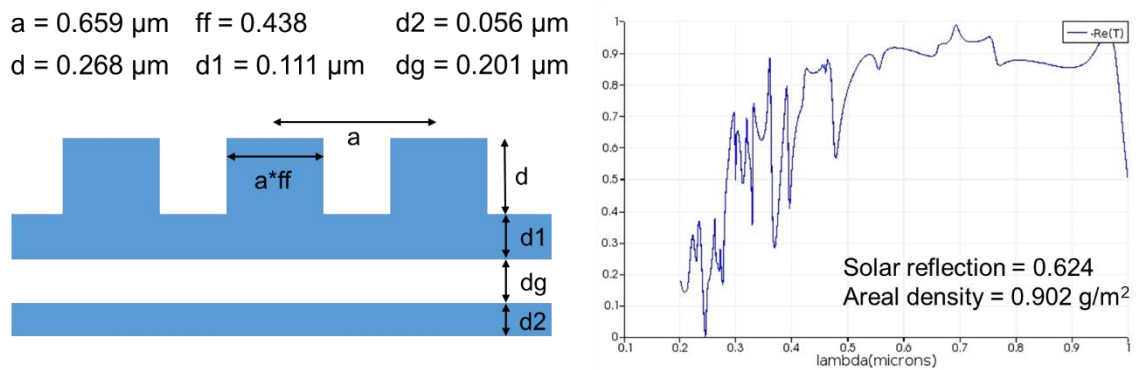
Figure 5.11 PSO results for grating on a two layer structure.

121

In order to push the limits of what can be done under this frame work, we decide to combine the metasurface design concept with the multilayers and apply PSO. Due to the large number of input variables in this design, we further separate the metasurface optimization and multilayer optimization. Specifically, for the metasurface layer, we focus on optimizing short wavelength (UV~500 nm) reflectivity, whereas for the multilayers, we focus on optimizing long wavelength (500~2000 nm) reflectivity. We then combine the optimized structures into one multilayer system. Suc hybrid design and its solar reflectivity spectrum are shown in Fig. 5.12. From this spectrum we can see how the reflection curve behaves differently below and above 500 nm. A stop band below 500 nm is created by the metasurface layer with hole pattern, and the curve above 500 nm resembles the one in Fig. 5.7. The reflection band of the multilayer stretches into the near infrared wavelength, covering the tail of the solar radiation. The solar reflectivity of the final design is 75.6%, with an areal density of 2.16 g/m^2.
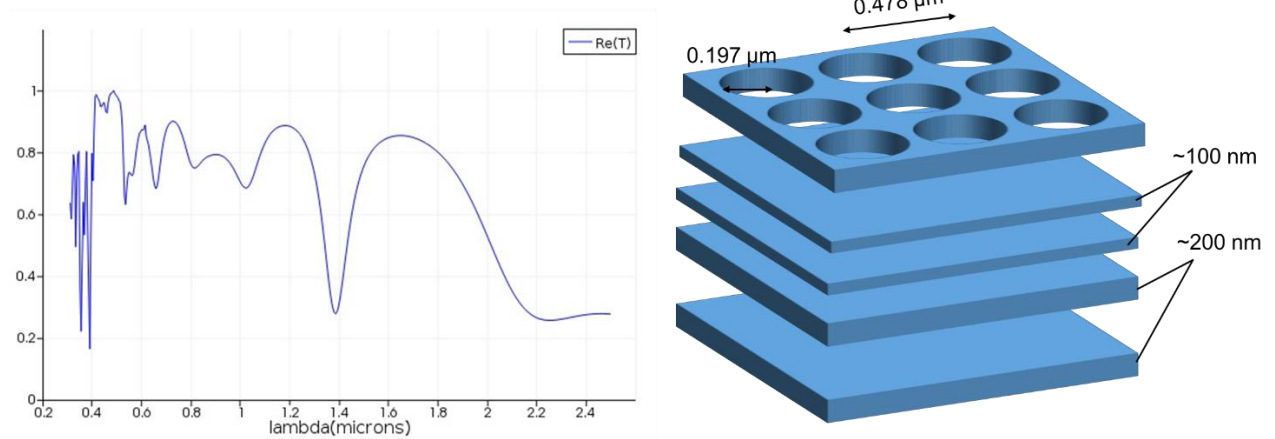
Figure 5.12 Reflectivity (left) and structural parameter (right) of the hybrid design combining metasurface layer and multilayers.

5.6 Chapter conclusions

In this Chapter we examined solar sail material photonic designs. Silicon nitride as the base material is used and the dependence of its optical properties on the overall performance is analyzed. Several design motifs are studied, including Bragg reflectors and grating reflectors. Particle swarm optimization is then used to discovers more elaborate designs with better performance metrics. Finally, a design that satisfies the requirements for extreme solar sailing is presented.

CHAPTER 6

Modeling solar corona plasma interaction with the

solar sail material

Advanced solar sailing would require flying in close proximity to the sun, where it would interact among other things with the solar wind, the density and temperature of which increase in the vicinity of the sun. Solar wind plasma may cause sputtering of surface layers, radiation enhanced sublimation, and potentially ablation [67,68]. He+ and H+ ions implantation may cause formation of nanoscale bubbles, leading to structural deformation and materials exfoliation [118, 119]. Figure 6.1 highlights some of the possible effects of sail material degradation when subject to a solar radiation environment, after Ref. [58].
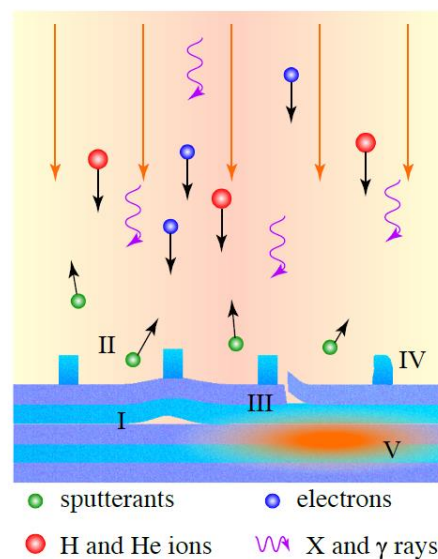
Figure 6.1 Effects of solar plasma and energetic photons and particles on solar sails in the proximity of sun : (I) formation of bubbles, (II) surface sputtering, (III) cracking, exfoliation and delamination, (IV) surface morphology deformation, and (V) energy deposition and thermos-mechanical stresses. Figure from Ref. [58].

In this Chapter, we analyze the effects of the solar wind on the solar sail materials in the vicinity of the sun. We focus on understanding solar wind sputtering and the way it may be affected by the buildup electric sheath and electron emission from the heated surface.

6.1 Solar activity close to the sun

Solar wind consists of a stream of charged particles (electrons and protons), emanating from the inner solar corona. It is known that solar wind can lead to sputtering [170, 171], therefore the influence of solar wind on thin film sail materials needs to be accounted for. For this purpose, we calculate the sputtering rate taking into account plasma sheath and secondary electron emission from the surface.

In our analysis of sputtering we make two simplifications:

1) We assume a few micron thick sail material with a 100 nm front aluminum layer. Although, as discussed previously, such a sail will not survive small perihelion flyby, we use Al to develop a generic understanding that can be extended to other materials.

2) We model the surface of the sun and the solar sail surface effectively as two electrodes. Based on solar wind data [172], the Debye length of the solar wind is found as:

$$\lambda_{\text{D}} = \sqrt{\frac{\epsilon_0 k_B T_e}{n_0 q^2}}$$

(6.1)

where ϵ_0 is the vacuum permittivity, k_B is the Boltzmann constant, T_e is the plasma temperature, n_0 is the particle density, and q is the electron charge. The Debye length for

protons in the solar wind from 2~20 $R_{\odot}$ is 0.65~2.65 m. Clearly, $\lambda_D \ll L$, where L is the distance between the sail and the solar surface.

Immersed in the solar wind plasma the sail surface would be constantly bombarded by electrons and ions causing material sputtering (Fig. 6.2). The sputtering rate depends on several conditions, including the sheath region surrounding the sail surface. It is the difference between the electrical potential between the plasma region and this sheath region that directly leads to ion bombardment of the surface.
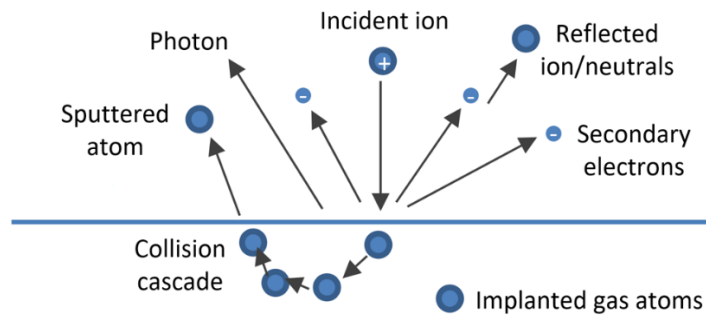
Figure 6.2 Possible phenomena for a surface bombard by high energy ions [173]. In this study we focus on sputtering.

The flux of ions and electrons is unequal due to a much higher speed of the electrons. As a result, the sail will be charged negatively with respect to solar wind plasma. This excess negative charge modifies the space charge distribution leading to sheath formation (schematically illustrated in Fig. 6.3(Left)).
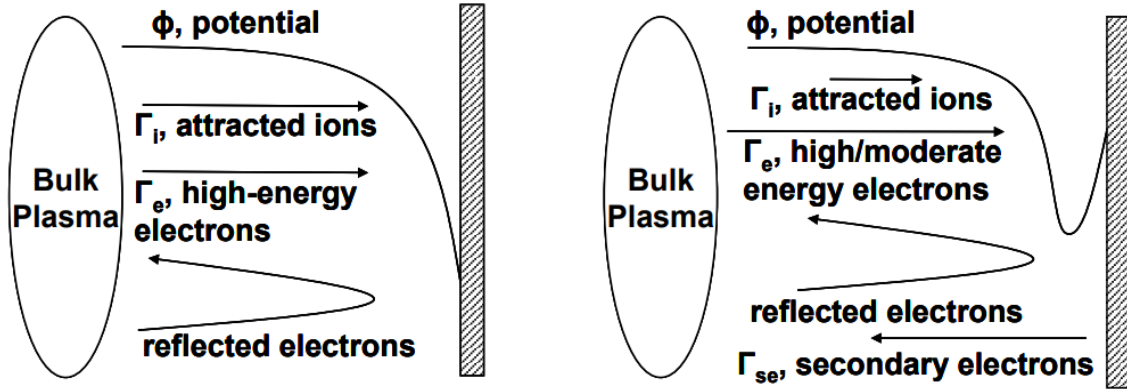
Figure 6.3 Plasma sheath profile. (Left) in the absence of secondary electrons (Right) in presence of secondary electrons. From [174].

In equilibrium, the potential held by a surface immersed in plasma environment is known as the floating potential Φ_{float}, since the potential floats to a value sufficient to maintain an equal flux of positive and negative species. We shall assume that plasma is at equipotential. This potential is termed the plasma potential Φ_{plasma}. The potential difference between the floating potential and the plasma potential $\Phi_{plasma} - \Phi_{float}$ is the sheath potential, Φ. This potential denotes the magnitude of the energy barrier which an electron must overcome in order to reach the sail. It is also the potential through which a positive ion is accelerated toward the substrate (see Fig. 6.3).

The spatial profile and extent of the sheath potential can be further modified by the emission of secondary electrons from the surface of the solar sail [175-177]. Secondary electron emission is generated when a solid surface is bombarded with charged particles (ions and electrons) and photons (Fig. 6.3(right)). Other physical processes that may cause electron emission include thermionic emission and photoelectric emission. The model is schematically illustrated in Fig. 6.4.

We shall address the following 4 questions:

1. What is the sheath potential for a solar sail in vicinity of the sun?

2. How do secondary electrons affect the sheath potential?

3. How does the temperature of the sail affect the sheath potential?

4. What is the effect of the sheath on sputtering rate?
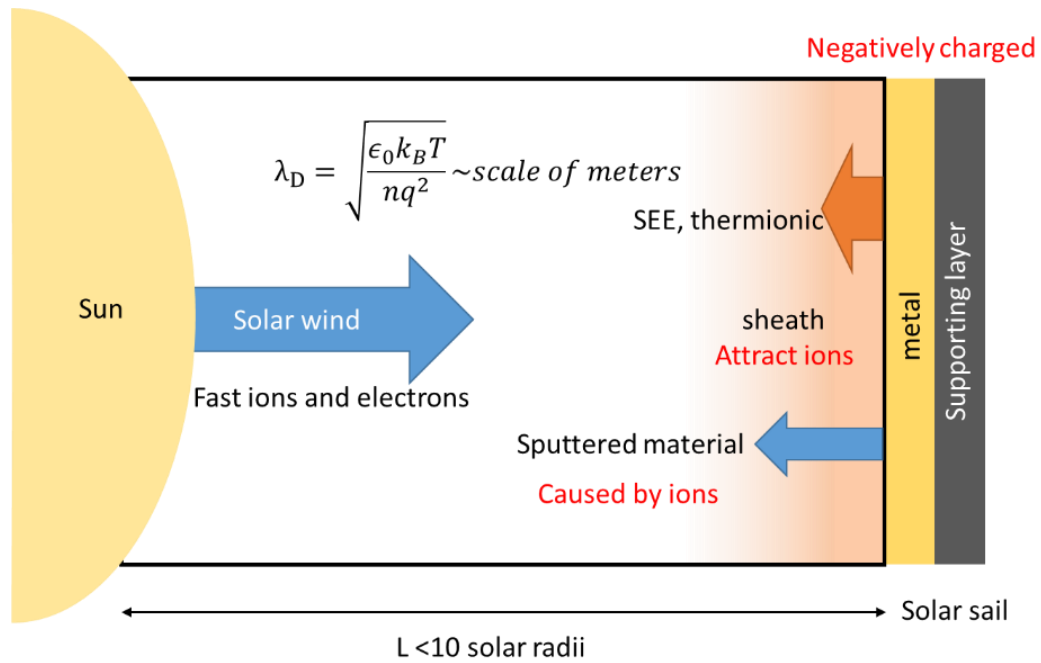
Figure 6.4 Schematic illustration of the plasma sheath model.

6.2 Modelling sheath profile

We begin our analysis with the Gauss Law:

$$\nabla \cdot E = \frac{Q}{\epsilon_0}$$

(6.2)

where E is the electric field, Q is the total charge, and ϵ_0 is the vacuum permittivity. We express the electric field as $E = -\nabla\Phi$ and model sail surface as a planar wall at $x = 0$. The sheath potential satisfies the Poisson's equation:

$$\nabla^2\Phi = \frac{d^2\Phi}{dx^2} = -\frac{Q}{\epsilon_0} = -\frac{q(n_i - n_e)}{\epsilon_0},$$

(6.3)

where the sheath potential Φ infinitely far from the wall $\Phi(\infty) = 0$, q is elementary charge, n_e and n_i are the solar wind electron and ion densities, respectively. Since the electron distribution is assumed to be Maxwellian, we use the Boltzmann equilibrium to obtain electron density. In this case the density of the plasma electrons is expressed as:

$$n_e = n_0 e^{\frac{q\phi}{k_B T_e}}$$

(6.4)

where n_0 is the equilibrium plasma density far away from the sail. To determine the potential profile, we first find the ion flux. Within the sheath, the flux of particles is conserved, thus we write:

$$n_0 u_0 = n_i u_i,$$

(6.5)

where u_0 is the velocities of ions far away from the sail and u_i is the velocity of ions in the sheath. As ions enter the sheath, they fall freely toward sail. The ion velocity at any given location within the sheath can be determined using the energy conservation:

$$\frac{1}{2}m_i u_0^2 = \frac{1}{2}m_i u_i^2 + q\Phi,$$

(6.6)

where m_i denotes ion mass. We then rewrite $u_i = \sqrt{\frac{2\left(\frac{1}{2}m_i u_0^2 - q\Phi\right)}{m_i}}$ and substitute this back into Eqs. 6.5, and obtain the following expression for ion density:

$$n_i = \frac{n_0}{\sqrt{1 - \frac{2q\Phi}{m_i u_0^2}}}$$

(6.7)

On substituting the expression of n_i and n_e into eq. 6.3 and considering the Boltzmann relationship, the condition required to satisfy the existence of sheath is $u_0 \geq \sqrt{\frac{k_B T_e}{m_i}}$ (i.e., the Bohm sheath condition). The minimum speed of ions at the edge of the sheath needs to be larger or equal to the Bohm speed $u_B = \sqrt{\frac{k_B T_e}{m_i}}$.

It is clear now that a sheath forms when a body is immersed in plasma. However, the behavior of the sheath when the object is conductive or insulating, as well as when the body is floating or has a bias can vary widely. Here we focus on the case that is closest to the solar wind and solar sail interaction, the case of floating walls. If a body, whether it is a metal or an insulator, is floating in the plasma, i.e., not electrically connected to ground or an external bias, due to lack of any conduction pathway, the electrons charge the surface instantly and the ions slowly flow towards the surface. The ions and electrons flux at the surface are equal. The charging produces a large negative potential which repels additional electrons. To find an expression for the negative sheath potential, we start with writing the expression for the flux of ions j_i and that of electron j_e

$$j_i = qn_i u_i, \qquad j_e = -q(n_0 e^{-\frac{q\Phi}{kT_e}})u_e$$

(6.8)

where $u_e = \frac{1}{4}\sqrt{\frac{8k_B T_e}{\pi m_e}}$ is the mean thermal speed of the electrons near the sail. The $\frac{1}{4}$ accounts for velocities only in the direction normal to the sail surface [178]. We can now

130

evaluate the ion current density at the sheath boundary, where $n_i = n_0$ and $u_i = u_B = $

$\sqrt{\frac{k_B T_e}{m_i}}$ (satisfies the Bohm sheath condition). The current balance at the sheath boundary

$j_i = j_e$ is then:

$$qn_0\sqrt{\frac{k_B T_e}{m_i}} = q\mathrm{n}_0 e^{-\frac{q\Phi}{kT_e}}\left(\frac{1}{4}\sqrt{\frac{8k_B T_e}{\pi m_e}}\right)$$

(6.9)

We then find the solution of the sheath potential Φ be

$$\Phi = -\frac{k_B T_e}{q}\ln\left(\sqrt{\frac{m_i}{2\pi m_e}}\right)$$

(6.10)

The effects of secondary electron emission on sheath potential have been studied in the past and are considered to be playing an important factor in determining the sheath potential [179]. Presence of secondary electrons tends to lower the sheath potential making it more positive with respect to bulk plasma. As illustrated in Fig. 6.3(b), when strong secondary electron emission happens, electrons are injected back into bulk plasma causing reduction of sheath potential. Pandey and Roy [180] derived the sheath potential in the presence of secondary electron emission and sputtering yield following the works of Hobbs and Wesson [176]. They showed that the impact of secondary electrons can be given by:

$$\Phi = -\frac{k_B T_e}{q}\ln\left((1-\Gamma)\sqrt{\frac{m_i}{2\pi m_e}}\right)$$

(6.11)

131

here Γ defines secondary electron multiplication factor (i.e., how many new electrons can be generated upon one incoming primary electron). From Eq. 6.12 it is clear that the increase of Γ decreases of the strength of sheath potential, Φ. This result is obtained without specifying the process responsible for electron emission from surface. If the electron emission originates solely from secondary electrons, Γ can be expressed as:

$$\Gamma = \Gamma_{\mathrm{e}} = \int_0^\infty \sigma(E_e) f(E_e) dE_e$$

(6.12)

where $\sigma(E_e)$ is the secondary electron yield (SEY) – a material specific coefficient, and $f(E_e)$ is the normalized velocity distribution function (VDF) of the electrons bombarding the surface. If other electron emission process are involved, Γ is redefined as[176]:

$$\Gamma = \frac{\Gamma_e + j}{1 + j},$$

(6.13)

where $j = J/n_0 (k_B T_e/m_i)^{1/2}$ and J accounts for the electron emission flux stemming from other sources. For example, in the case of thermionic emission:

$$J = D_{\mathrm{m}} A_0 T_m^2 e^{-\frac{W}{k_B T_m}},$$

(6.14)

where D_{m} is a material specific constant, $A_0 = 1.20173 \times 10^6 \, A/m^2 /K^2$, W is the work function of the metal, and T_m is the surface temperature.

6.3 Numerical simulations

First we compute the sputtering damage without taking the effects of plasma sheath into account. In our calculations of sputtering damage we use Transport of Ions In Matter

(TRIM) code [181]. The code inputs are mass, charge and energy of ions (in our case H+), and the solar sail material (Al/CNT) they interact with. Without plasma sheath, the input ion energy is determined by the solar wind temperature (assuming solar wind plasma is at a local equilibrium). Figure 6.5 shows the solar wind average temperature as the function of distance to the surface of the sun [172].
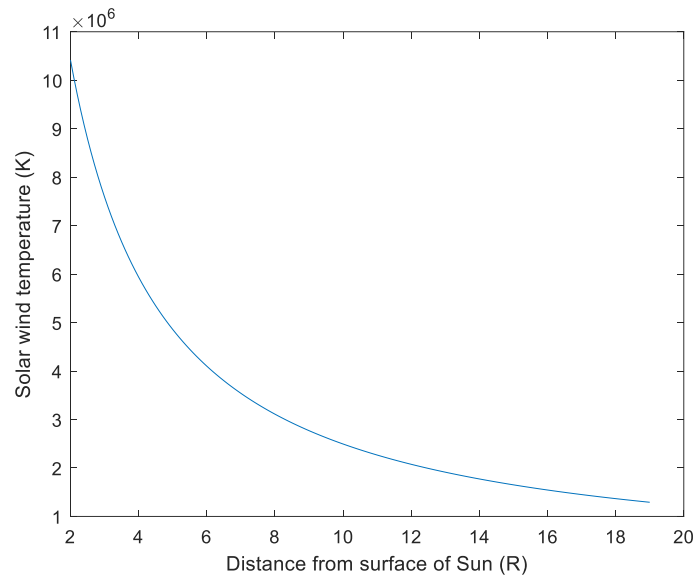
Figure 6.5 Solar wind average temperature with distance from sun.

Fig. 6.6 illustrates the simulation setup and an example result of ion-target interaction. Here we simulate 100 nm aluminum – 100 nm CNT as a prototype solar sail. Hydrogen ion are injected into the thin film with the energy calculated from the solar wind proton temperature, along with the energy gained from falling through the sheath potential. In the example in Fig. 6.6(right), the injected hydrogen ion energy is 419 eV from the solar wind proton energy at 5 $R_\odot$ without considering the sheath effect. The thin red lines indicated the trajectory of the ions once injected into the material.
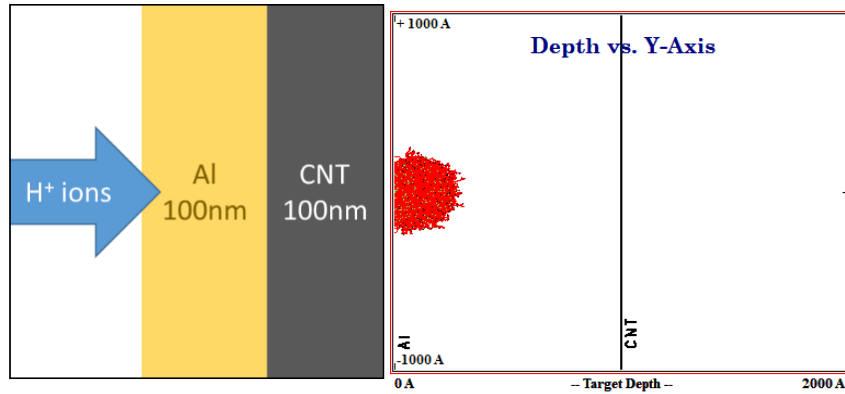
Figure 6.6 (left) diagram showing the TRIM setup (right) cross section plot of collision between ion and target material not considering sheath.

The output of the TRIM simulation is the number sputtered atoms per incident ion. We can then define the sputtering damage rate as:

$$sputtering\ damage\ \left[\frac{cm}{s}\right] = \frac{\frac{\#\ sputtered\ atoms}{\#\ incident\ ions} \times flux\ \left[\frac{\#}{cm^2 \times s}\right]}{atomic\ density\ of material\ \left[\frac{\#}{cm^3}\right]},$$

(6.15)

where solar wind flux is calculated assuming average solar wind particle velocity ~416 km/s [172]. Figure 6.7 shows the resulting sputtering damage rate as a function of distance from sun's surface. As expected, as the sail approaches the sun, due to the increase of solar wind temperature and plasma density, the sputtering damage increases.
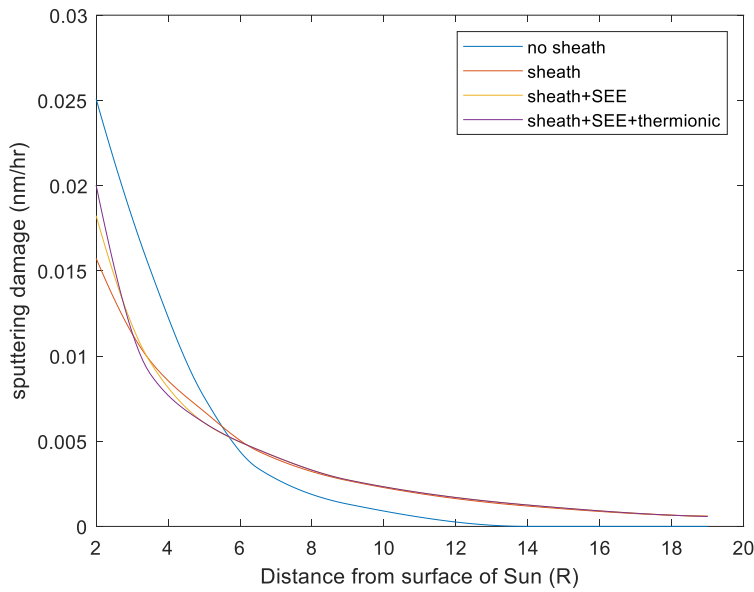
Figure 6.7 Sputtering damage rate with and without account of sheath and secondary electron emission.

Next, we calculate sputtering damage rate taking sheath potential into account. Respective sheath potential as a function of distance to the sun is shown in Fig. 6.8. When the plasma sheath potential is calculated without considering secondary electron emissions or other electron emitting at the surface of the sail, the sheath potential follows the trend of the solar wind temperature(see also Fig. 6.5). Specifically, the sheath potential decreases as the distance from the sun's surface grows. By comparing the numbers in Fig. 6.8 to the solar wind proton energies (Fig. 6.5), we see that if an ion is to fall through the sheath potential, the kinetic energy gain caused by accelerating through the sheath potential is comparable to the solar wind proton energies, and thus is unneglectable.
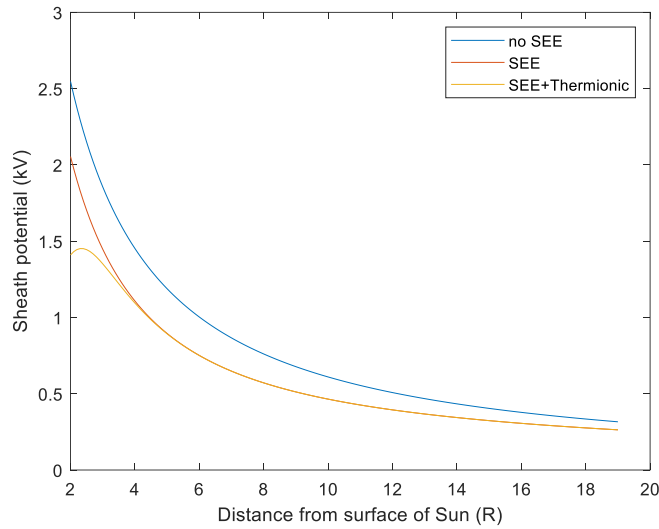
Figure 6.8 Plasma sheath potentials of no electron emission and considering electron emission from the surface of solar sail.

The plasma sheath potential with an account of secondary electron emission is also plotted in Fig. 6.8. To calculate sheath potential with secondary electron emission, we first find Γ (see Eq. 6.13). The energy distribution function in the solar wind is assumed to be Maxwellian, and the secondary electron yield can be obtained from the literature [182]. In Fig. 6.9 (top) electron emission ratio Γ as a function of distance from the sun is plotted for two cases: (1) assuming secondary electron emission and (2) assuming thermionic emission in addition to secondary electron emission. For distances >8 R☼ from the surface of the sun the difference in Γ for two different cases is negligible. The function Γ reaches maximum at ~6.5 R☼. This maximum occurs due to an interplay between the normalized velocity distribution function (VDF) of the electrons and secondary electron yield (SEY) specific to aluminum, see Fig. 6.9 (bottom). The peak of VDF shifts as the plasma temperature changes, while SEY is rather stable as the temperature changes. SEY describes the amount of secondary electrons generated per incident electron with different energies, while VDF

136

describes the distribution of electrons with certain energies. If we multiply VDF to SEY, the efficiency of secondary electron generation can be found. At low and high plasma temperatures (distance to sun = 2 R☼ and 20 R☼), the VDF peaks at energies that does not correlate well to the peak of the SEY of aluminum, indicating most of the incident electrons do not generate secondary electrons efficiently. At distance to sun = 6.5 R☼, the peak of VDF corresponds to the peak of the SEY curve, thus gives a high overall secondary electron generation, indicating a high value for Γ.

Secondary electron emission lowers the sheath potential as shown in Fig. 6.8. As the solar sail gets closer to the sun, the effect of secondary electron emission becomes more significant due to increase in plasma density.
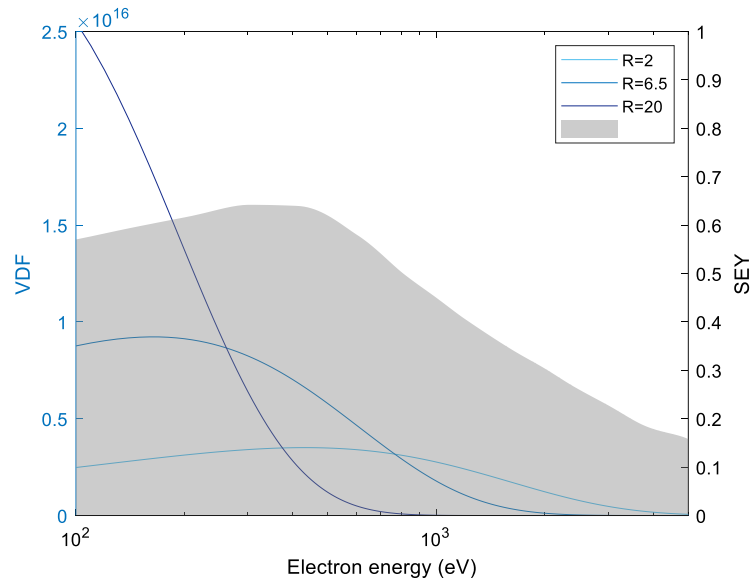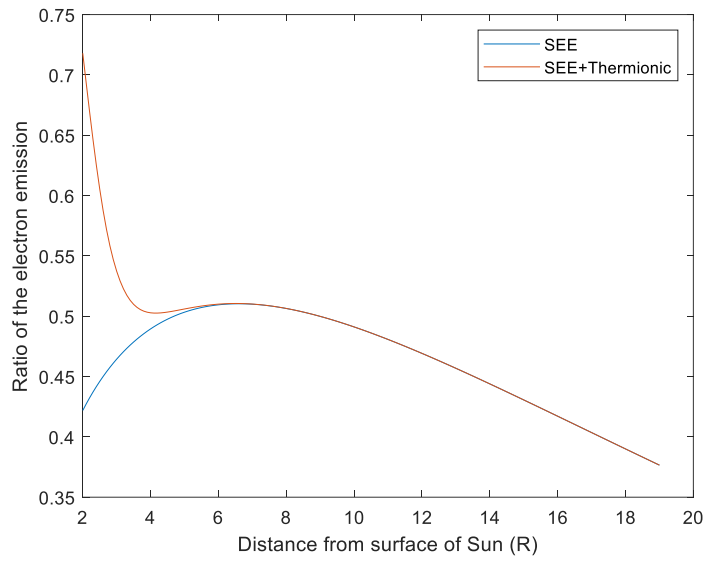
Figure 6.9 (top) Γ considering secondary electron emission and thermionic electron emission plotted with distance to sun. (bottom) The peak of the VDF correlates the best with SEY of aluminum at 6.5 R☼ from the sun. The lines in blue shades are the VDFs of electron at 2 R☼, 6.5 R☼, and 20 R☼ from the sun. The shaded curve is the SEY for aluminum.

Thermionic emission is another source of electron emission that can affect the sheath potential. When solar sail flies close to the sun, high sail material temperature is inevitable as a result of the absorption of solar radiation. Calculated sail temperature as a function of distance from the sun is shown in Fig. 6.10 (assuming unity backside emissivity). Aluminum has a melting point of ~960 K and will not survive close solar flybys. However for the sake analysis and developing a framework here we ignore the melting temperature. We examine the influence of thermionic electron emission. Due to the lack of data on aluminum material dependent correction coefficient D_m in Eq. 6.15, we set $D_m = 0.5$ (for comparison tungsten has $D_m = 0.75$ and tantalum has $D_m = 0.35$). With the use of Eq. 6.13, 6.14. and 6.15 we calculate Γ as a function of distance from the sun, Fig. 6.9 (top). Evidently in close proximity to the sun Γ factor accounting for thermionic emission in addition to secondary electron emission, deviates significantly from Γ accounting only for secondary electrons for close solar approaches, at distances < 6 R☼. At these distances the sail material temperature >1900 K signifying that thermionic emission plays an important role. Due to thermionic electron emission factor Γ dramatically increases at distances below 4 R☼. The effect of thermionic emission on sheath potential, Φ, is shown in Fig. 6.8. The thermionic electron mission dominating at <4 R☼ reduces the sheath potential. As a result, proton acceleration is reduced.
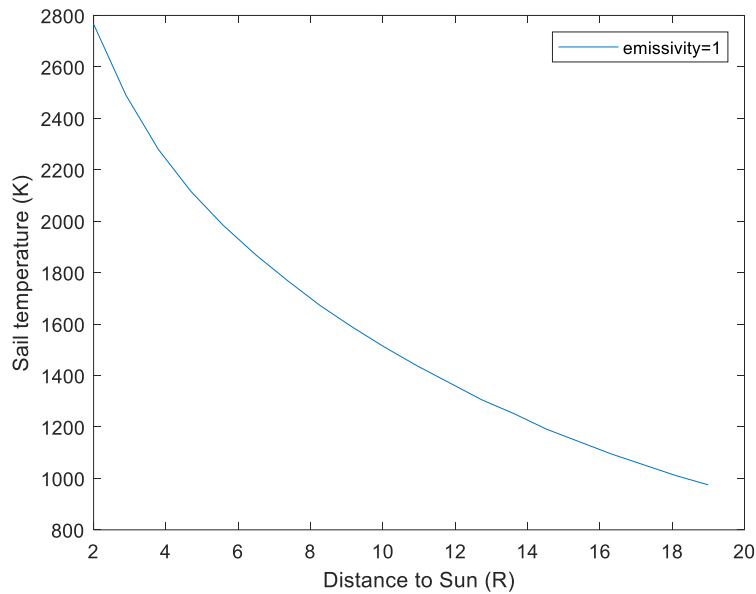
Figure 6.10 Solar sail equilibrium temperature in the vicinity of sun. The sun facing side is assumed to be aluminum and the backside emission is assumed to be unity.

Once the sheath potential is established (see Fig. 6.7) we can estimate the kinetic energy that solar wind ions gain while falling through the sheath as $q\Phi$. This energy adds to the average kinetic energy of ions in solar wind. We then modify TRIM calculations to examine effects of increased ion energy on materials sputtering. We compare sputtering damage rate with and without the account of plasma sheath (see Fig. 6.7). For large distances from the sun due to a lower thermal ion energy the key contributor to sputtering is sheath potential ion acceleration. Notably, sputtering damage rate is not necessarily proportional to ion energy. High energy ions penetrate deep into the material and interact with the atoms far away from the surface. In this cases atoms cannot escape the surface, and implantation instead of sputtering occurs. This effect is clearly seen in Fig. 6.7. While plasma sheath increases the ion injection energy, for close solar approaches a lower sputtering damage rate is observed when compared to a case without sheath.

In Fig. 6.10, we provide an example TRIM simulation result considering plasma sheath with SEE and thermionic emission from the sail surface at 3.5 R☼ from the sun. The ions penetrates deeper into the solar sail comparing to Fig. 6.5(right) as the ion injection energy increase. Deep ion penetration yields relatively small sputtering rate of ~0.02 nm/hr. For small durations of sail material exposure (<1 week) sputtering is not expected to cause any substantial damage. However, such deep ion penetration may result in other sail material damaging effects not considered here.
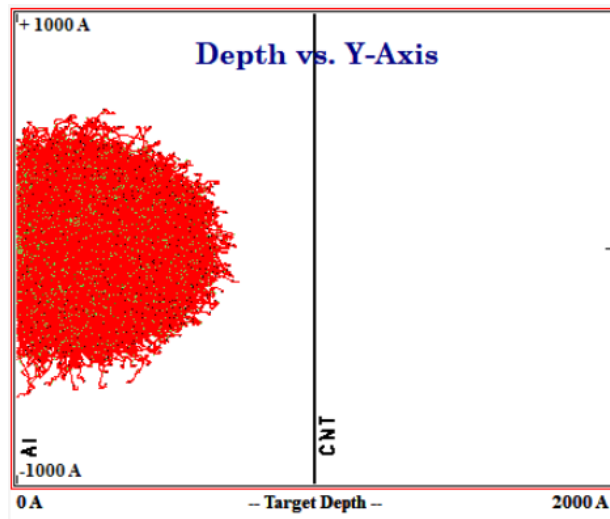
Figure 6.11 Ion collision cross section considering acceleration from plasma sheath at 3.5 R☼ from the sun.

6.4 Chapter conclusion

In this Chapter we have examined the effects of sputtering of solar sail materials by the solar wind as a function of distance from the sun. In our analysis we have also taken into account of sail charging and built up plasma sheath near the sail surface. As shown the sheath changes solar wind ion acceleration and modifies the sputtering rate. Effects of

secondary electron emission and thermionic electron emissions are studied. Our calculations predict sputtering rate of ~0.02 nm/hr at 2 R$_\odot$ from the sun. For extreme solar sailing with active propulsion near the sun of <1 week, such a rate of sputtering will have minor effects on sail material performance. However, other effects such as surface roughness, ion implantation, blistering may need to be studied in detail. Compared to previous simulating the charging of Solar Parker Probe, our estimates of the sheath potential are about 2 orders of magnitude larger [183]. Future study would need to develop more detailed models to account for effects beyond the ones we have discussed in this Chapter.

CHAPTER 7

Conclusion

Efficient propulsion systems for space travel hold the promise of revolutionizing space exploration by making it more scalable and cost-effective. One particularly promising candidate for this role is radiation pressure propulsion. Technological advancements in lightweight materials have transformed the initial concept into a feasible idea. This dissertation delves into the exploration of two types of radiation pressure propulsion: laser-driven propulsion and extreme solar sailing.

In the case of laser sailing, the dissertation investigates the operational principles for Earth orbital maneuvering. Lightweight spacecraft, driven by lasers, exhibit the capability to execute maneuvers that are traditionally challenging for conventional chemical and electrical propulsion systems. Transfers between low Earth and geostationary orbits, as well as 90° plane change maneuvers, can be achieved within a few hours using a 1MW laser beam or in a day with a lower laser power. The design of spacecraft lightsails is guided by radiative thermal balance, achievable through the careful selection of materials, such as silicon nitride and boron nitride, along with nanophotonic engineering. These designs achieve absorptivity to emissivity ratios in the range of 10^{-5} to 10^{-3}, providing near unity reflectivity and ultralight areal density.

Extreme solar sailing is another approach for fast transit space exploration that is discussed in this dissertation. To push the limit of solar sailing, we explored solar sailing within 3~5 $R_{\odot}$ to <0.2 AU of the sun and examined sail materials that can potentially withstand such an extreme environment. Materials that can withstand the high solar

irradiance in the vicinity of the sun are surveyed. We have suggested two design approaches: first one is the two-layer design using TiN as the reflective layer and CNT as the supportive material, and the second one using silicon nitride with nanophotonic design. For the first approach we developed a new fabrication process to create TiN/CNT thin film freestanding materials. A freestanding solar sail sample is fabricated and characterized. The sail sample survives 450°C thermal cycling, while preserving optically smooth reflection. Plasma damage on this type of sail is simulated with sputtering estimated to be 0.02 nm/hr 2 R$_\odot$ from the sun. For the silicon nitride solar sails, we examined strategies for nanophotonic inverse design. Metasurface and multilayer designs are explored, and the structures with 75% solar reflectivity and 2 g/m^2 areal density are obtained.

This dissertation shows that principles of nanophotonic engineering can be used to create a next generation of advanced space systems for future breakthrough space exploration. Meticulously designed optical nanostructures powered by photon pressure may one day get to far reaches of space.

BIBLIOGRAPHY

[1]   S. Bolton *et al.*, "The juno mission," *Space Science Reviews,* vol. 213, no. 1, pp. 5-37, 2017.

[2]   E. National Academies of Sciences and Medicine, "Origins, worlds, and life: a decadal strategy for planetary science and astrobiology 2023-2032," 2022.

[3]   P. Liewer, R. Mewaldt, J. Ayon, C. Garner, S. Gavit, and R. Wallace, "Interstellar probe using a solar sail: Conceptual design and technological challenges," in *COSPAR Colloquia Series*, 2001, vol. 11, pp. 411-420.

[4]   S. G. Turyshev *et al.*, "Direct multipixel imaging and spectroscopy of an exoplanet with a solar gravity lens mission," *arXiv preprint arXiv:2002.11871,* 2020.

[5]   A. M. Long, M. G. Richards, and D. E. Hastings, "On-orbit servicing: a new value proposition for satellite design and operation," *Journal of Spacecraft and Rockets,* vol. 44, no. 4, pp. 964-976, 2007.

[6]   J. S. Hudson and D. Kolosa, "Versatile On-Orbit Servicing Mission Design in Geosynchronous Earth Orbit," *Journal of Spacecraft and Rockets,* pp. 1-7, 2020.

[7]   N. Sánchez-Ortiz, M. Belló-Mora, and H. Klinkrad, "Collision avoidance manoeuvres during spacecraft mission lifetime: Risk reduction and required δv," *Advances in Space Research,* vol. 38, no. 9, pp. 2107-2116, 2006.

[8]   C. Bonnal, J.-M. Ruault, and M.-C. Desjean, "Active debris removal: Recent progress and current trends," *Acta Astronautica,* vol. 85, pp. 51-60, 2013.

[9]   J. Pollard, "Evaluation of low-thrust orbital maneuvers," in *34th AIAA/ASME/SAE/ASEE Joint Propulsion Conference and Exhibit*, 1998, p. 3486.

[10]   B. M. Kiforenko, Z. V. Pasechnik, and I. Y. Vasil'ev, "Comparison of the rocket engines efficiency in the case of low thrust orbit-to-orbit transfers," *Acta Astronautica,* vol. 60, no. 10-11, pp. 801-809, 2007.

[11]   H. R. Kaufman and R. S. Robinson, "Electric thruster performance for orbit raising and maneuvering," *Journal of Spacecraft and Rockets,* vol. 21, no. 2, pp. 180-186, 1984.

[12]   G. P. Sutton and O. Biblarz, *Rocket propulsion elements*. John Wiley & Sons, 2016.

[13]   M. D. Rayman and D. H. Lehman, "Deep space one: Nasa's first deep-space technology validation mission," *Acta Astronautica,* vol. 41, no. 4-10, pp. 289-299, 1997.

[14]   A. A. Siddiqi, *Beyond Earth: A Chronicle of Deep Space Exploration, 1958-2016*. National Aeronautics and Space Administration, Office of Communications …, 2018.

[15]   A. Tenneti, G. Hampika, V. Rohit, and M. Guduri, "Interstellar Space Travel Using Nuclear Propulsion," in *Energy Systems, Drives and Automations*: Springer, 2020, pp. 331-338.

[16]   G. Vulpetti, "Antimatter propulsion for space exploration," *Journal of the British Interplanetary Society,* vol. 39, no. 9, pp. 391-409, 1986.

[17]   G. Matloff and H. Gerrish, "The scale of the problem: Interstellar distances, time, and energy considerations," in *Interstellar Travel*: Elsevier, 2023, pp. 51-82.

[18]   JAXA, "https://global.jaxa.jp/projects/sas/ikaros/."

[19]   B. Starshot, "https://breakthroughinitiatives.org/initiative/3."

[20]   K. L. Parkin, "The breakthrough starshot system model," *Acta Astronautica,* vol. 152, pp. 370-384, 2018.

[21]   G. Marx, "Interstellar vehicle propelled by terrestrial laser beam," *Nature,* vol. 211, no. 5044, pp. 22-23, 1966.

[22]   J. Redding, "Interstellar vehicle propelled by terrestrial laser beam," *Nature,* vol. 213, no. 5076, pp. 588-589, 1967.

[23]   H. A. Atwater *et al.*, "Materials challenges for the Starshot lightsail," *Nature materials,* vol. 17, no. 10, pp. 861-867, 2018.

[24]   G. A. Landis, "Optics and materials considerations for a laser-propelled lightsail," presented at the the 40th International Astronautical Federation Congress, Malaga, Spain, October 7-12, 1989.

[25]   P. Lubin, "A roadmap to interstellar flight," *arXiv preprint arXiv:1604.01356,* 2016.

[26]   R. L. Forward, "Roundtrip interstellar travel using laser-pushed lightsails," *Journal of Spacecraft and Rockets,* vol. 21, no. 2, pp. 187-195, 1984.

[27]   M. G. Millis, J. Greason, and R. Stevenson, "Breakthrough Propulsion Study: Assessing Interstellar Flight Challenges and Prospects," 2018.

[28]   J. T. Kare, "SailBeam: Space propulsion by macroscopic sail-type projectiles," in *AIP Conference Proceedings*, 2001, vol. 552, no. 1: American Institute of Physics, pp. 402-406.

[29]   K. F. Long, *Deep space propulsion: a roadmap to interstellar flight*. Springer, 2012.

[30]   G. Anglada-Escudé *et al.*, "A terrestrial planet candidate in a temperate orbit around Proxima Centauri," *Nature,* vol. 536, no. 7617, pp. 437-440, 2016.

[31]   W. Jin, W. Li, M. Orenstein, and S. Fan, "Inverse design of lightweight broadband reflector for relativistic lightsail propulsion," *ACS Photonics,* vol. 7, no. 9, pp. 2350-2355, 2020.

[32]   O. Ilic, C. M. Went, and H. A. Atwater, "Nanophotonic heterostructures for efficient propulsion and radiative cooling of relativistic light sails," *Nano letters,* vol. 18, no. 9, pp. 5583-5589, 2018.

[33]   B. Cheetham, T. Gardner, A. Forsman, E. Kayser, and M. Clarkson, "CAPSTONE: a unique CubeSat platform for a navigation demonstration in cislunar space," in *ASCEND 2022*, 2022, p. 4382.

[34]   J. Schoolcraft, A. Klesh, and T. Werne, "MarCO: interplanetary mission development on a CubeSat scale," *Space Operations: Contributions from the Global Community,* pp. 221-231, 2017.

[35]   "https://www.alliedmarketresearch.com/cubesat-market-A09399."

[36]   Z. Manchester, M. Peck, and A. Filo, "Kicksat: A crowd-funded mission to demonstrate the world's smallest spacecraft," in *27th Annual AIAA/USU Conference on Small Satellites*, Manchester, 2013.

[37]   G. Curzi, D. Modenini, and P. Tortora, "Large constellations of small satellites: A survey of near future challenges and missions," *Aerospace,* vol. 7, no. 9, p. 133, 2020.

[38]   D. Krejci and P. Lozano, "Space propulsion technology for small spacecraft," *Proceedings of the IEEE,* vol. 106, no. 3, pp. 362-378, 2018.

[39]   T. Wekerle, J. B. Pessoa, L. E. V. L. d. Costa, and L. G. Trabasso, "Status and trends of smallsats and their launch vehicles—An up-to-date review," *Journal of Aerospace Technology and Management,* vol. 9, pp. 269-286, 2017.

[40]   K. Hibbard, L. Glaze, and J. Prince, "Aerobraking at Venus: A science and technology enabler," *Acta Astronautica,* vol. 73, pp. 137-143, 2012.

[41]   R. Saunders *et al.*, "Magellan mission summary," *Journal of Geophysical Research: Planets,* vol. 97, no. E8, pp. 13067-13090, 1992.

[42]   J. Brophy, C. Garner, B. Nakazono, M. Marcucci, M. Henry, and D. Noon, "The ion propulsion system for Dawn," in *39th AIAA/ASME/SAE/ASEE Joint Propulsion Conference and Exhibit*, 2003, p. 4542.

[43]   P. E. Nielsen, "Effects of directed energy weapons," NATIONAL DEFENSE UNIV WASHINGTON DC CENTER FOR TECHNOLOGY AND NATIONAL …, 1994.

[44]   I. G. Observatory, "https://noirlab.edu/public/programs/gemini-observatory/."

[45]   M. M. Salary and H. Mosallaei, "Photonic Metasurfaces as Relativistic Light Sails for Doppler-Broadened Stable Beam-Riding and Radiative Cooling," *Laser & Photonics Reviews,* vol. 14, no. 8, p. 1900311, 2020.

[46]   Y. A. Rezunkov, *High Power Laser Propulsion*. Springer, 2021.

[47]   L. Felicetti and F. Santoni, "Nanosatellite swarm missions in low Earth orbit using laser propulsion," *Aerospace Science and Technology,* vol. 27, no. 1, pp. 179-187, 2013.

[48]   J. H. Lee and E. J. Conway, "Power laser beaming and applications in space," *Le Journal de Physique IV,* vol. 1, no. C7, pp. C7-715-C7-719, 1991.

[49]   H. D. Curtis, *Orbital mechanics for engineering students*. Amsterdam: Elsevier Butterworth Heinemann, 2019.

[50]   D. A. Vallado, *Fundamentals of astrodynamics and applications*. New York: McGraw-Hill Companies, Inc., 2001.

[51]   A. A. Siddiqi and R. Launius, *Deep space chronicle: A chronology of deep space and planetary probes 1958-2000*. Washington, DC United States: NASA Headquarters, 2002.

[52]   A. Witze, "Pluto fly-by: a graphical guide to the historic mission," *Nature News,* vol. 523, no. 7559, p. 140, 2015.

[53]   J. H. Mauldin, "Prospects for Interstellar Travel," *NASA STI/Recon Technical Report A,* vol. 93, p. 25710, 1992.

[54]   E. Stone, "The voyagers," *Nature Astronomy,* vol. 1, no. 12, pp. 896-896, 2017.

[55]   S. E. Wailliez, "On Lambert's problem and the elliptic time of flight equation: A simple semi-analytical inversion method," *Advances in Space Research,* vol. 53, no. 5, pp. 890-898, 2014.

[56]   D. Garber *et al.*, "A Fast Response Mission to Rendezvous with an Interstellar Object," *arXiv preprint arXiv:2106.14319,* 2021.

[57]   P. R. Srivastava, A. Majumdar, R. Menon, and G. A. Swartzlander Jr, "High Forward Thrust Metasurface Beam-Riding Sail," *arXiv preprint arXiv:2303.06793,* 2023.

[58]   A. R. Davoyan, J. N. Munday, N. Tabiryan, G. A. Swartzlander, and L. Johnson, "Photonic materials for interstellar solar sailing," *Optica,* vol. 8, no. 5, pp. 722-734, 2021.

[59]   G. A. Swartzlander, "Radiation pressure on a diffractive sailcraft," *JOSA B,* vol. 34, no. 6, pp. C25-C30, 2017.

[60]   M. M. Salary and H. Mosallaei, "Inverse Design of Diffractive Relativistic Meta-Sails via Multi-Objective Optimization," *Advanced Theory and Simulations,* vol. 4, no. 6, p. 2100047, 2021.

[61]   J. Brewer *et al.*, "Thermo-accelerative optimization of relativistic lightsails," *arXiv preprint arXiv:2106.03558,* 2021.

[62]   D. J. Barnhart, T. Vladimirova, A. M. Baker, and M. N. Sweeting, "A low-cost femtosatellite to enable distributed space missions," *Acta Astronautica,* vol. 64, no. 11-12, pp. 1123-1143, 2009.

[63]   K. Sun *et al.*, "Metasurface optical solar reflectors using AZO transparent conducting oxides for radiative cooling of spacecraft," *Acs Photonics,* vol. 5, no. 2, pp. 495-501, 2018.

[64]   W. Li and S. Fan, "Nanophotonic control of thermal radiation for energy applications," *Opt. Express,* vol. 26, no. 12, pp. 15995-16021, 2018.

[65]   D. G. Baranov, Y. Xiao, I. A. Nechepurenko, A. Krasnok, A. Alù, and M. A. Kats, "Nanophotonic engineering of far-field thermal emitters," *Nature materials,* vol. 18, no. 9, pp. 920-930, 2019.

[66]   A. Howes, J. R. Nolen, J. D. Caldwell, and J. Valentine, "Near-Unity and Narrowband Thermal Emissivity in Balanced Dielectric Metasurfaces," *Advanced Optical Materials,* vol. 8, no. 4, p. 1901470, 2020.

[67]   A. P. Raman, M. Abou Anoma, L. Zhu, E. Rephaeli, and S. Fan, "Passive radiative cooling below ambient air temperature under direct sunlight," *Nature,* vol. 515, no. 7528, pp. 540-544, 2014.

[68]   K. Sun *et al.*, "VO2 thermochromic metamaterial-based smart optical solar reflector," *ACS photonics,* vol. 5, no. 6, pp. 2280-2286, 2018.

[69]   C. Jauregui, J. Limpert, and A. Tünnermann, "High-power fibre lasers," *Nature photonics,* vol. 7, no. 11, pp. 861-867, 2013.

[70]   A. Arbabi, Y. Horie, M. Bagheri, and A. Faraon, "Dielectric metasurfaces for complete control of phase and polarization with subwavelength spatial resolution and high transmission," *Nature nanotechnology,* vol. 10, no. 11, pp. 937-943, 2015.

[71]   K. Luke, Y. Okawachi, M. R. Lamont, A. L. Gaeta, and M. Lipson, "Broadband mid-infrared frequency comb generation in a Si 3 N 4 microresonator," *Optics letters,* vol. 40, no. 21, pp. 4823-4826, 2015.

[72]   J. Kischkat *et al.*, "Mid-infrared optical properties of thin films of aluminum oxide, titanium dioxide, silicon dioxide, aluminum nitride, and silicon nitride," *Applied optics,* vol. 51, no. 28, pp. 6789-6798, 2012.

[73]   P. Tai Lin, V. Singh, L. Kimerling, and A. Murthy Agarwal, "Planar silicon nitride mid-infrared devices," *Applied physics letters,* vol. 102, no. 25, p. 251121, 2013.

[74]   J. D. Caldwell *et al.*, "Sub-diffractional volume-confined polaritons in the natural hyperbolic material hexagonal boron nitride," *Nature communications,* vol. 5, no. 1, pp. 1-9, 2014.

[75]   Z. Jacob, "Hyperbolic phonon–polaritons," *Nature materials,* vol. 13, no. 12, pp. 1081-1083, 2014.

[76]   X. G. Xu *et al.*, "Mid-infrared polaritonic coupling between boron nitride nanotubes and graphene," *ACS nano,* vol. 8, no. 11, pp. 11305-11312, 2014.

[77]   R. Kou *et al.*, "Spectrometric analysis of silicon nitride films deposited by low-temperature liquid-source CVD," *Journal of Applied Physics,* vol. 126, no. 13, p. 133101, 2019, doi: 10.1063/1.5114675.

[78]   M. H. Pfeiffer, J. Liu, A. S. Raja, T. Morais, B. Ghadiani, and T. J. Kippenberg, "Ultra-smooth silicon nitride waveguides based on the Damascene reflow process: fabrication and loss origins," *Optica,* vol. 5, no. 7, pp. 884-892, 2018.

[79]   S. Wang and R. Magnusson, "Theory and applications of guided-mode resonance filters," *Applied optics,* vol. 32, no. 14, pp. 2606-2613, 1993.

[80]   P. Moitra *et al.*, "Large-scale all-dielectric metamaterial perfect reflectors," *Acs Photonics,* vol. 2, no. 6, pp. 692-698, 2015.

[81]   J. P. Moura, R. A. Norte, J. Guo, C. Schäfermeier, and S. Gröblacher, "Centimeter-scale suspended photonic crystal mirrors," *Opt. Express,* vol. 26, no. 2, pp. 1895-1909, 2018.

[82]   S. Molesky, Z. Lin, A. Y. Piggott, W. Jin, J. Vucković, and A. W. Rodriguez, "Inverse design in nanophotonics," *Nature Photonics,* vol. 12, no. 11, pp. 659-670, 2018.

[83]   K. A. Obrey and R. K. Schulze, "Ultra-thin Aerogel Films," *Los Alamos National Lab,* 2012.

[84]   C. Lin *et al.*, "Nanocardboard as a nanoscale analog of hollow sandwich plates," *Nature Communications,* vol. 9, no. 1, p. 4442, 2018/10/25 2018, doi: 10.1038/s41467-018-06818-6.

[85]   H. Huang *et al.*, "Determination of mechanical properties of PECVD silicon nitride thin films for tunable MEMS Fabry–Perot optical filters," *Journal of Micromechanics and Microengineering,* vol. 15, no. 3, p. 608, 2005.

[86]   R. DiPippo, *Geothermal Power Plants: Principles, Applications, Case Studies and Environmental Impact*. Elsevier Science, 2011.

[87]   A. Kaushik, H. Kahn, and A. H. Heuer, "Wafer-level mechanical characterization of silicon nitride MEMS," *Journal of Microelectromechanical Systems,* vol. 14, no. 2, pp. 359-367, 2005.

[88]   B. Fu, E. Sperber, and F. Eke, "Solar sail technology—a state of the art review," *Progress in Aerospace Sciences,* vol. 86, pp. 1-19, 2016.

[89]   L. Johnson, "Solar sails for spacecraft propulsion," 2016.

[90]   L. Johnson, R. Young, E. Montgomery, and D. Alhorn, "Status of solar sail technology within NASA," *Advances in Space Research,* vol. 48, no. 11, pp. 1687-1694, 2011.

[91]   G. Vulpetti, L. Johnson, and G. L. Matloff, *Solar sails: a novel approach to interplanetary travel.* Springer, 2014.

[92]   L. Johnson, R. M. Young, and E. E. Montgomery IV, "Status of solar sail propulsion: moving toward an interstellar probe," in *AIP Conference Proceedings*, 2007, vol. 886, no. 1: American Institute of Physics, pp. 207-214.

[93]   F. Gámez Losada and J. Heiligers, "New solar-sail orbits for polar observation of the Earth and Moon," *Journal of Guidance, Control, and Dynamics,* vol. 44, no. 12, pp. 2155-2171, 2021.

[94]   C. R. McInnes, "Solar sail mission applications for non-Keplerian orbits," *Acta Astronautica,* vol. 45, no. 4-9, pp. 567-575, 1999.

[95]   G. Aliasi, G. Mengali, and A. A. Quarta, "Artificial Lagrange points for solar sail with electrochromic material panels," *Journal of Guidance, Control, and Dynamics,* vol. 36, no. 5, pp. 1544-1550, 2013.

[96] C. L. Johnson, A. F. Heaton, F. M. Curran, and R. Dissly, "The solar cruiser mission: demonstrating large solar sails for deep space missions," in *International Astronautical Congress*, 2019, no. MSFC-E-DAA-TN74364.

[97] Y. Tsuda *et al.*, "Flight status of IKAROS deep space solar sail demonstrator," *Acta astronautica,* vol. 69, no. 9-10, pp. 833-840, 2011.

[98] L. Johnson, M. Whorton, A. Heaton, R. Pinson, G. Laue, and C. Adams, "NanoSail-D: A solar sail demonstration mission," *Acta astronautica,* vol. 68, no. 5-6, pp. 571-575, 2011.

[99] D. A. Spencer, B. Betts, J. M. Bellardo, A. Diaz, B. Plante, and J. R. Mansell, "The LightSail 2 solar sailing technology demonstration," *Advances in Space Research,* 2020.

[100] F. Meinardi, F. Bruni, and S. Brovelli, "Luminescent solar concentrators for building-integrated photovoltaics," *Nature Reviews Materials,* vol. 2, no. 12, pp. 1-9, 2017.

[101] T. Chujo, H. Ishida, O. Mori, and J. Kawaguchi, "Liquid crystal device with microstructure for attitude control of spacecraft by solar radiation pressure," in *2018 Space Flight Mechanics Meeting*, 2018, p. 0964.

[102] B. E. Goldstein *et al.*, "Solar Polar Sail mission: report of a study to put a scientific spacecraft in a circular polar orbit about the sun," in *Missions to the Sun II*, 1998, vol. 3442: SPIE, pp. 65-76.

[103] C. Sauer, "Solar sail trajectories for solar polar and interstellar probe missions," 1999.

[104] J. Szalay *et al.*, "The near-sun dust environment: initial observations from parker solar probe," *The Astrophysical Journal Supplement Series,* vol. 246, no. 2, p. 27, 2020.

[105] M. Macdonald, G. W. Hughes, C. R. McInnes, A. Lyngvi, P. Falkner, and A. Atzei, "Solar polar orbiter: a solar sail technology reference study," *Journal of Spacecraft and Rockets,* vol. 43, no. 5, pp. 960-972, 2006.

[106] "https://blogs.nasa.gov/parkersolarprobe/2020/09/25/parker-solar-probe-speeds-toward-record-setting-close-approach-to-the-sun/." (accessed.

[107] G. L. Matloff, "Graphene, the ultimate interstellar solar sail material," *Journal of the British Interplanetary Society,* vol. 65, pp. 378-381, 2012.

[108] G. A. Landis, "Advanced Solar-and Laser-pushed Lightsail Concepts," 1999.

[109] R. Y. Kezerashvili and G. L. Matloff, "Solar radiation and the beryllium hollow-body sail: 2. Diffusion, recombination and erosion processes," *Journal of the British Interplanetary Society,* vol. 61, no. 2, pp. 47-57, 2008.

[110] E. Ancona and R. Y. Kezerashvili, "Extrasolar space exploration by a solar sail accelerated via thermal desorption of coating," *Advances in Space Research,* vol. 63, no. 7, pp. 2021-2034, 2019.

[111]   L. McNutt, L. Johnson, P. Kahn, J. Castillo-Rogez, and A. Frick, "Near-earth asteroid (NEA) scout," in *AIAA Space 2014 Conference and Exposition*, 2014, p. 4435.

[112] K. Kobayashi *et al.*, "The high inclination solar mission," *arXiv preprint arXiv:2006.03111,* 2020.

[113] O. Mori *et al.*, "Overview of IKAROS mission," *Advances in solar sailing,* pp. 25-43, 2014.

[114] G. V. Naik, J. L. Schroeder, X. Ni, A. V. Kildishev, T. D. Sands, and A. Boltasseva, "Titanium nitride as a plasmonic material for visible and near-infrared wavelengths," *Opt. Mater. Express,* vol. 2, no. 4, pp. 478-489, 2012.

[115]   L. H. Li and Y. Chen, "Atomically thin boron nitride: unique properties and applications," *Advanced Functional Materials,* vol. 26, no. 16, pp. 2594-2608, 2016.

[116]   D. Golberg *et al.*, "Boron nitride nanotubes and nanosheets," *ACS nano,* vol. 4, no. 6, pp. 2979-2993, 2010.

[117]   K. S. Novoselov, D. V. Andreeva, W. Ren, and G. Shan, "Graphene and other two-dimensional materials," *Frontiers of Physics,* vol. 14, pp. 1-4, 2019.

[118]   A. C. Neto and K. Novoselov, "New directions in science and technology: two-dimensional crystals," *Reports on Progress in Physics,* vol. 74, no. 8, p. 082501, 2011.

[119]   S. Park, M. Vosguerichian, and Z. Bao, "A review of fabrication and applications of carbon nanotube film-based flexible electronics," *Nanoscale,* vol. 5, no. 5, pp. 1727-1752, 2013.

[120]   A. C. Ferrari *et al.*, "Science and technology roadmap for graphene, related two-dimensional crystals, and hybrid systems," *Nanoscale,* vol. 7, no. 11, pp. 4598-4810, 2015.

[121]   Z. Wu *et al.*, "Transparent, conductive carbon nanotube films," *Science,* vol. 305, no. 5688, pp. 1273-1276, 2004.

[122]   K. S. Novoselov *et al.*, "Two-dimensional atomic crystals," *Proceedings of the National Academy of Sciences,* vol. 102, no. 30, pp. 10451-10453, 2005.

[123]   A. Naqavi *et al.*, "Extremely broadband ultralight thermally-emissive optical coatings," *Opt. Express,* vol. 26, no. 14, pp. 18545-18562, 2018.

[124]   N. Yu and F. Capasso, "Flat optics with designer metasurfaces," *Nature materials,* vol. 13, no. 2, pp. 139-150, 2014.

[125] C. J. Chang-Hasnain and W. Yang, "High-contrast gratings for integrated optoelectronics," *Advances in Optics and Photonics,* vol. 4, no. 3, pp. 379-440, 2012.

[126]   Y. Liu and X. Zhang, "Metamaterials: a new frontier of science and technology," *Chemical Society Reviews,* vol. 40, no. 5, pp. 2494-2507, 2011.

[127]   N. Engheta and R. W. Ziolkowski, *Metamaterials: physics and engineering explorations*. John Wiley & Sons, 2006.

[128]   S. M. Kamali, E. Arbabi, A. Arbabi, and A. Faraon, "A review of dielectric optical metasurfaces for wavefront control," *Nanophotonics,* vol. 7, no. 6, pp. 1041-1068, 2018.

[129]   A. Zhan, S. Colburn, R. Trivedi, T. K. Fryett, C. M. Dodson, and A. Majumdar, "Low-contrast dielectric metasurface optics," *ACS photonics,* vol. 3, no. 2, pp. 209-214, 2016.

[130]   K. Debnath, T. D. Bucio, A. Al-Attili, A. Z. Khokhar, S. Saito, and F. Y. Gardes, "Photonic crystal waveguides on silicon rich nitride platform," *Opt. Express,* vol. 25, no. 4, pp. 3214-3221, 2017.

[131]   C. m. specifications, "http://www.nexolvematerials.com/low-cure-polyimides/cp1-polyimide.."

[132]   K. E. Drexler, "Design of a high performance solar sail system," Massachusetts Institute of Technology, 1979.

[133]   T. Tsuneyoshi, Y. Yohaze, T. Watanabe, and T. Ono, "Free-Standing Metal Films Prepared via Electroless Plating at Liquid–Liquid Interfaces," *Langmuir,* vol. 34, no. 44, pp. 13183-13191, 2018.

[134]   L. Dai, F. An, J. Zou, X. Zhong, and G. Zhong, "Freestanding inorganic oxide films for flexible electronics," *Journal of Applied Physics,* vol. 132, no. 7, 2022.

[135]   X. Peng, J. Jin, E. M. Ericsson, and I. Ichinose, "General method for ultrathin free-standing films of nanofibrous composite materials," *Journal of the American Chemical Society,* vol. 129, no. 27, pp. 8625-8633, 2007.

[136]   Y. Kato, A. Sekiguchi, K. Kobashi, R. Sundaram, T. Yamada, and K. Hata, "Mechanically robust free-standing single-walled carbon nanotube thin films with uniform mesh-structure by blade coating," *Frontiers in Materials,* vol. 7, p. 562455, 2020.

[137]   K. Mizuno *et al.*, "A black body absorber from vertically aligned single-walled carbon nanotubes," *Proceedings of the National Academy of Sciences,* vol. 106, no. 15, pp. 6044-6047, 2009.

[138]   P. Liu *et al.*, "Continuous carbon nanotube-based fibers and films for applications requiring enhanced heat dissipation," *ACS applied materials & interfaces,* vol. 8, no. 27, pp. 17461-17471, 2016.

[139]   Y. Sun *et al.*, "Large-scale multifunctional carbon nanotube thin film as effective mid-infrared radiation modulator with long-term stability," *Advanced Optical Materials,* vol. 9, no. 3, p. 2001216, 2021.

[140]   J. Hansson *et al.*, "Effects of high temperature treatment of carbon nanotube arrays on graphite: increased crystallinity, anchoring and inter-tube bonding," *Nanotechnology,* vol. 31, no. 45, p. 455708, 2020.

[141]   Y. Kim, H. Muramatsu, T. Hayashi, M. Endo, M. Terrones, and M. Dresselhaus, "Thermal stability and structural changes of double-walled carbon nanotubes by heat treatment," *Chemical Physics Letters,* vol. 398, no. 1-3, pp. 87-92, 2004.

[142] K. Metenier *et al.*, "Coalescence of single-walled carbon nanotubes and formation of multi-walled carbon nanotubes under high-temperature treatments," *Carbon,* vol. 40, no. 10, pp. 1765-1773, 2002.

[143] B. Yoo, Z. Xu, and F. Ding, "How single-walled carbon nanotubes are transformed into multiwalled carbon nanotubes during heat treatment," *ACS omega,* vol. 6, no. 5, pp. 4074-4079, 2021.

[144] V. J. Gokhale, O. A. Shenderova, G. E. McGuire, and M. Rais-Zadeh, "Infrared absorption properties of carbon nanotube/nanodiamond based thin film coatings," *Journal of Microelectromechanical Systems,* vol. 23, no. 1, pp. 191-197, 2013.

[145] J. H. Lehman, C. Engtrakul, T. Gennett, and A. C. Dillon, "Single-wall carbon nanotube coating on a pyroelectric detector," *Applied Optics,* vol. 44, no. 4, pp. 483-488, 2005.

[146] Z. Shi, X. Chen, X. Wang, T. Zhang, and J. Jin, "Fabrication of Superstrong Ultrathin Free-Standing Single-Walled Carbon Nanotube Films via a Wet Process," *Advanced Functional Materials,* vol. 21, no. 22, pp. 4358-4363, 2011.

[147] E. Shkondin, T. Repän, O. Takayama, and A. Lavrinenko, "High aspect ratio titanium nitride trench structures as plasmonic biosensor," *Opt. Mater. Express,* vol. 7, no. 11, pp. 4171-4182, 2017.

[148] W. S. Werner, K. Glantschnig, and C. Ambrosch-Draxl, "Optical constants and inelastic electron-scattering data for 17 elemental metals," *Journal of Physical and Chemical Reference Data,* vol. 38, no. 4, pp. 1013-1092, 2009.

[149] K. M. McPeak *et al.*, "Plasmonic films can easily be better: rules and recipes," *ACS photonics,* vol. 2, no. 3, pp. 326-333, 2015.

[150]   I. Sengupta, S. Chakraborty, M. Talukdar, S. K. Pal, and S. Chakraborty, "Thermal reduction of graphene oxide: How temperature influences purity," *Journal of Materials Research,* vol. 33, no. 23, pp. 4113-4122, 2018.

[151]   C.-H. Tsou *et al.*, "Effect of microstructure of graphene oxide fabricated through different self-assembly techniques on 1-butanol dehydration," *Journal of Membrane Science,* vol. 477, pp. 93-100, 2015.

[152]   W.-S. Hung *et al.*, "Pressure-assisted self-assembly technique for fabricating composite membranes consisting of highly ordered selective laminate layers of amphiphilic graphene oxide," *Carbon,* vol. 68, pp. 670-677, 2014.

[153]   S. Bose and L. T. Drzal, "Role of thickness and intercalated water in the facile reduction of graphene oxide employing camera flash," *Nanotechnology,* vol. 25, no. 7, p. 075702, 2014.

[154]   J. E. Cha, S. Y. Kim, and S. H. Lee, "Effect of continuous multi-walled carbon nanotubes on thermal and mechanical properties of flexible composite film," *Nanomaterials,* vol. 6, no. 10, p. 182, 2016.

[155]   L.-C. Lin and J. C. Grossman, "Atomistic understandings of reduced graphene oxide as an ultrathin-film nanoporous membrane for separations," *Nature Communications,* vol. 6, no. 1, p. 8335, 2015/09/23 2015, doi: 10.1038/ncomms9335.

[156]   K. Marszałek, N. Wolska, and J. Jaglarz, "Angle resolved scattering combined with optical profilometry as tools in thin films and surface survey," *Acta Physica Polonica A,* vol. 128, no. 1, pp. 81-86, 2015.

[157]   M. H. Tahersima *et al.*, "Deep neural network inverse design of integrated photonic power splitters," *Scientific reports,* vol. 9, no. 1, p. 1368, 2019.

[158]   M. M. Salary and H. Mosallaei, "Inverse design of radiative thermal meta-sources via discrete dipole approximation model," *Journal of Applied Physics,* vol. 125, no. 16, 2019.

[159]   Y. Shi, W. Li, A. Raman, and S. Fan, "Optimization of multilayer optical films with a memetic algorithm and mixed integer programming," *Acs Photonics,* vol. 5, no. 3, pp. 684-691, 2017.

[160]   T. Hughes, G. Veronis, K. P. Wootton, R. J. England, and S. Fan, "Method for computationally efficient design of dielectric laser accelerator structures," *Opt. Express,* vol. 25, no. 13, pp. 15414-15427, 2017.

[161]   N. V. Sapra *et al.*, "On-chip integrated laser-driven particle accelerator," *Science,* vol. 367, no. 6473, pp. 79-83, 2020.

[162]   M. R. Bonyadi and Z. Michalewicz, "Particle swarm optimization for single objective continuous space problems: a review," *Evolutionary computation,* vol. 25, no. 1, pp. 1-54, 2017.

[163]   K. Pascoe, "Reflectivity and transmissivity through layered, lossy media," *A user-friendly approach,* 2012.

[164]   C. Yang and J. Pham, "Characteristic study of silicon nitride films deposited by LPCVD and PECVD," *Silicon,* vol. 10, pp. 2561-2567, 2018.

[165]   L. Y. Beliaev, E. Shkondin, A. V. Lavrinenko, and O. Takayama, "Optical, structural and composition properties of silicon nitride films deposited by reactive radio-frequency sputtering, low pressure and plasma-enhanced chemical vapor deposition," *Thin Solid Films,* vol. 763, p. 139568, 2022.

[166]   M. Ghaderi and R. F. Wolffenbuttel, "Design and fabrication of ultrathin silicon-nitride membranes for use in UV-visible airgap-based MEMS optical filters," in *Journal of Physics: Conference Series*, 2016, vol. 757, no. 1: IOP Publishing, p. 012032.

[167]   S. A. Alterovitz, G. H. Bu-Abbud, J. A. Woollam, and D. C. Liu, "An enhanced sensitivity null ellipsometry technique for studying films on substrates: Application to silicon nitride on gallium arsenide," *Journal of Applied Physics,* vol. 54, no. 3, pp. 1559-1569, 1983.

[168]   F. Chang and G. Kino, "Nitrogen-rich silicon nitride thin films for deep-ultraviolet Mirau interferometry," *Optics letters,* vol. 22, no. 8, pp. 492-494, 1997.

[169]   H. R. Philipp, "Optical properties of silicon nitride," *Journal of the Electrochemical Society,* vol. 120, no. 2, p. 295, 1973.

[170]   P. Wurz *et al.*, "Solar wind sputtering of dust on the surface of 67P/Churyumov-Gerasimenko," *Astronomy & Astrophysics,* vol. 583, p. A22, 2015.

[171]   G. Wehner, C. Kenknight, and D. Rosenberg, "Sputtering rates under solar-wind bombardment," *Planetary and Space Science,* vol. 11, no. 8, pp. 885-895, 1963.

[172]   M. Venzmer and V. Bothmer, "Solar-wind predictions for the Parker Solar Probe orbit-Near-Sun extrapolations derived from an empirical solar-wind model based on Helios and OMNI observations," *Astronomy & Astrophysics,* vol. 611, p. A36, 2018.

[173]   "https://www.plasmaquest.co.uk/the-technology/sputtering-basics/." (accessed.

[174]   R. Shastry, "Experimental characterization of the near-wall region in Hall thrusters and its implications on performance and lifetime," University of Michigan, 2011.

[175]   K. U. Sawlani, "Effects of Secondary Electron Emission on the Plasma Sheath and Local Electron Energy Distribution with Application to Hall Thrusters," 2015.

[176]   G. Hobbs and J. Wesson, "Heat flow through a Langmuir sheath in the presence of electron emission," *Plasma Physics,* vol. 9, no. 1, p. 85, 1967.

[177]   X. Wang, J. Pilewskie, H. W. Hsu, and M. Horányi, "Plasma potential in the sheaths of electron-emitting surfaces in space," *Geophysical Research Letters,* vol. 43, no. 2, pp. 525-531, 2016.

[178]   D. M. Goebel, I. Katz, and I. G. Mikellides, *Fundamentals of electric propulsion*. John Wiley & Sons, 2023.

[179]   X. Yao and D. Jiang, "Effect of secondary electron emission on sheath potential in an electron cyclotron resonance plasma," *Journal of applied physics,* vol. 81, no. 5, pp. 2119-2123, 1997.

[180]   B. Pandey and S. Roy, "Sheath in the presence of secondary electron emission and sputtering yield," in *36 th AIAA Thermophysics Conference*, 2003.

[181]   J. F. Ziegler, "SRIM-2003," *Nuclear instruments and methods in physics research section B: Beam interactions with materials and atoms,* vol. 219, pp. 1027-1036, 2004.

[182]   C. Walker, M. El-Gomati, A. Assa'd, and M. Zadražil, "The secondary electron emission yield for 24 solid elements excited by primary electrons in the range 250–5000 eV: a theory/experiment comparison," *Scanning,* vol. 30, no. 5, pp. 365-380, 2008.

[183]   M. F. Diaz-Aguado, J. W. Bonnell, S. D. Bale, J. Wang, and M. Gruntman, "Parker Solar Probe FIELDS Instrument Charging in the Near Sun Environment: Part 1: Computational Model," *Journal of Geophysical Research: Space Physics,* vol. 126, no. 5, p. e2020JA028688, 2021.